

Chemical Science

Accepted Manuscript

This article can be cited before page numbers have been issued, to do this please use: C. Wang, S. Gao, X. Bu, J. Lei, G. Shao and Z. Zhou, *Chem. Sci.*, 2026, DOI: 10.1039/D6SC02712A.



This is an Accepted Manuscript, which has been through the Royal Society of Chemistry peer review process and has been accepted for publication.

Accepted Manuscripts are published online shortly after acceptance, before technical editing, formatting and proof reading. Using this free service, authors can make their results available to the community, in citable form, before we publish the edited article. We will replace this Accepted Manuscript with the edited and formatted Advance Article as soon as it is available.

You can find more information about Accepted Manuscripts in the [Information for Authors](#).

Please note that technical editing may introduce minor changes to the text and/or graphics, which may alter content. The journal's standard [Terms & Conditions](#) and the [Ethical guidelines](#) still apply. In no event shall the Royal Society of Chemistry be held responsible for any errors or omissions in this Accepted Manuscript or any consequences arising from the use of any information it contains.

ARTICLE

Metal-Support Interactions via Multidimensional Regulation in Key Electrocatalytic Reactions

Chaolong Wang,^a Shasha Gao,^b Xiaojing Bu,^a Jiacong Lei,^a Gonglei Shao,^{*,a,c} Zhen Zhou^{a,c}Received 00th January 20xx,
Accepted 00th January 20xx

DOI: 10.1039/x0xx00000x

Metal-Support Interactions (MSI) plays a pivotal role in boosting electrocatalytic performance by optimizing the electronic state of metal active sites and stabilizing them in different supports, thereby optimizing electron transfer kinetics and adsorption/desorption behavior of reaction intermediates. Hence, this review systematically elaborates on the MSI regulatory mechanisms of diverse support types and their microstates, along with its typical electrocatalytic applications. For support microstates: different crystal phases tune MSI strength via lattice arrangement differences; specific exposed crystal facets strengthen metal-support electronic coupling through lattice matching and surface coordination; vacancy defects in support serve as a key means for electronic state regulation to finely adjust MSI strength; atom doping in support significantly modulates MSI nature by altering interfacial electron transfer efficiency and constructing stable coordination structures. In electrocatalytic applications, MSI exerts critical regulatory effects and is widely applied in key reactions including catalytic water splitting (HER/OER), fuel cell-related reactions (HOR/ORR), carbon dioxide reduction reaction (CO₂RR), nitrogen reduction reaction (NRR), and small organic molecule oxidation. Therefore, this review systematically clarifies the multi-dimensional regulatory rules of support properties (type, crystal phase, facet, vacancies, doping) on MSI, and provides theoretical and practical guidance for the design and performance optimization of atomically dispersed catalysts.

1. Introduction

The progress of the chemical industry is inseparable from catalytic technology, and the innovative achievements of modern catalytic technology are an important driving force for the rapid development of fields such as petroleum exploitation and utilization, energy conversion, chemical production, and environmental governance.¹⁻³ Despite significant progress in catalytic research, many challenges remain to be addressed. Catalytic activity, selectivity, and stability affect the efficiency of catalysts in industrial production. For chemical industry production, low catalyst efficiency and high production costs will directly hinder their large-scale industrial application.^{4,5}

In catalytic reactions, catalysis relies on the contact between reactants and catalyst surface active centers. Maximizing the exposure of catalytic active sites on the surface significantly enhances catalytic efficiency. Theoretical studies indicate that metal catalysts can achieve 100% surface atom coverage, enabling all metal atoms to act as active sites.⁶ Thus, regulating metal components to the atomic level is a feasible and effective strategy to improve metal atom utilization. Structurally, single metal atoms and their surrounding

coordination structures form single-atom active centers, whose ordered distribution on supports constitutes single-atom catalysts (SACs). The atomic dispersion state and coordination environment of metal atoms are decisive for regulating catalyst intrinsic activity, reaction selectivity, and thermal stability.⁷ However, zero-valent metal single atoms are thermodynamically unstable and need stable anchoring via chemical bonding with coordinating atoms (O/S/P/C) in supports (e.g., oxides, sulfides, phosphides, carbon-based materials) to form structurally stable active sites.⁸⁻¹¹ In the design of atomically dispersed catalyst, Metal-support interactions (MSI) is the core mechanism for stabilizing active sites and regulating catalytic performance.

In fact, from traditional metal-supported catalysts to contemporary atomically dispersed catalysts, MSI has always been a key approach for stabilizing active sites, regulating electronic structures, and optimizing reaction kinetics. As catalytic research has shifted from particle catalysis to single-atom and cluster catalysis, the scope and dimensions of MSI have undergone systematic expansion, marking a paradigm shift from classical strong metal-support interaction (SMSI) to modern generalized MSI. The classical SMSI concept was proposed by Tauster et al.^{12,13} in the 1970s and was initially used to explain a unique phenomenon: when Group VIII metals were supported on reducible oxides such as TiO₂, the chemical adsorption of CO and H₂ was significantly suppressed after high-temperature reduction. Its core mechanism focuses on the

^a Interdisciplinary Research Center for Sustainable Energy Science and Engineering (IRC4SE²), School of Chemical Engineering, Zhengzhou University, Zhengzhou 450001, Henan, China

^b Key Laboratory of Microelectronics and Energy of Henan Province, Department of Physics and Electronic Engineering, Xinyang Normal University, Xinyang 464000, Henan, China

^c National Key Laboratory of Special Rare Metal Materials, Zhengzhou University, Zhengzhou 450001, Henan, China



migration and coating of support reduction species onto the surface of metal particles, forming an amorphous layer that physically shields active sites and alters adsorption properties. Research during this phase centered on structural coating and migration-induced coverage, primarily addressing thermodynamic and geometric structural effects, and provided foundational insights into the metal-support interface.¹⁴⁻¹⁶ With the rise of nanocatalysis, single-atom catalysis, and electrocatalysis, MSI has taken on a broader meaning, shifting the research focus from “surface coating” to atomic/electronic-scale phenomena such as interfacial electron transfer, orbital hybridization, coordination restructuring, spin state regulation, and strain effects.^{17,18} In modern electrocatalytic systems, MSI is no longer limited to oxide migration under high-temperature reduction conditions.¹⁹ Instead, it emphasizes that at the electrochemical reaction interface, the support interacts with the metal active center through deep electronic coupling, which are mediated by microstructures such as crystal phase, crystal facet, defects, and doping, thereby directionally regulating the charge density, spin state, and intermediate adsorption energy of active sites.

MSI in modern electrocatalytic systems represent both a continuation of and an evolution from classical SMSI. Both

approaches acknowledge the critical regulatory role of the support on the metal active sites and emphasize that interfacial interactions influence the intrinsic properties of the catalyst; However, they differ fundamentally in terms of research scale, core mechanisms, functional characteristics, and applicable scenarios. Classical SMSI focuses on nanometal particles and oxide supports, characterized primarily by support migration and coating, as well as the suppression of active site adsorption under high-temperature solid-state conditions; In contrast, MSI in modern electrocatalytic systems addresses atomic-scale active sites and multifunctional supports, operating within electrocatalytic environments.²⁰⁻²³ It relies on core mechanisms such as directed interfacial charge transfer, orbital hybridization coupling, and coordination structure reorganization, enabling the synergistic optimization of catalytic activity, selectivity, and stability, and better meeting the demands of key electrocatalytic reactions.²⁴⁻²⁹ Based on this, this paper systematically reviews current research on MSI in various types of support materials, as well as the effects of the support crystal phase, crystal facet, vacancies, and atomic doping on MSI.³⁰⁻³³ It then provides a detailed account of the application of MSI in electrocatalytic reactions, including HER, OER, HOR, ORR, CO₂RR, NRR, and the oxidation of small organic molecules (Figure 1).

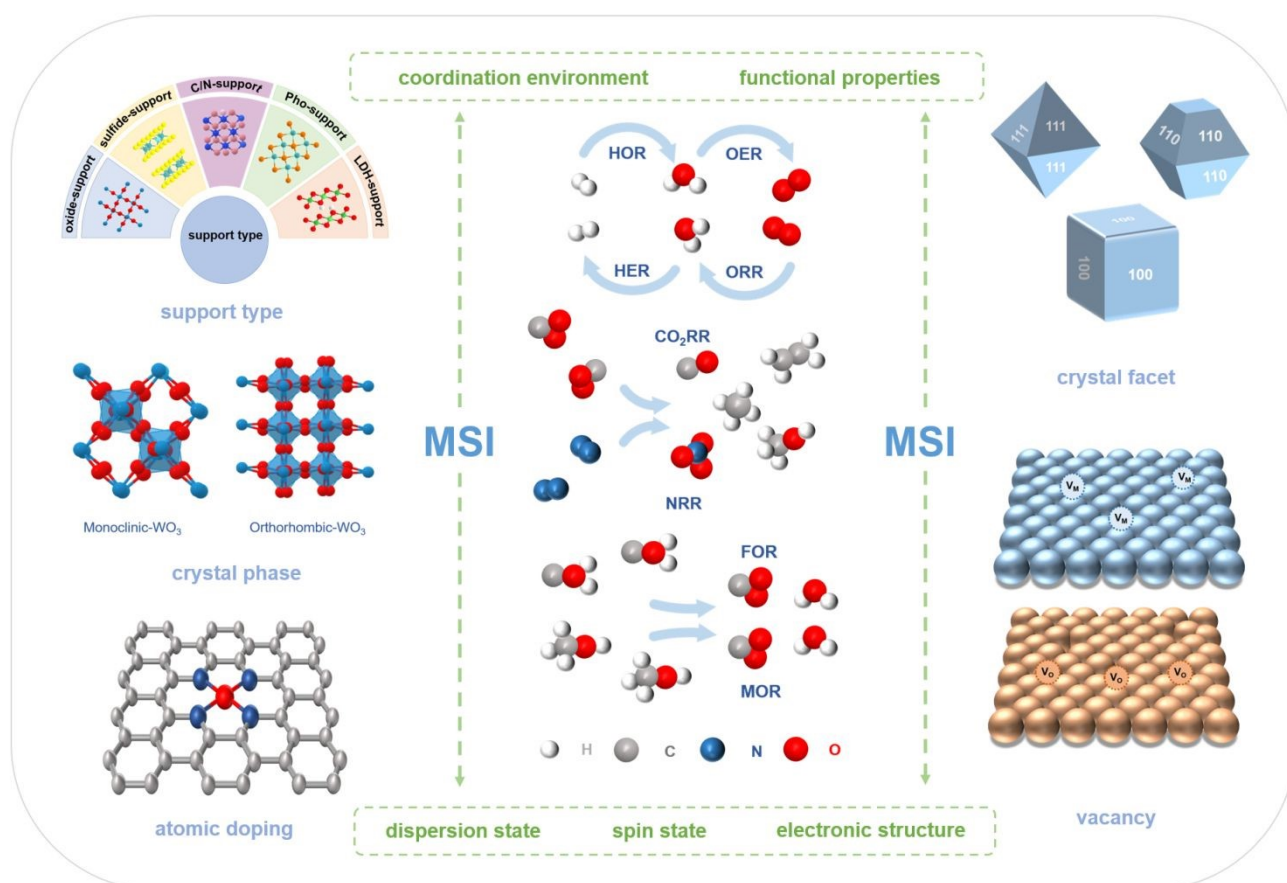


Figure 1. Influencing factors of MSI in electrochemical applications.

2. Classification of MSI



ARTICLE

In the design and optimization of metal-supported catalysts, MSI constitute a key mechanism determining catalytic performance. The support not only provides a physical anchoring site for the metal active center but also profoundly regulates the intensity and mode of MSI through its chemical and structural properties. This, in turn, influences the electronic structure, coordination environment, and reaction kinetics of the active site. The multidimensional regulation of MSI by support properties are systematically reviewed, focusing on the fine-tuning mechanisms from the perspectives of support type, crystal phase, crystal facet, vacancy defects, and atomic doping characteristics. Notably, variations in the microscopic state of the support precisely modulate the electronic state and stability of the metallic active site by altering interfacial electronic properties, lattice matching, coordination bond order, and defect density.

The mechanisms underlying MSI between the support and the supported metal are highly diverse, and we have provided a general overview of them. Overall, the structural stability and intrinsic activity of the catalyst are primarily regulated through the synergistic effects of physical and chemical interactions between the support and the metal (Figure 2). At the physical level, this interaction strongly depends on the geometric structure, spatial arrangement, and interfacial physical fields of the support. First, the crystal phase structure and lattice constant of the support directly determine the lattice matching and strain state at the interface. High lattice matching between the support and the supported metal promotes epitaxial growth of the metal, thereby effectively reducing interfacial energy and significantly strengthening the bonding force. Second, the unique structure of the support generates a strong spatial confinement effect, physically isolating and anchoring the supported metal atoms to suppress their agglomeration during the reaction. Furthermore, the work function difference (ΔW_F) between the support and the metal, along with the localized polar electric fields concentrated around individual atoms, not only influences the accumulation of interfacial charges and the spillover migration of active species but also directionally guides the adsorption pathways of reactant molecules. At the chemical level, MSI manifests as deep, substantial electron transfer, orbital overlap, and chemical bonding processes. The key to stabilizing metal active sites on the support lies in forming strong coordinate or covalent bonds between the supported metal atoms and the coordinating elements of the support (such as O, S, P, C, N, etc.), thereby preventing metal migration. Notably, the microscopic state of the support directly

determines the coordination configuration of the metal-supported active center. Building on this, directional electron transfer and orbital hybridization, driven by interfacial electronegativity differences, can finely tune the electron density of the supported metal and reshape the position of its d-band center. This optimization enhances the thermodynamic adsorption behavior toward reaction intermediates. Furthermore, precise design of the support type and coordination environment can specifically induce spin state transitions in metal single atoms. Such transitions significantly enhance the delocalization of electrons in the central metal's d orbitals, as well as their hybridization and activation capabilities with reactants.

As discussed above, MSI influences catalytic behavior through both physical and chemical effects. The stability of MSI interface under harsh operating conditions is still a real concern. Even though MSI helps disperse and anchor metal atoms through coordination bonds, covalent bonding, and strong electronic coupling, the interface can still undergo major structural changes under strongly acidic or strongly oxidizing environments. In strong acids, high concentrations of H^+ can protonate and erode polar interfacial bonds like $M-N_x$ and $M-O$. This leads to ligand breaking, support surface etching, and eventually dissolution or agglomeration of the metal sites. Under strong oxidizing potentials, metal centers tend to get overoxidized into high valence species. These high-valence metal ions have high charge density, small ionic radii, and large hydration energy, so they thermodynamically prefer to stay as dissolved ions in solution rather than remain in the solid state. That greatly weakens the electronic coupling between the metal and support, causing interfacial detachment and overall structural instability. On top of that, strongly oxidizing conditions often speed up support corrosion and create interfacial defects, which further hurts MSI stability and durability.

To improve MSI stability under strongly acidic and oxidizing conditions, the key is to build interfaces with strong covalent bonding, high coordination saturation, and good corrosion resistance. Strengthening the interfacial bonds and suppressing proton attack and oxidative erosion can effectively reduce interfacial dissociation and metal leaching, thus preserving both the structure and the catalytic activity over long term operation. To make it easier to compare the resist leaching and maintain structural stability of different support materials by MSI bonds in polar electrolytes (acidic or alkaline), we have added a corresponding table (Table 1).



ARTICLE

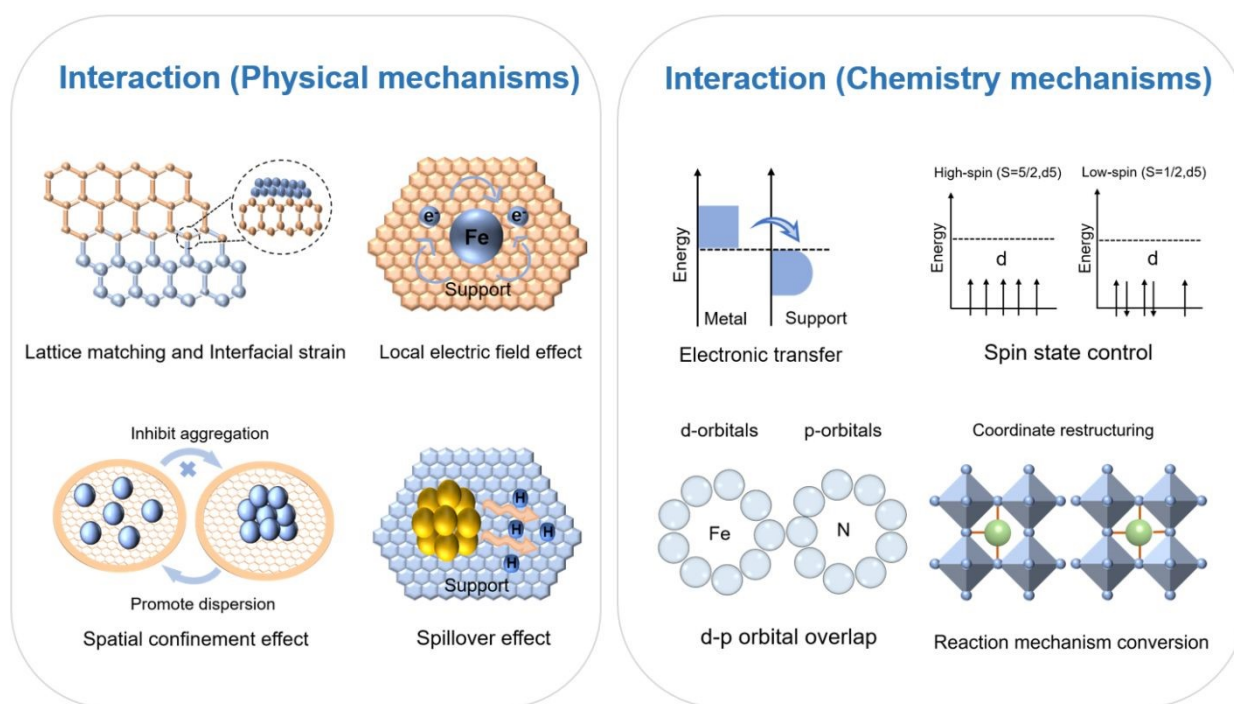


Figure 2. Comprehensive classification of MSI mechanisms.

Table 1 Leaching resistance and stability of MSI Interfaces for different supports in polar electrolytes

Support Type	Typical interface chemical bonds	Stability in Acid	Stability in Alkali	Resistance mechanism
Oxide support	M ₁ -O-M ₂	Good	Excellent	Ionic bonds/Covalent bonds
Sulfide support	M-S/M ₁ -S-M ₂	Medium	Good	Covalent bonds
Carbon support	M-C	Medium	Good	Covalent bonds
N-doped carbon support	M-N/M-N-C	Excellent	Excellent	Covalent bonds
Nitride support	M-N/M ₁ -N-M ₂	Good	Excellent	Covalent bonds
Phosphide support	M-P/M ₁ -P-M ₂	Good	Excellent	Covalent bonds
LDH support	M-O/M-OH, M ₁ -O-M ₂	Poor	Excellent	Ionic bonds/Covalent bonds

2.1. MSI on Various Support

2.1.1. Oxide-Supported Catalyst

Oxides have been widely utilized as both supports and catalysts in the design and synthesis of heterogeneous catalysts. The performance and stability of metal-supported on metal oxides primarily depend on the multiple interactions between metal atoms and the unique surface structures and electronic properties of the supports. Furthermore, the coordination environment and electronic structure of supported metals are

significantly influenced by the intrinsic properties of the supports.³⁴⁻³⁶ Specifically, the distinct physicochemical properties of different oxide supports can modulate the electron distribution and band structure of metals at the metal-support interface, thereby affecting their adsorption strength toward reaction intermediates and ultimately regulating the activity and selectivity of catalytic reactions.³⁷

Manganese oxides attract extensive attention due to their abundant reserves, low cost and structural diversity. Various modification strategies have been explored, among which single-atom modification is effective for achieving 100% atomic



utilization and high activity. Yang et al.³⁸ prepared a high-valent Ir single-atom bifunctional catalyst ($\text{Ir}_{\text{SA}}\text{-MnO}_x$) anchored on phosphorylated MnO_x hollow nanospheres via a simple wet chemical adsorption method (Figure 3a). Compared with the recently reported single atomic Ir-crystalline MnO_2 -based catalysts, its hollow and weakly crystalline structure provides more anchoring sites and larger specific surface area. Transmission electron microscope (TEM) and selected area electron diffraction (SAED) confirm its hollow morphology and weak crystallinity, high-angle annular dark-field scanning transmission electron microscopy (HAADF-STEM) verifies atomic dispersion of Ir (Figure 3b-c). X-ray absorption near edge structure (XANES) and X-ray photoelectron spectroscopy (XPS) analyses reveal its electronic structure: Mn K-edge XANES shows Ir incorporation does not alter Mn electronic state (average oxidation state +3.2). Ir L_3 -edge XANES and Ir 4f XPS

spectra confirm Ir is in high valence ($> +4$) with positive-shifted and symmetric peaks. Theoretical studies indicate Mn^{3+} centers are bifunctionally active for oxygen evolution reaction (OER)/oxygen reduction reaction (ORR), while high-valent Ir optimizes intermediate adsorption energy, and MSI provides a theoretical basis for the catalyst's bifunctional performance.

For titanium oxide (TiO_2), Sun et al.³⁹ prepared a TiO_2 -supported copper SAC (Cu_1/TiO_2) via a simple hydrothermal method for the electrocatalytic reduction of NO_2^- to NH_3 (Figure 3d). In-situ Fourier transform infrared spectroscopy (In-situ FTIR) and density functional theory (DFT) studies demonstrate that the TiO_2 -anchored Cu single atoms can narrow the band gap of TiO_2 and promote electron transfer, thereby significantly enhancing NH_3 selectivity and yield. HAADF-STEM confirms uniform and high-density atomic dispersion of Cu on Cu_1/TiO_2 (Figure 3e). Fourier transform extended X-ray absorption fine structure (FT-EXAFS) shows a Cu-O peak at 1.5 Å (no Cu-Cu peak), reconfirming atomic Cu dispersion on TiO_2 .

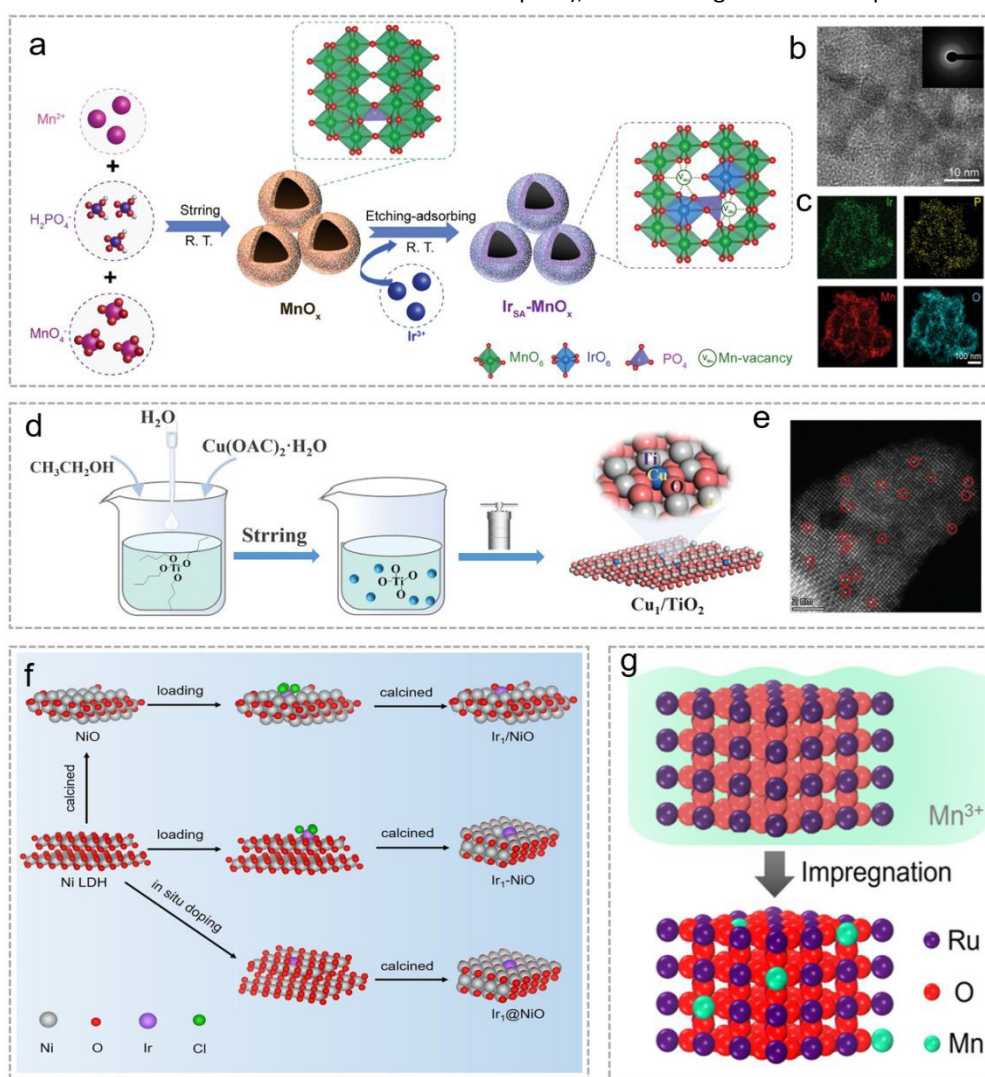


Figure 3. The effect of oxide-supported on MSI. (a) Scheme of the preparation procedure of $\text{Ir}_{\text{SA}}\text{-MnO}_x$. (b) High-resolution TEM image of $\text{Ir}_{\text{SA}}\text{-MnO}_x$. (c) EDS elemental maps of $\text{Ir}_{\text{SA}}\text{-MnO}_x$. Reproduced with permission.³⁸ Copyright 2024, Wiley. (d) The synthesis procedures of Ir_1/NiO , $\text{Ir}_1\text{-NiO}$, and $\text{Ir}_1@\text{NiO}$. (e) HAADF-STEM image for Cu_1/TiO_2 (1.45 wt.%). Reproduced with permission.³⁹ Copyright 2025, Wiley. (f) The synthesis procedures of Ir_1/NiO , $\text{Ir}_1\text{-NiO}$, and $\text{Ir}_1@\text{NiO}$. Reproduced with permission.⁴⁰ Copyright 2024, Wiley. (g) Synthesis and structure of the $\text{Mn}_{(\text{SA})}/\text{RuO}_2$ catalyst. Reproduced with permission.⁴¹ Copyright 2025, American Chemical Society.



ARTICLE

XPS spectra reveals a high-binding-energy shift of O 1s in Cu₁/TiO₂ vs. pure TiO₂, indicating strong Cu-TiO₂ electronic interaction that stabilizes Cu single atoms and modulates the catalyst's electronic structure. For nickel oxide (NiO), Wei et al.⁴⁰ synthesized three Ir SACs (Ir₁/NiO, Ir₁-NiO, Ir@NiO) on NiO via different anchoring methods (Figure 3f): Ir₁/NiO from calcining IrCl₃-loaded NiO nanosheets (Ni LDH-derived); Ir₁-NiO from spin-coating and calcining Ir-loaded Ni LDH; Ir@NiO from calcining Ir-doped Ni LDH (Ir in NiO lattice). X-ray Absorption Spectroscopy (XAS) analyses confirming atomic dispersion of Ir. XPS spectra shows Ir 4f binding energies decrease with increasing coordination number (Ir₁/NiO < Ir₁-NiO < Ir@NiO), implying reduced Ir valence. Correspondingly, Ni³⁺/Ni²⁺ ratio in Ni 2p spectra increases, indicating enhanced Ni-Ir electron transfer and elevated Ni valence. Ultimately, Ir₁-NiO with moderate Ir-O-Ni coordination number exhibits optimal OER performance.

Ruthenium-based catalysts have attracted attention due to excellent OER activity, but suffer from limited OER stability and easy degradation in oxidizing environments. Xue et al.⁴¹ synthesized a single-atom Mn-modified RuO₂ catalyst (Mn_(SA)/RuO₂) via simple impregnation (Figure 3g). Single-atom Mn modification tailors the electronic structure of RuO₂ and optimizes MSI. Ru 3d XPS shows a 0.2 eV negative shift of Ru 3d_{5/2} peak after Mn incorporation, with a similar shift in Ru 3p spectrum; Mn_(SA)/RuO₂ also has lower Ru K-edge energy and white line peak than RuO₂. These confirm reduced Ru oxidation state and MSI induced by electron transfer. In-situ Raman spectroscopy reveals the crystal structure features of RuO₂: 500 cm⁻¹ (O out-of-plane vibration E_g mode), 614 cm⁻¹ and 690 cm⁻¹ sharp peaks (A_{1g} and B_{2g} modes of O vibration around Ru). When overpotential increases from 1.23 V to 1.53 V, A_{1g} peak of pure RuO₂ shifts ~23 cm⁻¹, while this peak of Mn_(SA)/RuO₂ shift reduces to ~13 cm⁻¹. This indicates Mn incorporation inhibits Ru-O bond vibration/stretching during OER, significantly enhancing RuO₂ stability.

Apart from the aforementioned oxides, many transition metal oxides have also been developed into various metal-supported oxide catalysts. Although the oxide carriers are different, MSI plays an important role in each of them. The properties of oxide-support regulate the electronic structure and coordination environment of the supported metals through MSI, thereby modulating the catalytic activity, selectivity, and stability.

2.1.2. Sulfide-Supported Catalyst

Two-dimensional (2D) transition metal dichalcogenides (TMDs) exhibit significant advantages in electrochemical energy applications due to their unique electronic structures and

tunable physicochemical properties.⁴² These materials possess tunable conductivity, abundant active sites, and excellent electron transport capabilities, making them ideal electrochemical functional materials. The MSI in sulfide-supported catalysts significantly influences catalytic performance, as sulfide supports can effectively regulate the dispersion, electronic state, and stability of active metals. For instance, sulfur edge sites in molybdenum disulfide (MoS₂) serve as anchoring points for metal-supported, suppressing migration and agglomeration to enhance catalyst durability.^{43,44} Concurrently, electron transfer between metals and chalcogenide supports optimizes the d-band centers at metal active sites, boosting reactant adsorption and activation capabilities.⁴⁵

Such as 2D tungsten disulfide (WS₂) support, Lv et al.⁴⁶ constructed Ni-WS₂ catalyst (Figure 4a). The MSI promotes *H generation, accelerates interfacial charge transfer, and optimizes intermediate adsorption. W 4f_{7/2} and W 4f_{5/2} (W⁴⁺) in Ni-WS₂ positively shift by 0.3 eV vs. WS₂; S 2p binding energy shows no significant shift, confirming electron transfer mainly between Ni and W. Ni 2p_{3/2} and Ni 2p_{1/2} in Ni-WS₂ negatively shift by 0.5 eV vs. standard Ni²⁺, verifying MSI-induced charge redistribution. FT-EXAFS reveals first coordination peak at 1.61 Å of Ni-WS₂, with shorter Ni-S bond length than NiS, reflecting strong Ni-WS₂ interatomic coupling from MSI. DFT calculations also confirm that Ni insertion enhances electron transport and conductivity, facilitating nitrate reduction reaction (NO₃RR) and improving catalytic performance.

Wang et al.²⁴ synthesized ultrafine Ru nanoclusters supported on FeMo-S nanosheets, obtaining FeMo-S/Ru hetero-interface catalyst for both hydrogen evolution reaction (HER) and sulfion oxidation reaction (SOR) (Figure 4b). Experiments and DFT calculations confirm strong Ru-FeMo-S electron interaction, which optimizes H adsorption and promotes sulfur intermediate formation/adsorption. HAADF-STEM images show uniform Ru nanoclusters anchoring on FeMo-S, providing structural basis for interfacial interaction (Figure 4c). HAADF-STEM reveals close contact between FeMo₂S₄ and Ru planes, enabling electron transfer. Ru nanoclusters have uniform size distribution, indicating MSI suppresses Ru migration/agglomeration (Figure 4d). XPS confirms Ru-FeMo-S binding: Fe 2p peaks negatively shift 0.6 eV vs. FeMo-S; Mo 3d peaks negatively shift 0.5 eV; S 2p peaks show 0.4 eV negative shift of S²⁻; Ru 3p peaks confirm Ru incorporation and minor surface oxidation. DFT calculation shows the electron transfer from Ru to FeMo-S, further confirming the existence of MSI in Ru-FeMo-S.

MoS₂ is a promising cost-effective alternative support to precious metal HER catalysts, but suffers from poor conductivity



and limited active sites. Liu et al.⁴⁷ synthesized Ni SA/rGO-CTAB-MoS₂, featuring single-atom Ni encapsulated in rGO-CTAB-MoS₂ curled nanosheet nanoflowers (Figure 4e). In the XPS spectra of Mo 3d, the binding energy of Mo 3d in Ni SA/rGO-CTAB-MoS₂ exhibits a significant shift toward lower energies compared to rGO-CTAB-MoS₂, indicating that Ni introduction alters the electronic structure of Mo. The Ni 2p spectrum of Ni SA/rGO-CTAB-MoS₂ decomposes into six peaks, the peaks at 856.2 eV and 873.5 eV correspond to Ni²⁺, indicating the presence of coordination bonds between Ni and S, consistent with FTIR results. Compared to rGO-CTAB-MoS₂, the peaks in this sample exhibit a shift toward higher energies, indicating strong interactions between individual Ni atoms and rGO-CTAB-MoS₂.

This significantly enhances the stability of Ni single atoms during the electrocatalytic process.

DOI: 10.1039/D6SC02712A

TMDs are considered promising electrochemical functional materials due to their unique 2D layered structures and tunable conductivity. But they still have issues: low intrinsic conductivity and a tendency for supported metal species to aggregate. MSI can help by stably anchoring metal active sites at defect sites on the sulfide support, tuning the electronic structure of the active sites through directional electron transfer, and inducing surface reconstruction to expose more active sites. This provides key support for rationally designing TMD-supported catalysts.

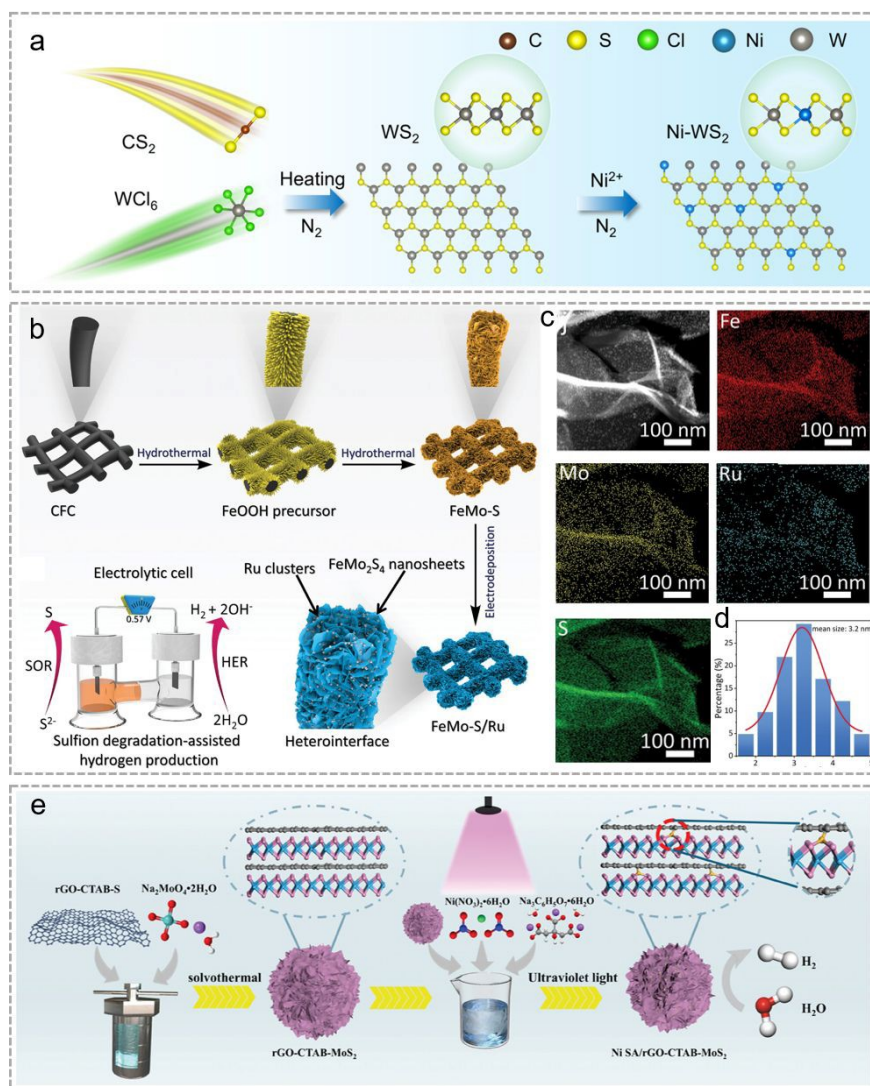


Figure 4. The effect of sulfide-supported on MSI. (a) Schematic illustration of the preparation of Ni-WS₂ nanoflowers. Reproduced with permission.⁴⁶ Copyright 2025, American Chemical Society. (b) Schematic illustration for the synthesis of FeMo-S/Ru catalyst. (c) HAADF-STEM image and corresponding elemental mapping of FeMo-S/Ru. (d) The size distribution of Ru clusters. Reproduced with permission.²⁴ Copyright 2024, Wiley. (e) Schematic diagram of the preparation of Ni SA/rGO-CTAB-MoS₂ composites by hydrothermal and photodeposition processes. Reproduced with permission.⁴⁷ Copyright 2025, Wiley.

2.1.3. Carbon/Nitride-Supported Catalyst

Carbon-supported SACs have been widely applied in industrially important reactions such as electrocatalysis and photocatalysis

due to their unique metal-ligand synergistic effects.⁴⁸⁻⁵⁰ Compared to oxide/sulfide supports, carbon supports have three key advantages: high conductivity (facilitating electron transfer), abundant pores (optimizing mass transfer), and low cost (boosting industrial scalability).⁵¹ However, weak carbon-



metal interactions hinder metal single-atom anchoring. Introducing N into carbon supports is critical to enhance MSI. N enables unique M-N bond characteristics via orbital hybridization, distinct from M-C and M-O bonds.^{2,52-54} Structurally, N anchors metal species through two mechanisms: forming coordinate bonds with metal vacant orbitals via lone pairs, and forming strong covalent bonds to suppress metal migration. Electronically, metal d-orbital and N p-orbital hybridization enhances covalency, forms delocalized electron systems, fills metal d bands and constructs efficient electron transport pathways between active sites and supports.

In recent years, SACs with M-N₄-C configuration have been widely used in ORR. Sun et al.⁵⁵ employed a simple pyrolysis method to anchor cobalt single atoms to a carbon support via chelation with adjacent Co₂N nanoparticles (Co SAs/Co₂N)

(Figure 5a). Within the carbon support, individual cobalt atoms are firmly anchored to carbon support via Co-Co covalent bonds. Simultaneously, Co₂N nanoparticles serve as an electron reservoir, establishing efficient electron transfer pathways for Co atoms through Co-Co covalent bonds. HAADF-STEM images of Co SAs/Co₂N confirms Co single-atom form (Figure 5b). Co K-edge XANES reveals a significant negative shift of the pre-edge peak for Co SAs/Co₂N compared to CoPc, indicating the reduced Co valence and confirming Co single-atom sites as electron acceptors. Bader charge analysis shows electron-rich Co₂N transfers -0.44 e⁻ to Co single-atom acceptors. Electron density difference maps of intermediate adsorption states visually confirm efficient electron transfer from Co₂N to cobalt single atoms. By the MSI, Co SAs/Co₂N exhibits excellent ORR performance.

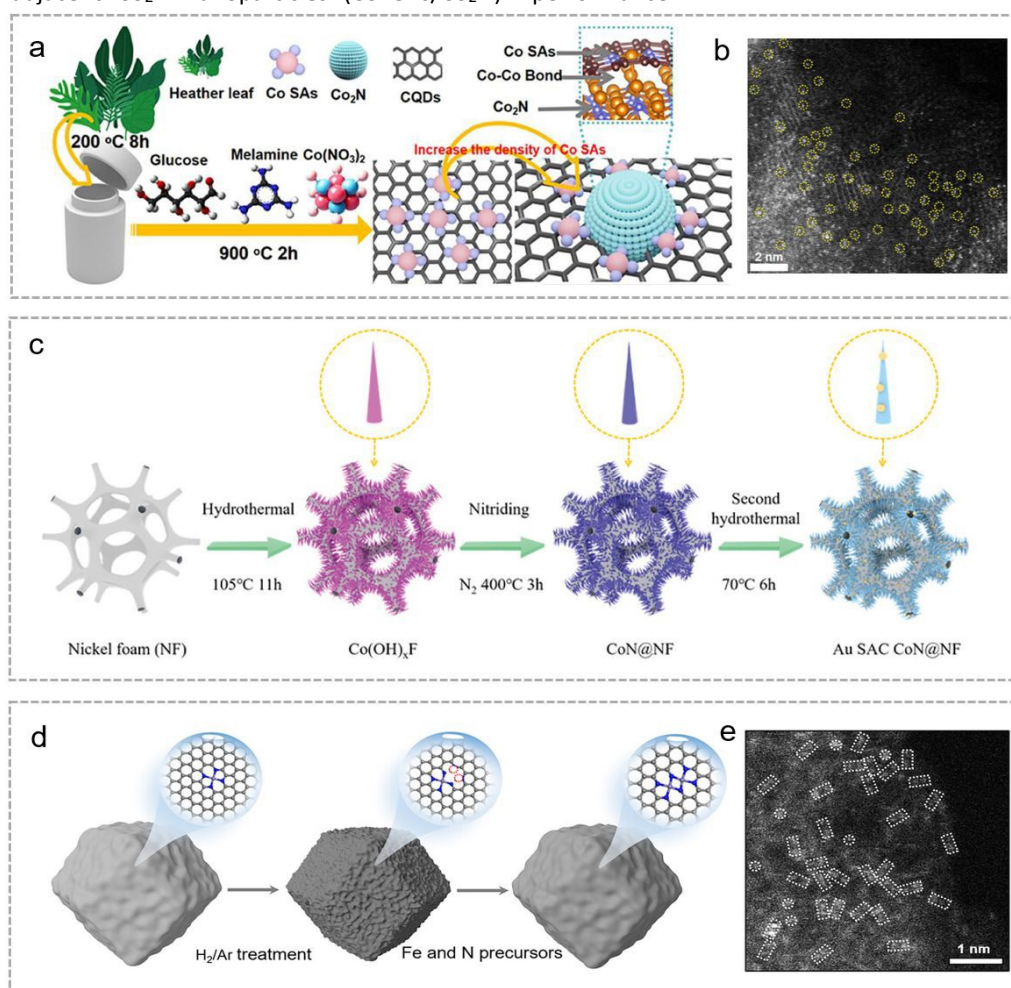


Figure 5. The effect of carbon/nitride-supported on MSI. (a) Synthesis process diagram of Co SAs/Co₂N catalyst. (b) HAADF-STEM images of Co SAs/Co₂N. Reproduced with permission.⁵⁵ Copyright 2025, Wiley. (c) Schematics of the synthesis process of the Au SAC CoN@NF. Reproduced with permission.⁵⁶ Copyright 2024, Wiley. (d) Schematic illustration showing the synthetic procedure to fabricate T-Fe-N-C catalyst. (e) HAADF-STEM image of T-Fe-N-C catalysts. Reproduced with permission.⁵⁷ Copyright 2025, Wiley.

N atoms on transition metal nitrides stabilize single atoms via coordination and synergistically regulate active site adsorption energy with metal atoms. Chen and Li⁵⁶ prepared Au SAC CoN@NF by loading Au atoms onto CoN nanorods supported on nickel foam, enabling strong MSI (Figure 5c). XRD pattern of Au SAC CoN without Au characteristic peaks are

observed, confirming stable single-atom Au anchoring via MSI. XANES and EXAFS characterize the electronic state and local coordination of single-atom sites. First-principles calculations confirm significant interaction between Au single atoms and CoN support, with pronounced orbital overlap near the Fermi level among Au 5d, Co 3d and N 2p orbitals. This orbital coupling



driven by the MSI enhances the bonding between the d orbitals of Co and the p orbitals of N, accelerating the kinetic processes of the ORR and OER.

To address this stability challenge about Fe dissolution in active FeN₄ sites, Wang et al.⁵⁷ treated pre-synthesized Fe-N-C catalysts in Ar/H₂ atmosphere, cleaving C-N bonds around FeN₄ sites and introducing Fe/N precursors to transform FeN₄ single-atom sites into Fe₂N₆ diatomic sites on carbon supports (Figure 5d). HAADF-STEM observations verify the structural transformation: uniform Fe single atoms in pristine Fe-N-C vs abundant Fe-Fe diatomic sites in T-Fe-N-C (Figure 5e). Fe K-edge XANES shows a lower energy absorption edge for T-Fe-N-C, indicating reduced Fe oxidation state. Time-of-flight secondary ion mass spectrometry (TOF-SIMS) shows a distinct FeN₄ peak in pristine Fe-N-C and a stronger Fe₂N₆ peak in T-Fe-N-C, confirming the single-to-diatom site transformation. Notably, proton exchange membrane fuel cell (PEMFC) assembled with T-Fe-N-C operates stably for 300 hours with only 7% current density decay.

Beyond the above, Shao et al.⁵⁸ synthesized PhenPtCl₂ nanosheets with N₂-Pt-Cl₂ coordination via ultrasonic-assisted solvothermal method using 1,10-phenanthroline and H₂PtCl₆ as precursors. In situ Raman and XPS reveal dynamic coordination evolution of N₂-Pt-Cl₂ active sites during electrocatalysis: Phen-Pt-Cl₂ → Phen-Pt-Cl → Phen-Pt. Phen-Pt intermediates play a key role in HER, dynamically coordinating with Cl⁻ in electrolyte; unsaturated bidentate Pt sites in Phen-Pt provide additional space and electrons for H⁺ adsorption and H₂ evolution. Similarly, Han et al.⁵⁹ constructs a 2D organic complex precursor with predefined O₂-Ru-N₂ coordination. MSI forms between PDAH and Ru: it immobilizes Ru via strong coordination bonds to prevent agglomeration and ensure isolated Ru atoms, while predefining Ru-N/O coordination patterns to template asymmetric O₂-Ru-N₂ active sites during subsequent pyrolysis. This asymmetric SAC also achieves efficient HER activity across the entire pH range. To address CO poisoning and transition metal (Ni/Co) dissolution in direct methanol fuel cell (DMFC) anodes, Chen et al.⁶⁰ tuned the interfacial electron transfer between TiN and PtNiCo to create an electron-rich state on PtNiCo. This strategy downshifts the d-band center of Pt, weakening CO adsorption and enhancing CO tolerance, while also strengthening Pt-Ni/Pt-Co bonds and suppressing transition metal dissolution. Consequently, the e-PtNiCo catalyst achieves high methanol oxidation activity and exceptional long-term stability in DMFCs.

In summary, for carbon-based/nitride supports, the key challenge in achieving high-performance and stability catalyst lies in balancing high electrical conductivity with strong MSI during electrocatalytic reactions, particularly under high current density conditions. Highly graphitized carbon frameworks provide excellent conductivity, ensuring rapid charge transport, effectively reducing ohmic resistance, and maintaining efficient catalysis under high current conditions. However, highly conjugated, perfect carbon structures typically lack sufficient metal anchoring sites, resulting in weak MSI. In contrast, the introduction of nitrogen doping and the formation of M-N_x coordination structures can significantly enhance MSI

through orbital hybridization, interfacial electron coupling, and chemical bonding, enabling the stable anchoring of metal single atoms and optimizing the adsorption and desorption behavior of reaction intermediates.

Therefore, rational structural design of carbon-based/nitride supports holds promise for fundamentally resolving this contradiction: utilizing a continuous graphitized carbon framework to maintain high-conductivity pathways while leveraging nitrogen sites to provide strong MSI. Through the synergistic interaction between the carbon framework and nitrogen sites, the trade-off between conductivity and interfacial interactions is effectively regulated. This synergistic strategy not only accelerates electron transport but also stabilizes atomically dispersed metal active sites and suppresses metal migration and dissolution, enabling the catalyst to maintain excellent structural stability even under high current density conditions. In short, the synergistic regulation of conductivity and MSI in carbon-based/nitride support systems provides important insights for the design of high-performance electrocatalysts.

2.1.4. Phosphide-Supported Catalyst

Metal phosphides, important functional materials composed of metals and phosphorus, possess unique physicochemical properties and distinct MSI characteristics, promising as supports or active components. Significant charge redistribution between metal-supported and phosphorus modulates atomic oxidation states, stabilizes Fermi-level electronic states, and endows high electron density and carrier mobility. Multiple MSI mechanisms stabilize supported metals, facilitate charge transfer to enhance catalytic activity and stability, and improve oxidation/acid resistance for sustained performance under harsh conditions.^{61,62} With tunable chemical composition and microstructure, metal phosphides gain growing attention in electrocatalysis.^{63,64} Designing multi-metal phosphides, advancing support interface engineering, and studying dynamic reaction mechanisms will further promote their applications in clean energy conversion and green synthesis.

For example, Luo et al.⁶⁵ fabricated the MoP@Mn_{SAC}-NC electrocatalyst by combining ultrafine MoP with atomically dispersed Mn-N₄ systems (Figure 6a). The MoP-Mn-N₄ interface forms strong electron phosphide-support interaction (EPSI) via Mo-N and Mo-P bonds, inducing electron delocalization in Mn-N₄ segments and low-spin to high-spin transition of Mn. Electron transfer occurs from Mn 3d d_{xz/yz} orbitals to d_{z²/d_{x²-y²} orbitals, enhancing Mn-O₂ interaction and optimizing *OOH adsorption. MoP@Mn_{SAC}-NC exhibits 35.5% Mn³⁺ (higher than 28.1% in Mn_{SAC}-NC), 47.9% Mo³⁺ (higher than 17.3% in MoP@NC) and lower Mo⁶⁺ (52.1% vs. 82.7% in MoP@NC), confirming electron transfer from Mn-N₄ to MoP. Collectively, MoP incorporation optimizes Mn electronic structure and spin state, efficiently promoting ORR.}

Additionally, metal-phosphide interaction optimizes active site distribution, increasing their quantity/exposure to enhance catalytic activity. He et al.⁶⁶ prepared single-atom Ru-doped Ni₅P₄ via phosphating Ru-impregnated nickel vacancy-enriched



Ni(OH)₂ (Figure 6b). HAADF-STEM verifies atomically dispersed Ru in Ni₅P₄-Ru. EXAFS reveals high-density atomic Ru anchoring via Ru-P and Ru-O-Ni bonds, with no Ru-Ru bonds. Ru³⁺ oxidation state is regulated by the support. This coordination structure induces lattice distortion and electron redistribution, increasing density of states (DOS) near the Fermi level and boosting charge transport. Ru-site electron enrichment reduces water dissociation energy barrier from 1.97 eV to 1.28 eV and optimizes hydrogen adsorption free energy.

As a transition metal phosphide, NiFeCo-P features excellent conductivity, abundant active sites, and multi-metal composition enabling electronic structure modulation via synergistic effects. Zhou et al.⁶⁷ developed Pt nanocluster-loaded NiFeCo-P with a 2D nanosheet array structure (Figure 6c). HRTEM confirms the uniform size distribution of Pt clusters (Figure 6d-e). XPS and electrochemical impedance spectroscopy (EIS) demonstrate that MSI facilitates electron transfer from NiFeCo-P to Pt nanoclusters, reduces catalyst-electrolyte interface charge transfer resistance and suppresses Pt

agglomeration. Benefiting from MSI-maintained structural integrity during reactions, the catalyst displays excellent water splitting performance in simulated alkaline seawater.

NiCoP shows potential in alkaline water electrolysis but suffers from sluggish kinetics and poor stability. Fan et al.⁶⁸ developed a robust bifunctional Ru SAs@NiCoP/NF catalyst by anchoring Ru_{SA} on NiCoP-coated nickel foam (Figure 6f). Ru achieves atomic dispersion via phosphorus-rich coordination and forms MSI. Phosphorus-rich coordination induces Ru electron redistribution, optimizes Ni/Co d-band centers, and lowers water dissociation and O₂ desorption energy barriers. High-resolution XPS shows that after Ru loading, Ni³⁺ 2p_{3/2} and 2p_{1/2} peaks, Co²⁺ 2p_{3/2} and 2p_{1/2} peaks of NiCoP/NF all shift to lower binding energies, indicating Ru acts as an electron donor to inject electrons to Ni/Co or O sites via MSI. MSI enhances water activation for HER and promotes P leaching/surface reconstruction to regulate OER intermediate adsorption-desorption via the lattice oxygen mechanism (LOM).

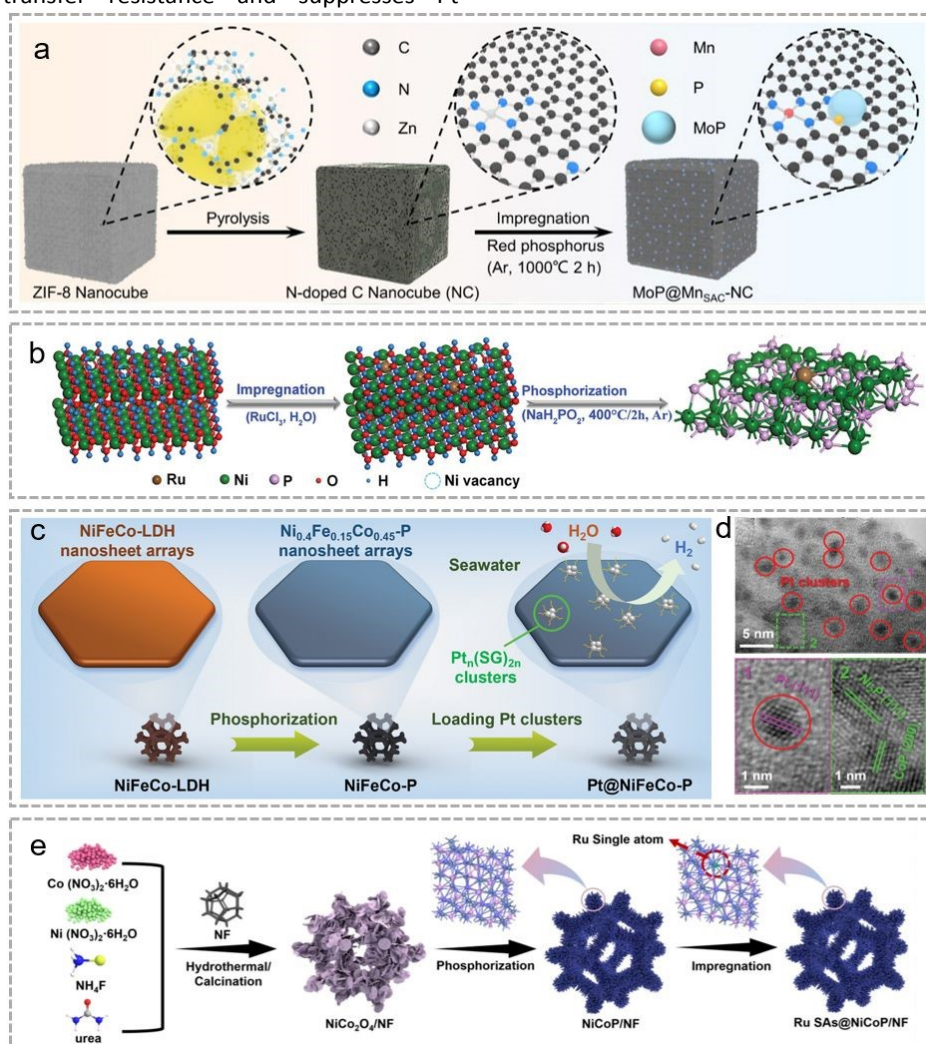


Figure 6. The effect of Phosphide-supported on MSI. (a) Schematic illustration for the preparation of the catalyst. Reproduced with permission.⁶⁵ Copyright 2025, Wiley. (b) Schematic diagram for the synthesis of Ni₅P₄-Ru. Reproduced with permission.⁶⁶ Copyright 2025, Wiley. (c) Schematic illustration of the synthesis of Pt@NiFeCo-P. (d) HRTEM image of Pt@NiFeCo-P. Reproduced with permission.⁶⁷ Copyright 2024, Wiley. (e) Schematic illustration for the synthesis of Ru SAs@NiCoP/NF. Reproduced with permission.⁶⁸ Copyright 2025, Wiley.



In fact, most transition metal phosphides possess tunable composition, high conductivity, structural stability, and corrosion resistance, making them excellent catalytic supports. However, their practical application is hindered by several limitations, including uneven distribution of active sites, insufficient precision in electronic structure modulation, metal agglomeration, and potential phosphorus leaching. MSI effectively addresses these issues by anchoring metal sites via strong metal-phosphorus interactions, thereby enabling uniform dispersion of active sites. Moreover, MSI-mediated directional electron transfer regulates the electron density and spin state of metal sites, optimizes the adsorption of reaction intermediates, and accelerates interfacial charge transfer. More importantly, a rational balance between high electrical conductivity and strong MSI in phosphide supports ensures rapid charge transfer under high current density conditions while simultaneously suppressing metal dissolution and phosphorus leaching, thus significantly enhancing catalytic activity, durability, and industrial application potential.

2.1.5. LDH-Supported Catalyst

View Article Online

DOI: 10.1039/D6SC02712A

Layered double hydroxides (LDHs) are inorganic functional materials with unique layered structures, assembled by electrostatic interactions between positive metal ions and interlayer anions. Tuning metal ions and interlayer anions yields materials with varied electronic structures and surface properties.⁶⁹⁻⁷² LDHs have large specific surface area, abundant active sites and strong ion exchange capacity, showing broad prospects in electrochemistry.⁷³⁻⁷⁵ The advantages of single-atom metal-LDH interactions lie in electronic and geometric synergies: anchoring via coordination bonding, interlayer confinement or defect trapping prevents single-atom migration/agglomeration.^{76,77} LDHs modulate active site electronic structures via charge transfer and orbital hybridization to optimize catalysis.⁷⁸ Key synergistic factors include: stable anchoring sites from LDH layers, electronic interactions between LDHs and single atoms, and synergistic networks of multiple active centers formed by LDH intrinsic active sites and single atoms.

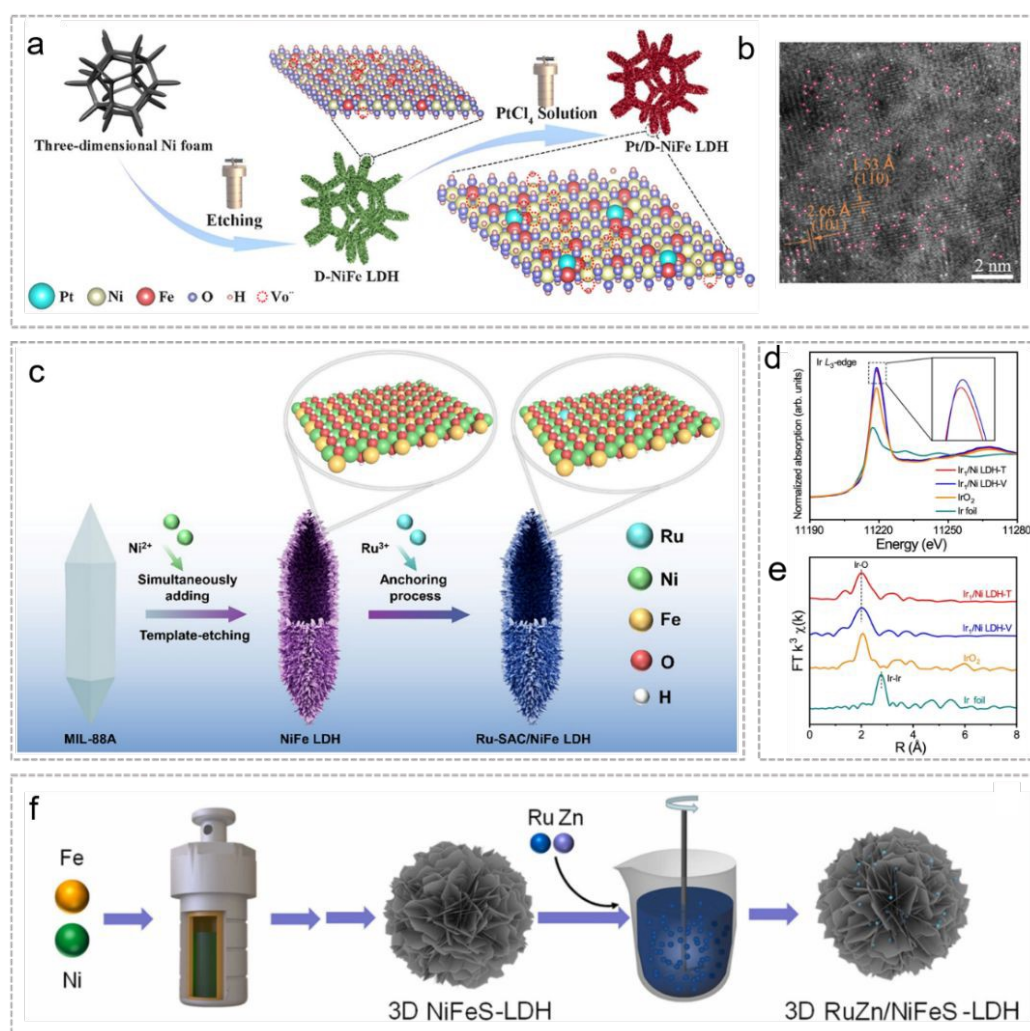


Figure 7. The effect of LDH-supported on MSI. (a) Schematic illustration of the synthetic procedure for Pt/D-NiFe-LDH. (b) AC-HAADF-STEM image of Pt/D-NiFe-LDH. Reproduced with permission.⁷⁹ Copyright 2025, Wiley. (c) Schematic illustration for the fabrication of Ru-SAC/NiFe LDH. Reproduced with permission.⁸⁰ Copyright 2025, Wiley. Normalized XANES (d) and EXAFS (e) spectra at the Ir L₃-edge for Ir₁/Ni LDH-T and Ir₁/Ni LDH-V. Reproduced with permission.⁸¹ Copyright 2024, Springer Nature. (f) The catalyst preparation procedure. Reproduced with permission.⁸² Copyright 2025, Elsevier.



For instance, Shen et al.⁷⁹ achieved quantitative control of oxygen vacancy (O_v) concentration in Pt/NiFe-LDH via tuning H_2O_2 etching amount, and synthesized Pt/D-NiFe-LDH (Figure 7a). Atomically dispersed Pt is anchored on oxygen-vacancy-rich NiFe-LDH, forming a Pt-Ni electronic bridge for charge transfer (Figure 7b). Oxygen vacancies promote electron migration from Ni to Pt, rendering Pt negatively charged, downshifting its d-band center and enhancing hydrogen adsorption. XPS shows Pt 4f_{7/2} binding energy of Pt/D-NiFe-LDH shifts negatively by 0.80 eV vs. metallic Pt/NiFe-LDH, confirming reduced valence of Pt. Ni 2p_{3/2} peak shifts positively by 0.16 eV for Pt/NiFe-LDH and 0.91 eV for Pt/D-NiFe-LDH vs. NiFe-LDH. PDOS analysis shows Pt d-band center of Pt/D-NiFe-LDH downshifts significantly vs. Pt/NiFe-LDH, weakening Pt-H bond strength. Charge density difference analysis and Bader charge calculations confirm electron transfer from Ni to Pt. Oxygen defects modulate Pt electronic structure via Pt-Ni electron bridges, accelerating water dissociation kinetics and optimizing hydrogen intermediate adsorption, enabling excellent HER performance.

A "structure-enabled MSI" strategy for high-efficiency SACs can be achieved by designing LDH supports with unique structures. Isras et al.⁸⁰ engineered hollow nanocage-structured NiFe LDH to efficiently anchor and stably disperse Ru single atoms (Figure 7c). The catalyst enhances MSI via spatial confinement and electronic coupling dual effects. The hollow nanocage structure combine with Ru modification increases exposed active sites. The XPS of Ru-NiFe LDH shows Ru 3p binding energy between Ru³⁺ and Ru⁴⁺, Ni 2p binding energy shifts positively by 0.3 eV vs. NiFe-LDH, Fe 2p binding energy shifts negatively by 0.2 eV vs. NiFe-LDH. This demonstrate charge redistribution via Ru-O-M bonds and synergistic electronic interactions. O 1s spectrum shows M-O-M bond binding energy shifts positively by 0.1 eV, indicating enhanced oxygen site and electron attraction by highly electronegative Ru via Ru-O-M interactions. NiFe LDH hollow nanocage structure enhances Ru-NiFe LDH MSI by optimizing coordination environment and electronic coupling pathways, stabilizing single-atom active sites and improving catalytic performance via electronic structure regulation.

Wei et al.⁸¹ proposed an electrochemical deposition strategy-anchoring Ir single atoms on Ni LDH. Cathodic electrodeposition anchors Ir atoms to Ni LDH triple face-centered cubic vacancies, forming Ir₁/Ni LDH-T. Anodic deposition connects Ir to oxygen vacancies through apical oxygen, yielding Ir₁/Ni LDH-V. Ir₁/Ni LDH-T exhibits stronger MSI due to additional Ir-O covalent bonds with Ni LDH. Ir L₃-edge XANES spectra demonstrate stronger white line intensities than IrO₂ for both catalysts, confirming Ir valence > +4 (Figure 7d). The weaker white line of Ir₁/Ni LDH-T indicates slightly lower Ir valence, implying Ni LDH-to-Ir electron transfer and distinct MSI strengths. Ir L₃-edge EXAFS spectra exhibit a dominant ~1.98 Å peak for Ir-O bonds, confirming monodispersed Ir (Figure 7e). Ni 2p XPS spectra reveal a positive Ni 2p peak shift in Ir₁/Ni LDH-T vs. pure Ni LDH, while Ir₁/Ni LDH-V shows no shift. Ir 4d XPS of Ir₁/Ni LDH-T displays a slight negative shift vs. Ir₁/Ni LDH-V, indicating lower Ir valence. This confirms that stronger MSI in Ir₁/Ni LDH-T enhances Ni-to-Ir electron transfer, increasing Ni

valence. Strong MSI in Ir₁/Ni LDH-T optimizes oxygen-containing intermediate adsorption and shifts the active site from Ni to Ir.

More, Xu et al.⁸² constructed a 3D RuZn/NiFeS-LDH by introducing Zn clusters into Ru/NiFeS-LDH (Figure 7f). Zn cluster doping increases oxygen vacancies on the support surface and enhances intermetallic interactions, which promote electron rearrangement and suppress excessive oxidation of Ni²⁺ bonds. Ni 2p XPS results show that sulfur shifts the Ni 2p peak to higher binding energy by 0.3 eV, altering Ni's chemical state. Ru further shifts the peak by 0.4 eV, while Zn induces a negative shift through electronic interactions. This prevents Ni³⁺ from further oxidation and stabilizes the active species Ni²⁺ ($0 < \sigma \leq 1$), providing a stable active center for 5-hydroxymethylfurfural electrooxidation (HMFOR). Zn K-edge EXAFS exhibits characteristic peaks of Zn-O, Zn-Zn and Zn-Ni bonds. This confirms Zn bonds with support oxygen, forms Zn clusters and interacts directly with Ni. Such multi-bond cooperative interactions allow Zn clusters to regulate support electron distribution, stabilize active species Ni²⁺, ultimately enhancing the overall HMFOR performance of the catalyst.

LDHs supports can achieve preliminary dispersion of metal species through coordination bonding and interlayer confinement, making them excellent supports for metal-supported catalysts. However, challenges remain in difficulty of regulating electronic structure, limited conductivity, the monotonous coordination environment around active sites, and insufficient structural stability during reactions. The charge transfer and orbital hybridization can be precisely modulated through coordination environments of active sites, enhancing charge transport efficiency between the support and active components. Additionally, MSI induces surface reconstruction and defect formation on LDHs, optimizing the adsorption energy barriers for intermediates while strengthening interfacial bonding. This approach significantly boosts both the catalytic activity and long-term stability of the catalyst.

2.2. Crystal Phase Regulation for MSI

As an MSI regulation strategy, support crystal phase exhibits inherent differences in atomic arrangement, lattice constants and surface electronic states. These differences significantly affect MSI intensity and pathways via multiple physicochemical mechanisms, thereby precisely controlling the electronic structure and reaction efficiency of catalytic active sites.⁸³ Theoretically, lattice symmetry and atomic packing density variations among support crystal phases directly influence the MSI between the support and the metal-loaded components. Higher matching enables epitaxial growth or coherent interfaces, reducing interfacial energy and strengthening bonding. Significant lattice mismatch induces interfacial strain. Support crystal phase also modulates metal sites nucleation and growth kinetics. Crystal phases with higher surface energy or unique atomic arrangements provide more anchoring sites, promoting metal precursor reduction and dispersion.

WO₃ is promising for boosting catalytic performance through phase regulation due to its diverse crystal structures and unique chemical properties. Composed of WO₆ octahedra



connected via shared corners/edges, WO_3 has multiple phases (hexagonal H- WO_3 , orthorhombic O- WO_3 , monoclinic M- WO_3) with distinct characteristics.⁸⁴ The WO_3 support can stabilize active centers and regulate reactant adsorption-desorption for improved electrocatalytic activity.⁸⁵ The crystalline features of WO_3 rely on WO_6 octahedral arrangement. In H- WO_3 , octahedra link via apical oxygen to form horizontal hexagonal ring networks and vertical 3D stacking, creating multi-channel porous structures for rapid ion transport (Figure 8a). O- WO_3 forms distorted octahedral coordination; octahedra interlink within layers via shared edges/vertices, with weak interlayer intermolecular forces, retaining only vertical square channels and restricting ion transport (Figure 8b). M- WO_3 adopts a twisted ReO_3 -type structure, with WO_6 octahedra linked via apical oxygen into a highly twisted 3D network, forming twisted cubic channels and increasing ion migration resistance (Figure 8c). These structural variations result in distinct electrochemical properties.

Based on the above discussion, Xu et al.⁸⁶ investigated the effect of WO_3 crystal phases (H- WO_3 , O- WO_3 , M- WO_3) as supports on Ru nanoparticle performance in HER. TEM images

showed bulk structures for all samples, with Ru uniformly distributed on H- WO_3 but concentrated at edges of O- WO_3 and M- WO_3 . Uniform Ru distribution enhances activity and utilization. Work function difference (ΔW_F) analysis reveals significant variations between Ru and different WO_3 phases (Figure 8d). Ru/H- WO_3 has the smallest ΔW_F , followed by Ru/O- WO_3 , with Ru/M- WO_3 showing the largest. Smaller ΔW_F reduces interfacial charge accumulation, lowers hydrogen spillover energy barrier, and promotes H^* migration/desorption from Ru to WO_3 , accelerating HER kinetics. Larger ΔW_F increases spillover resistance and diminishes performance. Benefiting from the smallest ΔW_F and stronger Ru anchoring/dispersion ability, Ru/H- WO_3 exhibits the best HER activity. First-principles DFT calculations confirmed these observations. Ru exhibits the lowest binding energy on H- WO_3 (both W and O sites), ensuring superior stability and uniform dispersion. Higher formation energies and site-dependent differences in O- WO_3 and M- WO_3 hindered stable distribution (Figure 8e). A 13-Ru cluster model further verified the lowest formation energy of Ru/H- WO_3 , confirming its advantage in anchoring and dispersing Ru (Figure 8f), which enhances active site stability and utilization.

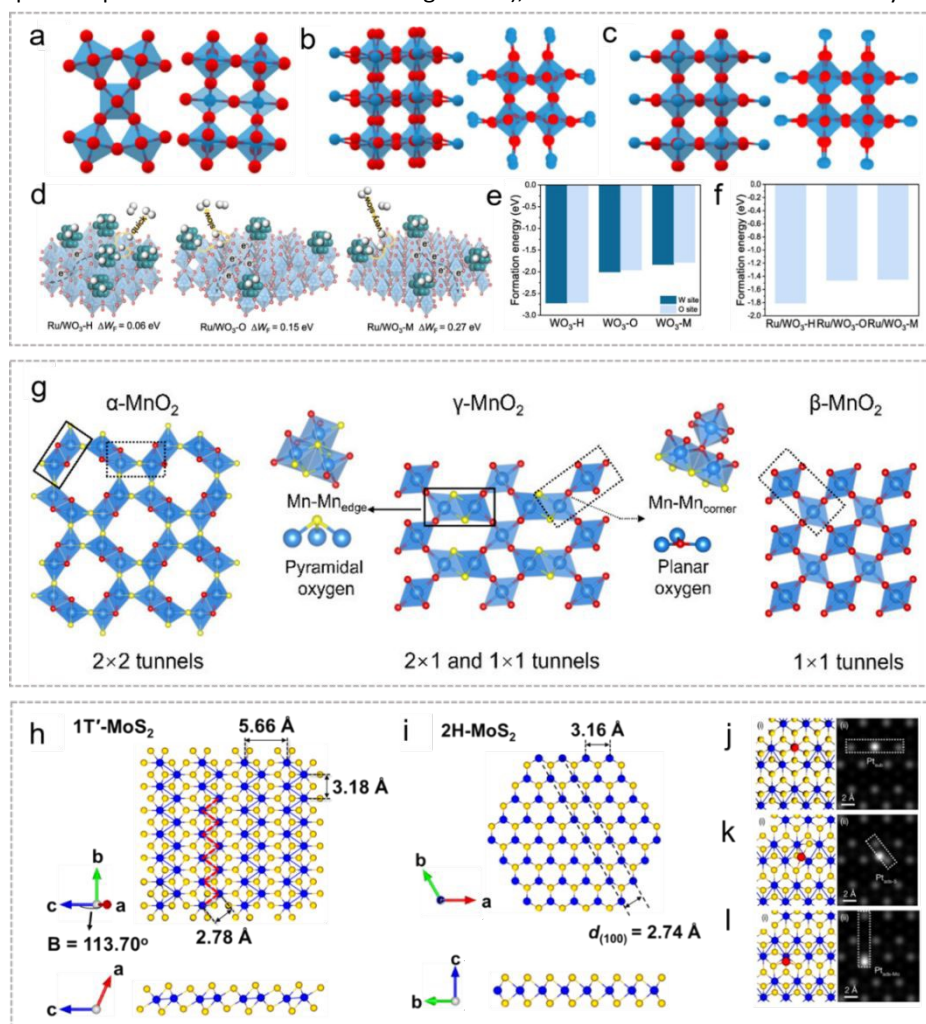


Figure 8. The effect of crystal phase on MSI. Crystal structure model of (a) hexagonal, (b) orthorhombic, and (c) monoclinic phases from different views (red atoms representing O and blue atoms representing W). (d) Schematic illustration of the interaction mechanism between different WO_3 supports and Ru to activate HER. The formation energy of (e) a single Ru atom and (f) Ru clusters coupling with the support. Reproduced with permission.⁸⁶ Copyright 2025, Elsevier. (g) Schematic crystal structure of α -



MnO₂, γ -MnO₂, and β -MnO₂. The blue, red, and yellow balls represent Mn, O_{pla}, and O_{pyr} atoms, respectively. Reproduced with permission.⁸⁷ Copyright 2025, American Chemical Society. (h) Schematic illustrations of the atomic structures of 1T'-MoS₂. (i) Schematic illustrations of the atomic structures of 2H-MoS₂. (j-l) Simulated atomic structures and the corresponding simulated STEM images of Pt_{sub}, Pt_{ads}-S and Pt_{ads}-Mo. Reproduced with permission.⁸⁸ Copyright 2023, Springer Nature.

She et al.⁸⁷ regulated MSI by adjusting MnO₂ tunnel size to solve kinetic delays and Ru site instability. Crystal engineering of α -MnO₂, β -MnO₂, γ -MnO₂ reveal that reduced tunnel size increases planar oxygen (O_{pla}) content, strengthening Ru-O_{pla}-Mn bonds and MSI. However, overly small tunnels of β -MnO₂ cause surface amorphization upon Ru doping, weakening MSI. Thus, Ru- γ -MnO₂ shows superior catalytic activity and stability. The three MnO₂ polymorphs share [MnO₆] octahedra but differ in stacking, with tunnel structures of 2×2(α -MnO₂), hybrid 2×1/1×1 (γ -MnO₂) and 1×1 (β -MnO₂) as shown in (Figure 8g). XRD and EXAFS confirmed increased O_{pla} proportion with smaller tunnels, and O_{pla}-formed Mn-O bonds are stronger, validated by H₂ temperature-programmed reduction (H₂-TPR). Higher O_{pla} inhibits Ru incorporation, leading to Ru content in the order α -MnO₂ > γ -MnO₂ > β -MnO₂. Mn K-edge XANES shows Ru- γ -MnO₂ has abundant Mn³⁺ and oxygen vacancies. Ru K-edge EXAFS confirms Ru-O coordination, with shorter Ru-O bonds in Ru- γ -MnO₂ enhancing MSI and Ru oxidation state. Ru K-edge XANES indicates the strongest MSI in Ru- γ -MnO₂ due to moderate O_{pla} inducing strong Ru-O_{pla}-Mn bonds. γ -MnO₂ also induces lattice strain and low-valent Mn sites, endowing Ru- γ -MnO₂ with outstanding activity.

2D TMDs are key template materials for supported catalysts. Using Pt on MoS₂ for hydrogen evolution as an example, mixed-phase MoS₂ leads to only partial epitaxial Pt nanoparticle growth. To address this issue, Shi et al.⁸⁸ developed a method to obtain high-purity phase MoS₂ nanosheets. 2H-MoS₂ promotes epitaxial Pt nanoparticle growth (Figure 8i), while 1T'-MoS₂ supports atomically dispersed Pt (s-Pt) with loadings up to 10 wt% (Figure 8h). DFT calculations and a multi-step validation approach identified three distinct sites for single-atom Pt on 1T'-MoS₂: a Pt-substituted Mo site (Pt_{sub}, Figure 8j), a Pt atom atop a sulfur atom (Pt_{ads}-S, Figure 8k), and a Pt atom atop a Mo atom (Pt_{ads}-Mo, Figure 8l). Pt at the Mo apical site shows near-zero hydrogen adsorption free energy, correlating with excellent HER performance.

Whereupon, the crystal phase of the support is the key structural parameter for regulating MSI. By governing lattice matching, interfacial electron transfer, and metal dispersion, crystal phase determines both the strength and mechanism of MSI at the atomic and electronic levels, thereby directly defining the intrinsic activity, number, and selectivity of active sites.

2.3. Crystal Facet Regulation for MSI

The crystal facets of catalyst support critically regulate the geometric and electronic environment of active sites. For example, TiO₂ facet nanotraps can shift Co single atoms from four-coordination to three-coordination, markedly boosting catalytic performance.⁸⁹ Similarly, exposed facets on CdSe nanoplates directly dictate single-atom positioning and

activity.⁹⁰ By precisely selecting facets, coordination structures can be tailored to influence reaction pathways and barriers. Furthermore, facets can generate localized electric fields that modify the electronic state of active sites and intermediate adsorption. High-curvature nanostructures, for instance, create strong electric fields that promote proton-coupled electron transfer, significantly enhancing oxygen reduction efficiency.⁹¹

Zheng et al.⁹² used a lattice-matched melt co-growth method to epitaxially grow Ir on the (111) facet of vanadium nitride (VN) (Figure 9a). This process involves Ir³⁺ reduction to metallic Ir and epitaxial growth due to lattice continuity. At the interface, Ir-V bonds induce electron transfer from V to Ir, which suppresses Ir oxidation and enhances stability. The strong interfacial coupling, along with compressive strain in the Ir atomic layer, weakens CO adsorption and improves poisoning resistance. The growth proceeds in two stages: initial single-atom/cluster deposition and subsequent epitaxial expansion into an ordered atomic Ir layer (Figure 9b). HRTEM analysis confirms [111] zone axis alignment and interplanar spacings of 2.51 Å and 2.22 Å (Figures 8c), demonstrating near-perfect epitaxy. The side-view structure further shows aligned (111) facet orientations (Figure 9d). PDOS analysis shows the Ir d-band center shifting below the Fermi level, confirming electronic rearrangement through strong MSI, which ultimately enhances catalyst stability and tolerance.

The exposed crystal facet of a support critically determines the atomic arrangement and coordination environment of active sites. For example, the Cu (111) facet uniquely promotes C-C coupling, forming the structural basis for efficient CO₂ electrolysis. Based on this mechanism, Liu et al.⁹³ designed Co single-atom-modified Cu (111) triangular nanosheets (CuCo₁). By controlling the Cu support to expose the (111) facet, they achieved directional anchoring of Co single atoms, creating a strongly interacting Co-Cu (111) interface. The Cu (111) provides stable anchoring sites and modulates Co's electronic state, while Co in turn optimizes *CO adsorption on Cu (111), lowering the C-C coupling barrier. XRD confirms CuCo₁ matches metallic Cu, with dominant Cu (111) diffraction (Figure 9e). HAADF-STEM shows clear lattice fringes (0.13 nm, Cu (220)) without structural distortion (Figure 9f). XAS shows Cu is primarily metallic, with a Cu-Cu peak at 2.22 Å and a minor Cu-O peak (Figure 9g). Co XANES indicates an average oxidation state near +2, and EXAFS reveals a Co-O-Cu scattering path at 2.70 Å, confirming atomic level Co-Cu bonding (Figure 9h). Overall, CuCo₁ successfully combines a metallic Cu support exposing the (111) facet with atomically dispersed Co via Co-O-Cu bonds. In situ studies and calculations show that Co tunes CO adsorption and promotes the OCCOH intermediate, while Cu (111) stabilizes the hydrogenation step.

To address the challenge of poorly defined catalyst structures, Liu et al.⁹⁴ combined facet engineering of TiO₂ nanocrystals with Co single-atom doping to clarify the active



surface and catalytic center. By adjusting the $\text{TiCl}_4/\text{TiF}_4$ precursor ratio during colloidal pyrolysis, they synthesized two distinct morphologies: bipyramidal nanocrystals with dominant (101) facets were obtained at a 4:1 ratio, while a 1:4 ratio produced nanoplates primarily exposing (001) facets (Figure 9i-m). Co atoms are doped as single atoms, substituting Ti in the lattice. Grand canonical quantum mechanics calculations revealed that Co preferentially substitutes five-coordinated Ti sites (Ti_{5c}) on the (001) surface, forming a stable five-coordinated Co site during OER. In contrast, Co on the (101) surface remains six-coordinated. This structural difference

dictates activity: the (001) facet facilitates dissociative water adsorption and maintains a low-coordination Co site.

Therefore, the exposed crystal facets of a support material uniquely modulate the surface atomic arrangement, local coordination environment, and geometric configuration of metal active sites. Through facet engineering, the interfacial coordination structure is tailored, and the electronic structure of active sites is regulated via MSI, effectively optimizing the adsorption behavior of reaction intermediates and lowering the energy barriers of electrocatalytic reactions. Thus, facet engineering offers a unique and effective means to precisely manipulate the strength and nature of MSI.

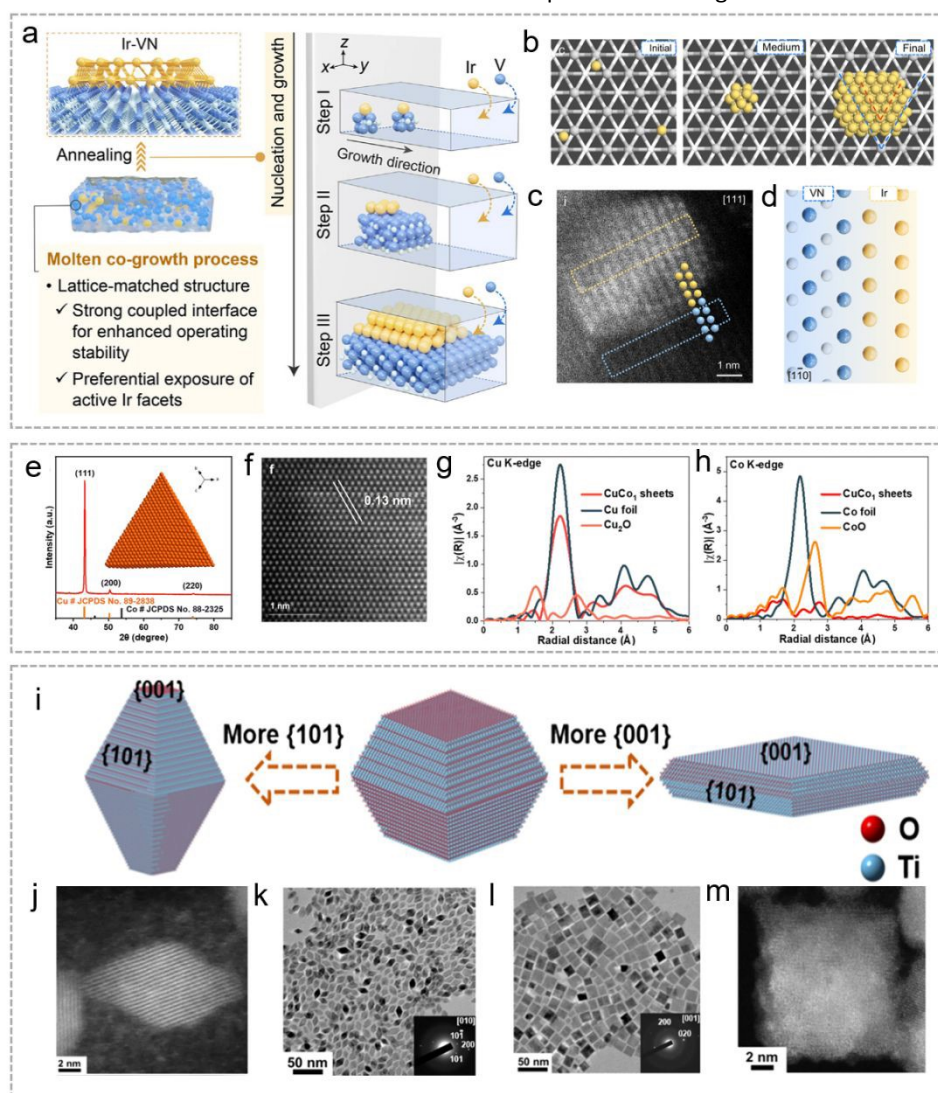


Figure 9. The effect of crystal facet on MSI. (a) The molten co-growth of Ir-VN. (b) The theoretic formation process of Ir (111) on VN during the molten co-growth process. (c) HAADF-STEM image of structural representation of Ir layers along VN support. (d) The side view of the corresponding model of the lattice-matched interface in Ir-VN catalyst. Reproduced with permission.⁹² Copyright 2025, Wiley. (e) XRD pattern of CuCo_1 sheets. (f) Aberration-corrected STEM images on the inside. (g) Fourier transform EXAFS spectra of CuCo_1 sheets, Cu foil, and Cu_2O . (h) Fourier transform EXAFS spectra of CuCo_1 sheets, Co foil, and CoO. Reproduced with permission.⁹³ Copyright 2025, Royal Society of Chemistry. (i) Schematic illustrations displaying how varying the prevalence of 001 and 101 surface facets of Co-TiO₂ nanocrystals results in nanobipyramid and nanoplate shapes. (j) HAADF-STEM image of a Co-TiO₂ nanobipyramid. (k) TEM image of Co-TiO₂ nanobipyramids (inset: the SAED pattern s). (l) TEM image of Co-TiO₂ nanoplates (inset: the SAED pattern). (m) HAADF-STEM image of a Co-TiO₂ nanoplate. Reproduced with permission under CC-BY 4.0.⁹⁴ Copyright 2025, American Chemical Society.

2.4. Vacancy Regulation for MSI



Vacancy in support are critical defects that regulate MSI by modifying the local atomic and electronic environment.⁹⁵ Electronically, vacancy types (e.g., oxygen vacancies in oxides) influence electron transfer between the support and metal-supported, regulate the oxidation state and d-band structure of metal sites. Structurally, vacancies act as anchoring sites that stabilize highly dispersed metal species, preventing aggregation. The resulting lattice distortion and modified coordination environment can further tune orbital hybridization, activating otherwise inert metal centers. Collectively, these effects influence reactant adsorption, activation pathways, and overall catalytic performance.

Regarding the cation vacancies, Zhang et al.⁹⁶ designed Ru-Co_vO₄ by engineering Co vacancies in Co₃O₄ (Figure 10a).

Cation vacancies enhance electronic coupling between Ru and Co, promoting orbital hybridization in the Ru-O-Co structure. The d-spacing of (111) facet is clearly expanded from 0.468 nm in Co₃O₄ to 0.475 nm in Ru-Co_vO₄ due to the Ru atoms with larger atomic radius (Figure 10b). HAADF-STEM and EDS confirm Ru exists as isolated single atoms (Figure 10c-d). This increases the Co³⁺/Co²⁺ ratio and shifts binding energies, indicating stronger electron transfer in Ru-Co_vO₄. EPR signals intensify with vacancies, confirming enhanced unpaired electrons and orbital hybridization. Collectively, cation vacancies shift the OER mechanism toward a more efficient pathway by strengthening Ru-Co synergy, lowering the O₂ desorption barrier, and significantly boosting acidic OER performance.

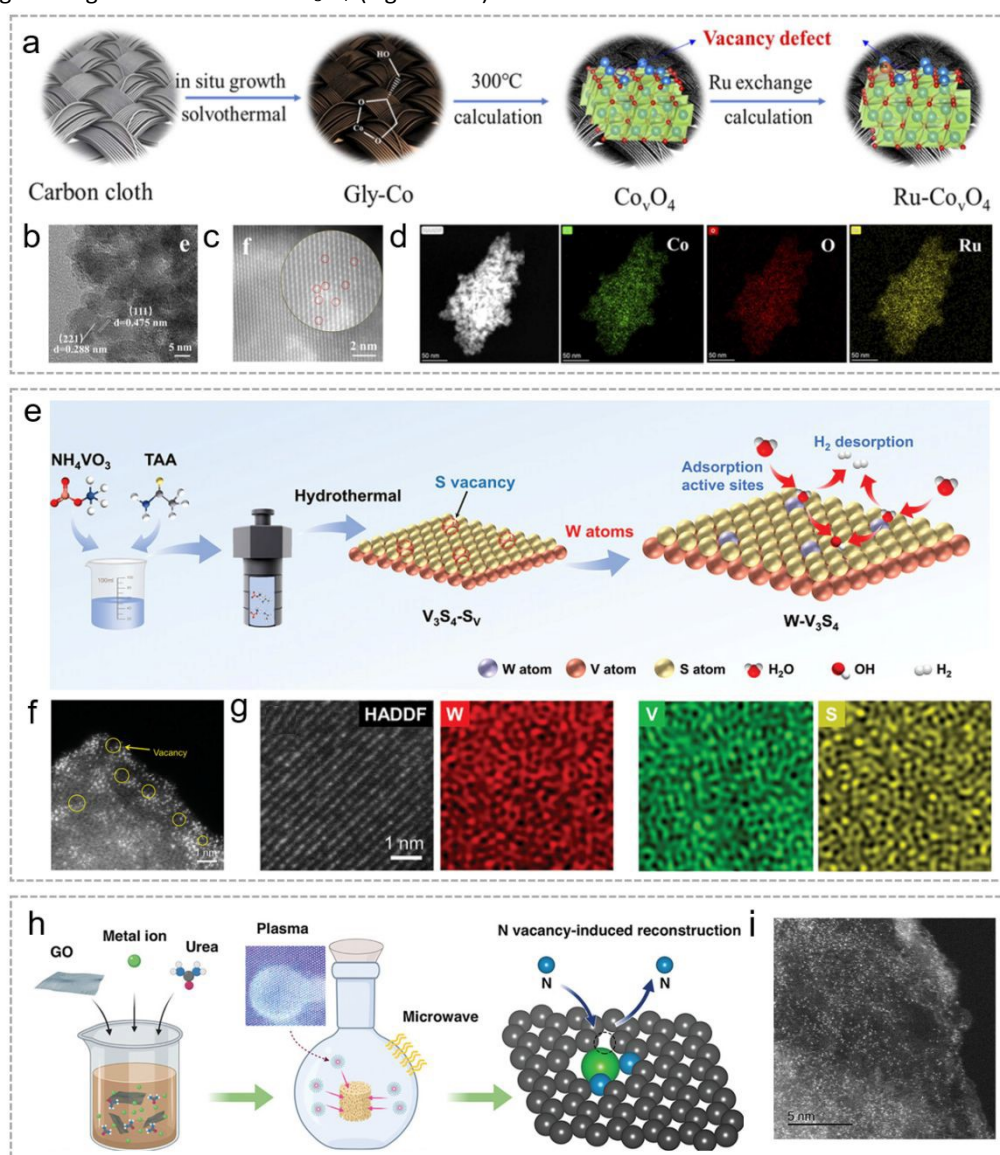


Figure 10. The effect of vacancy on MSI. (a) Synthetic schematic of Ru-Co_vO₄. (b-d) are HRTEM, HAADF-STEM and corresponding elemental maps of Ru-Co_vO₄. Reproduced with permission.⁹⁶ Copyright 2025, Elsevier. (e) Synthetic process schematic for W-V₃S₄ catalysts. (f) HRTEM images of W-V₃S₄. (g) HAADF-STEM image and EDS elemental mapping of W, V, and S elements for W-V₃S₄. Reproduced with permission.⁹⁷ Copyright 2024, Wiley-VCH GmbH. (h) Schematic illustration of microwave induced plasma assisted synthesis for SACs. (i) HAADF-STEM image of SA-NiNG-NV. Reproduced with permission.⁹⁸ Copyright 2021, Wiley.



For anion vacancies, Xi et al.⁹⁷ anchored tungsten (W) single atoms onto sulfur vacancies in ultrathin V₃S₄ nanosheets (W-V₃S₄) (Figure 10e). No distinct W nanoparticles or clusters are detected by HRTEM, confirming the presence of isolated W single atoms and S vacancies dispersed within the V₃S₄ (Figure 10f). Furthermore, HAADF-STEM images, together with corresponding EDS maps, jointly validate the uniform distribution of W, V, and S elements within the V₃S₄ nanosheets (Figure 10g). XPS reveals that the anchoring of W shifts the V 2p peak positively and the S 2p peak negatively, indicating charge redistribution that enhances intermediate adsorption/desorption. DFT calculations verify that W SAs optimize the electronic structure, lower the energy barrier for water dissociation, and improve H* adsorption. As a result, W-V₃S₄ exhibits low overpotential and high stability in alkaline HER, demonstrating the effectiveness of vacancy-anchored single-atom design.

N vacancies can enhance MSI by reconfiguring the coordination environment of the active metal center. Jia et al.⁹⁸ demonstrated a nitrogen vacancy (NV) induced coordinative reconstruction strategy to build highly defective Ni-pyridinic N₂ moieties catalyst (SA-NiNG-NV) (Figure 10h). HAADF-STEM images suggest the homogeneous distribution of Ni atoms across the entire graphene framework in SA-NiNG-NV (Figure 10i). Plasma-induced N removal restructure coordination: Ni coordinated two pyridinic N with two vacancies, forming unsaturated Ni-N₂V₂. XPS and inductively coupled plasma optical emission spectrometer (ICP-OES) show plasma-generated vacancies increased pyridinic N but reduced total N and Ni-N bonds in SA-NiNG-NV, confirming Ni coordination reconfiguration. DFT and XAS indicate this "semi-loose" Ni-N₂V₂ (vs. original Ni-N₃) reduces Ni binding constraints, facilitates CO₂ adsorption/activation, and lowers reduction barriers. SA-NiNG-NV exhibits high intrinsic activity and stability in electrochemical CO₂ reduction. Conversely, Duan et al.⁹⁹ achieved precise tuning by introducing Fe atoms into MoS₂. They designed a bifunctional monolayer with a zoned structure: a core region rich in Mo/S vacancies for superior HER activity, and a surrounding ring region doped with Fe (in 1FeMo and 3FeMo-VS configurations) for excellent OER activity.

From the discussion above, cation vacancies (e.g., Co vacancies) and anion vacancies (such as O, S, and N vacancies) affect the electronic band structure of supported catalysts in different ways. Cation vacancies mainly break the regular periodicity of the cation lattice, which reshapes the local orbital distribution and charge density. This in turn adjusts the valence band position and d-band center of the metal active sites. Anion vacancies, on the other hand, introduce defect levels inside the bandgap. That allows tuning of the Fermi level and the conduction band's electronic structure. The resulting redistribution of electrons also strengthens interfacial electronic coupling, improves charge transfer kinetics, and helps stabilize atomically dispersed metal sites. So even though the two types of vacancies work through different mechanisms, both can reconfigure the electronic band structure, enhance MSI, and together boost the intrinsic activity and structural stability of electrocatalysts.

2.5. Atomic Doping Regulation for MSI

View Article Online

DOI: 10.1039/D6SC02712A

Atomic doping is crucial for regulating MSI. First, electronegativity differences between dopants and metal active sites drive directional interfacial electron transfer,¹⁰⁰ altering metal electron density and d-band center to modulate intermediate adsorption strength, balancing reactant activation and product desorption.¹⁰¹ Second, heteroatoms (e.g., N, S, P) form stable coordination bonds with metal vacant orbitals via lone pairs, anchoring metals to suppress migration/agglomeration and constructing stable active sites.¹⁰² Furthermore, atomic doping promotes phase transformations,¹⁰³ modulates lattice parameters, enhances crystal stability, and improves catalyst durability under harsh conditions.^{104,105}

For anion doping, Precise control of N doping species enables targeted regulation of the spin states of metal single atoms, which subsequently influences catalytic electronic effects. Chen et al.¹⁰⁶ synthesized two kind of Ni SACs with distinct pyridinic-N and pyrrolic-N coordination via rapid Joule heating (Figure 11a). Magnetic characterization shows that pyridinic-N induces a high-spin state in the Ni center, while pyrrolic-N stabilizes a low-spin state. This is confirmed by EPR spectra, where Ni-Npyridinic-C exhibits a strong signal, indicating more unpaired electrons, while the Ni-Npyrrolic-C signal is weaker. PDOS analysis reveals that the high-spin Ni center exhibits more dispersed d-orbital electrons, enhancing orbital delocalization and facilitating stronger hybridization with CO₂ molecules. Crystal orbital hamiltonian population (COHP) analysis further indicates a stronger bonding interaction between the high-spin Ni site and the *COOH intermediate compared to the low-spin counterpart, favoring intermediate adsorption and activation. Consequently, the high-spin catalyst demonstrates superior CO₂ reduction performance. Guo et al.¹⁰⁷ used defect engineering to anchor Ru single atoms on MoS₂ doped with non-metal atoms (X = N, O, F) (Figure 11b). This non-metal coordination effectively tunes electronic structure of Ru, optimizes the HER pathway, and results in Ru-X-MoS₂ catalysts with significantly enhanced hydrogen evolution performance across all pH levels.

Regarding cation doping, Zhang et al.¹⁰⁸ anchored atomically dispersed Co-Cu diatomic pairs onto CeO₂ hollow nanostructures to investigate the effect of introducing another metal on catalyst performance (Figure 11c). In the CoCu@CeO₂ bimetallic catalyst, long-range electronic synergy exists between the Cu and Co sites. Leveraging the appropriate interatomic distance between them, Cu sites induce a directed charge rearrangement, raising the oxidation state of Co sites from +1.86 to +2.25 and shifting the d-band center to -2.37 eV, thereby enhancing the OER activity of the Co sites. Simultaneously, Cu sites act as an ORR active sites, achieving functional differentiation and synergy between the two sites, enabling the catalyst to exhibit an ultra-low OER-ORR potential difference while maintaining both high activity and high stability.

In conclusion, atomic doping enhances catalytic performance by modulating MSI. Key mechanisms include:



regulating electron transfer to optimize the oxidation state and electron density of active sites; constructing stable coordination structures that anchor metal species and suppress sintering;

improving the stability of the support; and inducing favorable transitions in reaction mechanisms.

DOI: 10.1039/D6SC02712A

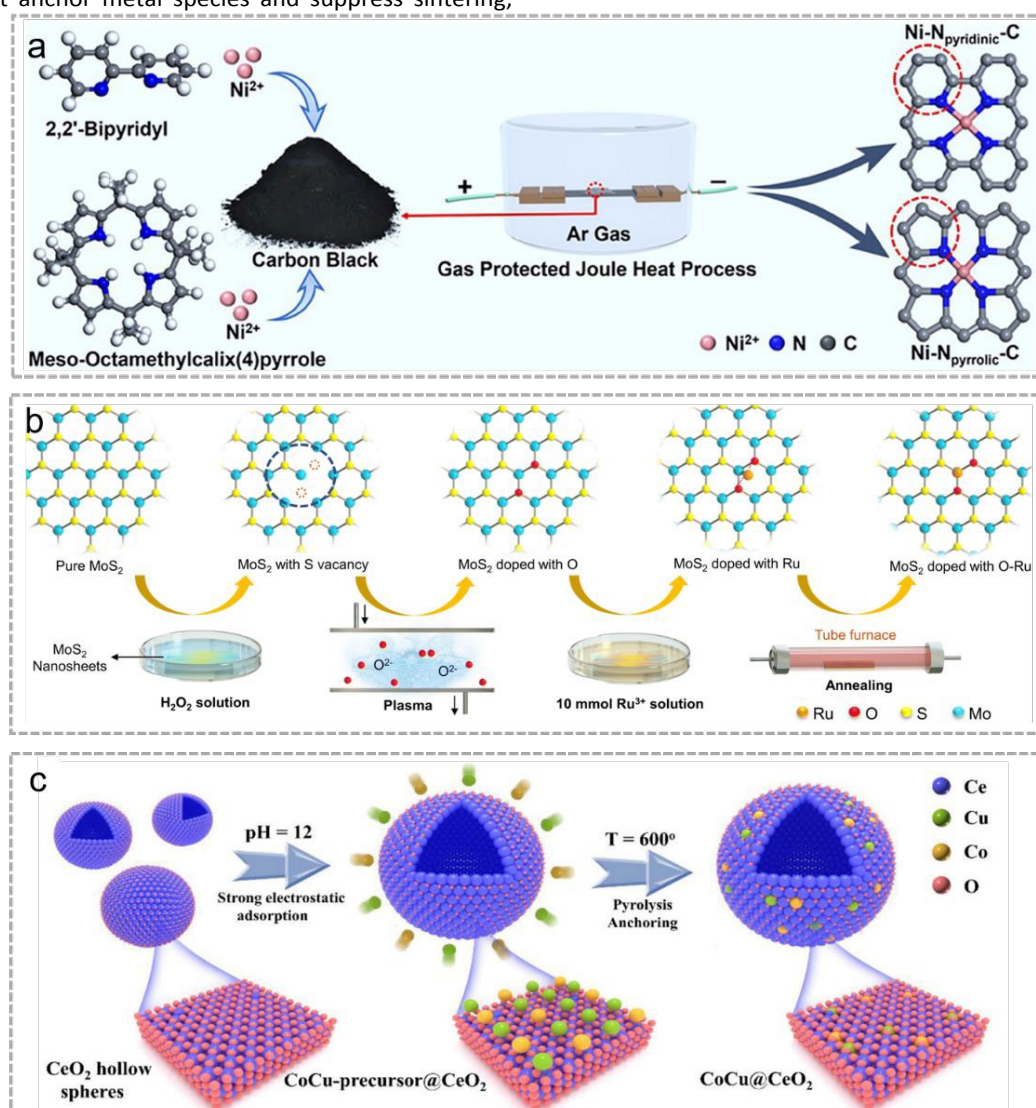


Figure 11. The effect of atomic doping on MSI. (a) Schematic illustration of the synthetic procedure of Ni-Npyrrolic-C and Ni-Npyridinic-C. Reproduced with permission.¹⁰⁶ Copyright 2025, Wiley. (b) Schematic representation of the synthesis process for Ru-O-MoS₂. Reproduced with permission.¹⁰⁷ Copyright 2024, Royal Society of Chemistry. (c) The illustration of the synthetic strategy for CoCu@CeO₂. Reproduced with permission.¹⁰⁸ Copyright 2025, Wiley.

2.6. Quantitative descriptors for MSI strength

In electrocatalytic systems, MSI plays a central role, but how to accurately quantify its strength remains a key challenge. Therefore, it is important to systematically review and discuss the current computational descriptors for MSI strength.

Binding energy is a fundamental thermodynamic parameter that describes the interfacial interaction between metal active centers and the support. It is defined as the energy difference between the metal-support composite and the sum of the isolated support and isolated metal. Physically, it is the minimum energy needed to completely detach a metal unit from the support surface, reflecting contributions from physical adsorption, chemical bonding, interfacial strain, and spatial confinement. Generally, the more negative the binding energy (i.e., the larger its absolute value), the more stable

the metal–support combination and the stronger the MSI. However, this descriptor only captures the static ground state and fails to account for dynamic effects such as applied potential, solvation, or reaction intermediates. Also, for complex supports like amorphous or highly defective materials, model construction can introduce significant errors.

Integrated Crystal Orbital Hamilton Population (ICOHP) is a key indicator for quantifying interfacial chemical bond strength at the electronic level. It is obtained by integrating the bonding and antibonding states of orbital interactions between metal and support atoms at the interface. Physically, it reflects the filling of interfacial bonding orbitals and the strength of covalent interactions, allowing distinction between ionic, covalent, and mixed bonding. A more



negative ICOHP value indicates stronger bonding and orbital coupling between the metal and support, hence stronger MSI. It works particularly well for typical interfacial bonds such as M-O, M-S, M-N, and M-C. The main drawbacks are its high dependence on precise electronic structure calculations (leading to high computational cost for complex interfaces) and the difficulty of capturing the dynamic evolution of MSI during reactions.

Bader charge transfer is calculated by integrating the spatial charge density around atoms, giving the net electron transfer between metal and support. Physically, it represents the extent of interfacial electron redistribution, directly reflecting the electronic coupling strength in MSI. The larger the absolute charge transfer, the stronger the electronic regulation of the metal center by the support, and the stronger the MSI. This descriptor is intuitive for electronically dominated MSI and applies to various systems including single atoms, clusters, and nanoparticles. Its main limitation is that it cannot easily separate the contributions of electron transfer from long-range electrostatic interactions.

The d-band center shift referenced to the Fermi level quantifies the displacement of the d-band center of metal active sites induced by the support. Physically, d-band center shift measures the modulation of the metal's electronic structure by the support, and serves as a key link between MSI and the adsorption behavior of reaction intermediates. A larger absolute shift means the electronic structure of the metal sites is more strongly affected by the support, indicating a stronger MSI effect on the electronic state. This descriptor can directly establish structure-activity relationships between MSI and catalytic performance, but it is only valid for transition metal active centers. Moreover, the shift is not strictly linear with MSI strength and can be influenced by factors such as coordination environment and spin state.

Metal atom diffusion barrier refers to the energy barrier that a single metal atom must overcome to migrate or aggregate on the support surface. Physically, it represents the anchoring ability and spatial confinement effect of the support, directly linking MSI to catalyst stability. A higher diffusion barrier means metal atoms are less likely to migrate and aggregate, indicating a stronger anchoring effect and a more pronounced stabilization role of MSI. This descriptor measures the ability of MSI to maintain dispersion of active sites from a kinetic perspective. However, it only reflects geometric confinement and kinetic stabilization, not chemical interactions like electronic coupling or orbital hybridization. Also, the calculated values depend heavily on the choice of crystal facets, defects, and adsorption sites, making it difficult to represent the average behavior of the whole catalyst.

3. Various Catalytic Applications of MSI

3.1. Application of MSI in Catalytic Water Splitting

Water-splitting hydrogen production technology has garnered significant attention for enabling sustainable hydrogen generation.¹⁰⁹⁻¹¹² Electrocatalytic HER commonly employs metal elements categorized into precious metals and non-precious metals.^{113,114} Current research trends focus on reducing precious metal usage and enhancing non-precious metal performance. Through precise design of MSI, researchers aim to simultaneously decrease precious metal consumption while improving the catalytic

activity and stability of non-precious metal systems. This approach offers novel insights for developing highly efficient HER catalysts.

Meng et al.¹¹⁵ successfully synthesized a novel single-atom Pt catalyst (Pt SACs-NiCrO₃/NF) by anchoring Pt atoms onto a NiCrO₃ support to achieve high-density uniform dispersion. The MSI in this catalyst induces electron transfer from Ni/Cr to Pt, optimizing the interfacial electronic structure and regulating the catalytic microenvironment: the NiCrO₃ support promotes water dissociation (Volmer step), while the near-acidic microenvironment formed by Pt single atoms accelerates the proton-involved Tafel step (Figure 12a). This synergistic effect significantly enhances alkaline HER performance, achieving overpotentials as low as 23 and 122 mV at 10 and 100 mA cm⁻² current densities, respectively, with a mass activity of 382.77 mA mg⁻¹_{Pt} and excellent stability over 100 h.

Recent studies have reported a Pt SAC synergistically stabilized by chlorine Cl and Ru-NPs (Pt₁Cl_{0.5}/Ru-NPs@RuO_x)¹¹⁶. The strong electronegativity of Cl synergistically regulates coordination environment and electronic structure of Pt with electron-donating properties of Ru, forming a dynamically stable Pt-Cl-Pt framework while enhancing Pt stability and optimizing d-band electronic states. This catalyst demonstrated stable operation for 1000 h in PEMWE (Figure 12b). Wang et al.¹¹⁷ synthesized low-crystalline Ru-LC-Ni(OH)₂ and high-crystalline Ru-HC-Ni(OH)₂ with single-atom Ru by controlling the crystallinity of nickel hydroxide supports (Figure 12c). The Ru-LC-Ni(OH)₂ catalyst exhibits disordered atomic arrangement, abundant defects, and metallic vacant bonds, enhancing MSI and facilitating electron transfer from the carrier to Ru to form low-oxidation-state Ru active sites. Simultaneously, it optimizes the local microenvironment, promoting H₃O⁺ aggregation at the interface to create a localized acidic environment, thereby enhancing water dissociation capacity and HER kinetics. Zhang et al.¹¹⁸ synthesized a single-atom Ru-doped cobalt oxide (Ru SA/Co₃O₄). The spinel structure of Co₃O₄ enables uniform dispersion of Ru single atoms, forming atomically dispersed Ru-Co synergistic active sites. MSI suppress Ru agglomeration while regulating the electronic structure and coordination environment of Co₃O₄. Ru sites promote water adsorption/dissociation and OH⁻ desorption, while Co sites optimize H* adsorption and H₂ evolution (Figure 12d). Kim et al.¹¹⁹ synthesized Ni₁-NOMHC SACs via a dual-template approach, using N/O co-doped ultrathin mesoporous hollow carbon as the support (Figure 12e). The unique N₂O₂ coordination environment optimizes electronic structure of Ni, enhancing dispersion, stability, and mass transfer efficiency, resulting in outstanding HER performance.

The hydrogen spillover effect offers a strategy to circumvent the thermodynamic constraints of conventional volcano plots. Zhao et al.¹²⁰ developed an in situ electrochemical reconstruction method to tailor hydrogen spillover pathways, as demonstrated on a Ru/WO_x catalyst with intrinsic spillover behavior. In situ characterization and control experiments reveal that Ru species undergo dynamic oxidation during the HER. Concurrently, the MSI between Ru and WO_x accelerates proton conversion and intercalation into the WO_x lattice. Theoretical calculations further show that in situ reconstruction modulates interfacial charge density via MSI, lowering the thermodynamic barrier for hydrogen migration and creating thermoneutral RuO_x/WO₂ interfacial sites. Benefiting from the optimized electronic coupling and an unobstructed spillover



pathway, the catalyst delivers an overpotential of 317 mV at 1000 mA cm⁻² in alkaline media, alongside outstanding

long-term stability exceeding 500 h.

View Article Online
DOI: 10.1039/D6SC02712A

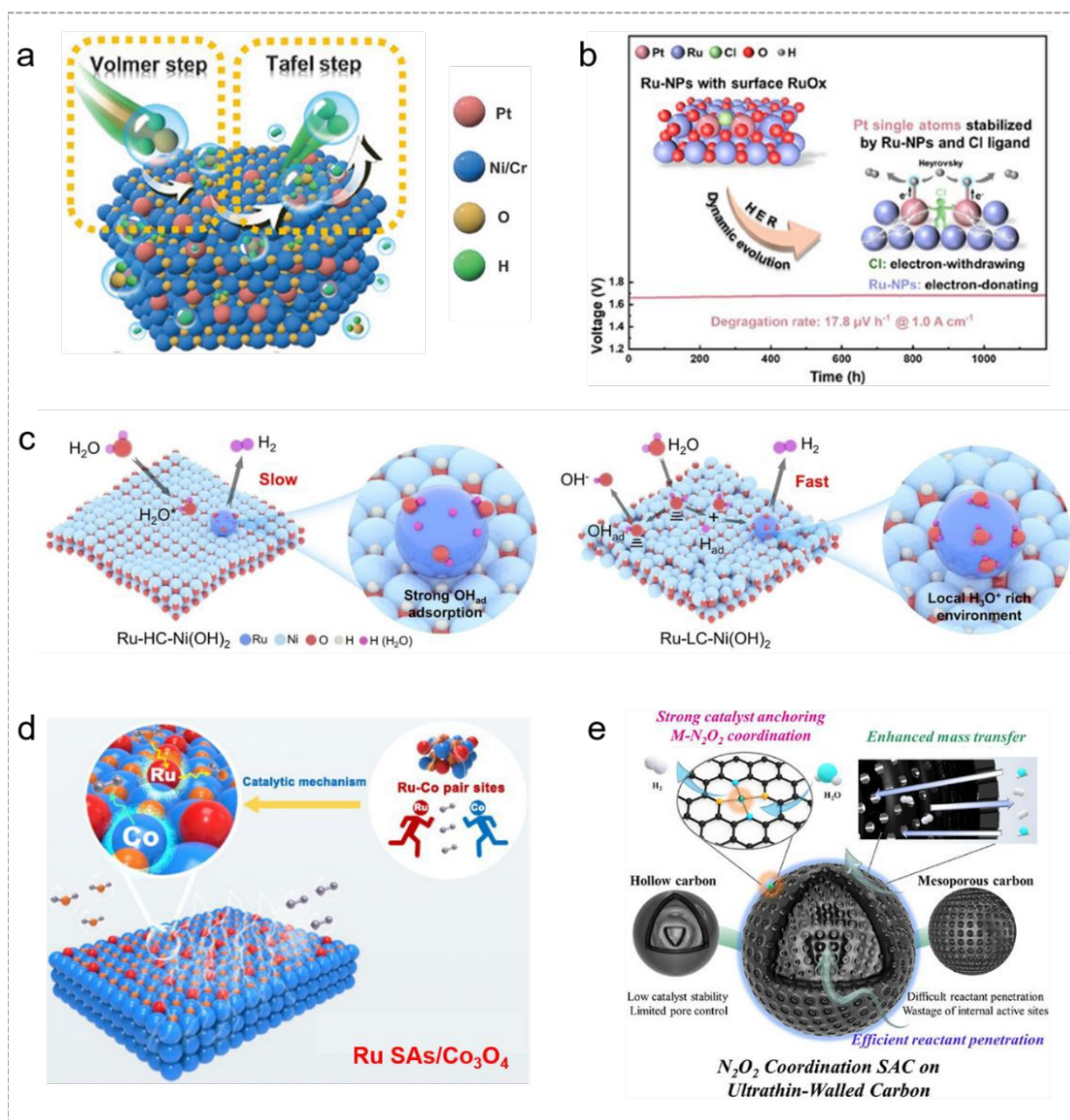


Figure 12. Application of MSI in the HER. (a) Schematic illustration of the dynamic proton-concentrated catalyst surface. Reproduced with permission.¹¹⁵ Copyright 2024, Wiley. (b) Pt single atom, synergistically stabilized by Cl ligand and Ru support, exhibits excellent stability over 1000 h of PEM water electrolysis. Reproduced with permission.¹¹⁶ Copyright 2025, Wiley. (c) Schematic diagram of microenvironmental changes on Ru-LC-Ni(OH)₂ and Ru-HC-Ni(OH)₂. Reproduced with permission.¹¹⁷ Copyright 2024, Wiley. (d) Ru sites can effectively accelerate water adsorption/dissociation and OH⁻ desorption, whereas the Co sites are favorable for H* adsorption and H₂ evolution. Reproduced with permission.¹¹⁸ Copyright 2025, American Chemical Society. (e) The N₂O₂ coordination fine-tunes the electronic structure of Ni, promoting efficient hydrogen adsorption and evolution. Reproduced with permission.¹¹⁹ Copyright 2025, American Chemical Society.

For OER, SACs are categorized into precious metals (represented by Ir and Ru, with inherently high activity) and non-precious metals (transition metals such as Fe, Co, Ni, with Co/Ni-based systems being the most extensively studied). Research on noble metal SACs, Kumar et al.¹²¹ modulated the coordination environment of Ir single atoms on NiO surfaces to enhance MSI. Embedded Ir (Ir_{emb}-NiO) exhibits stronger Ir-Ni secondary coordination layer interactions than adsorbed Ir (Ir_{ads}-NiO), stabilizing Ir single atoms and promoting LOM (Figure 13a). Under alkaline conditions, the overpotential is 256 mV@10 mA cm⁻² and a degradation rate is 1 mV h⁻¹, outperforming

commercial IrO₂ and Ir_{ads}-NiO (Figure 13b). Wang et al.¹²² prepared Ru@d-NiFe LDH via coprecipitation, forming OO-Ru-OH coordination on the surface while constructing a Ru-O-Ni/Fe network in the bulk; MSI reduce LOM and adsorbate evolution mechanism (AEM) energy barriers, enabling pathway synergy with a 230 mV overpotential at 10 mA cm⁻² and a 78 μV h⁻¹ decay rate at 250 mA cm⁻² (Figure 13c-d).

Hou et al.¹²³ constructed a Ni SAC on oxygen-doped Mo₂C (Ni_{SA}-O/Mo₂C). The Ni-O-Mo bridging structure enable MSI to regulate Ni electronic structure and optimize intermediate adsorption energy. During HER, Ni remains atomically dispersed, while Ni-O-Mo bonds



break and reconfigure into Ni-O-Ni clusters during OER, further lowering the energy barrier. This reveals the regulatory role of MSI dynamic evolution, demonstrating outstanding bifunctional activity (HER and OER) under alkaline conditions (Figure 13e-f). Transition metals single-atom doping of precious metal oxides represents an efficient design strategy, centered on regulating performance through MSI. Reports indicate that the single-atom Mn-doped Ru/RuO₂ heterostructure catalyst (Mn(SAs)-Ru/RuO₂)¹²⁴ enables charge redistribution between Ru and RuO₂, bringing ΔG_{H^*} close to ideal values (partially surpassing Pt benchmarks) (Figure 13g), precisely controlling hydrogen intermediate adsorption energy,

while simultaneously optimizing Ru site adsorption of OOH* comprehensively enhancing HER/OER kinetics. At 10 mA cm⁻², the overpotentials for HER and OER are reduced to 39 mV and 158 mV, respectively, with stability exceeding 500 h in 0.5 M H₂SO₄ (Figure 13h). Xiao et al.¹²⁵ employed an electrochemical disproportionation strategy to in situ fill MnO₂ cation vacancies with Ru atoms, forming stable Ru-O/Ru-Mn coordination. This enhances MSI to optimize Ru electronic structure and suppress aggregation. The catalyst exhibits 44-fold higher mass activity than commercial RuO₂ and excellent high-current-density stability.

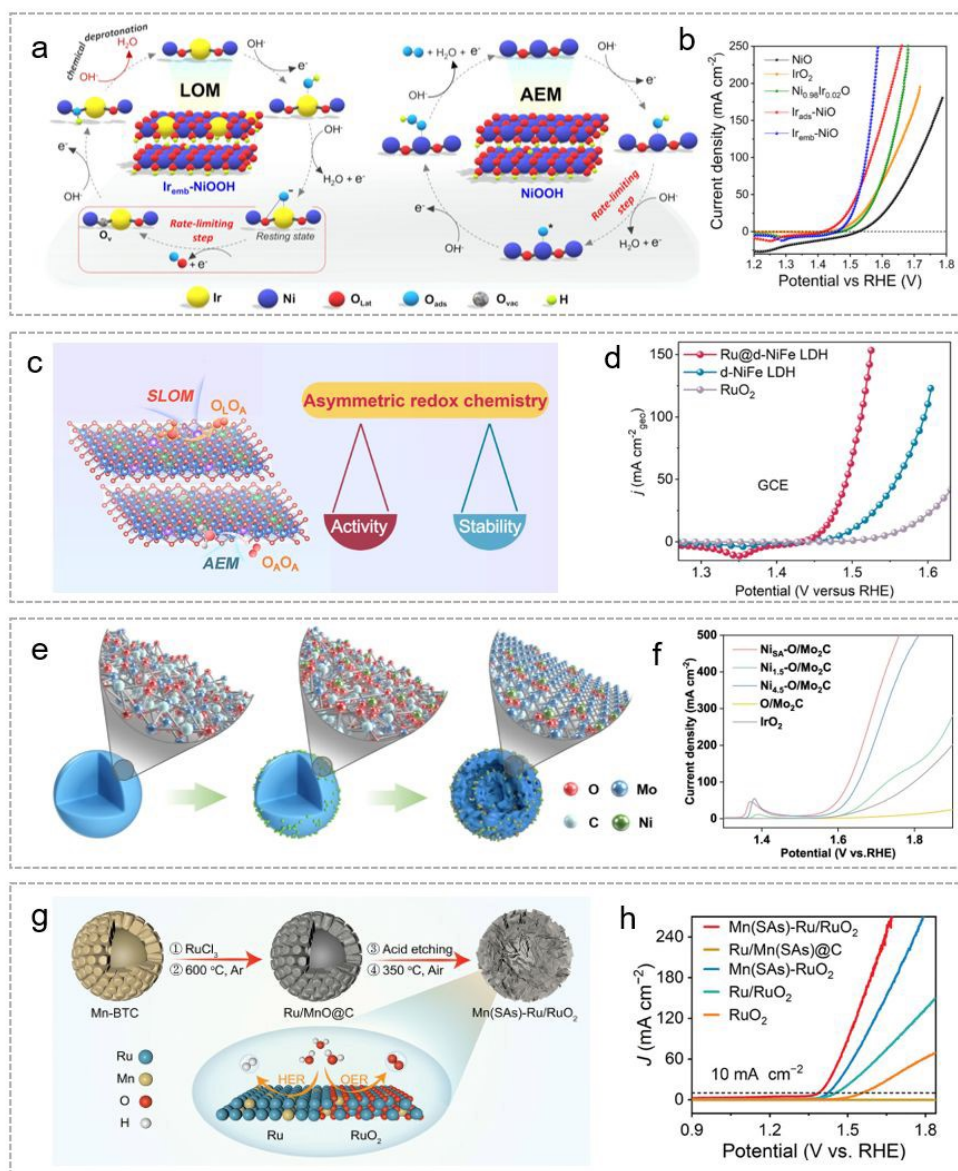


Figure 13. Application of MSI in the OER. (a) Proposed schematic illustration of the LOM process for Ir_{emb}-NiO (reconstructed to Ir_{emb}-NiOOH) and the AEM process for NiO (reconstructed to NiOOH). (b) OER LSV polarization of Ir_{emb}-NiO. Reproduced with permission under CC-BY 4.0.¹²¹ Copyright 2024, American Chemical Society. (c) Proposed schematic illustration of Ru@d-NiFe LDH. (d) LSV curves at 2 mV s⁻¹ of Ru@d-NiFe LDH. Reproduced with permission.¹²² Copyright 2025, Elsevier. (e) Schematic illustration of the fabrication process of the Ni_{SA}-O/Mo₂C electrocatalyst. (f) Polarization curves for Ni_{SA}-O/Mo₂C. Reproduced with permission.¹²³ Copyright 2024, Springer Nature. (g) Schematic illustration for the synthesis of Mn(SAs)-Ru/RuO₂. (h) LSV curves of electrocatalysts. Reproduced with permission.¹²⁴ Copyright 2024, Wiley.

Li et al.¹²⁶ used an atomic-level Fe doping strategy to precisely control the in situ crystalline phase reconstruction of δ -MnO₂ during

the OER. They find that pristine δ -MnO₂ transforms into the poorly active γ -MnOOH phase under an applied potential. In contrast,



single-atom Fe introduces asymmetric Fe-O-Mn bonds, establishing MSI that induce lattice distortion in MnO₂ and facilitate electron transfer from Fe to Mn. This increases the Mn³⁺ content and enhances oxygen spillover, steering the reconstruction toward the highly active α -MnOOH phase. During the OER, the MSI effect progressively reinforces with ongoing surface reconstruction, continuously optimizing the interfacial electronic structure and intermediate adsorption energies, and substantially lowering the energy barrier of the rate-determining step (RDS). Consequently, the catalyst exhibits far superior OER activity in alkaline media compared to pristine MnO₂ and commercial RuO₂.

In water splitting, MSI is a key strategy for boosting HER and OER performance by fine-tuning active sites. For HER, MSI tunes the electron density and d-band center of metal sites through directed charge transfer at the interface. This speeds up water dissociation in alkaline media, balances the adsorption and desorption of H*, and cuts down the overpotential. For OER, MSI adjusts the valence state and coordination environment of metal centers to improve the binding of key intermediates, and also allows flexible switching between different OER pathways. Under operando conditions, MSI evolves dynamically-driven by the applied potential or structural reconstruction-which continuously improves interfacial charge transfer, stabilizes active sites, and preserves high intrinsic activity. That is reason that MSI is essential for achieving both high-performance and long-term stability.

3.2. Application of MSI in Fuel Cells

The hydrogen oxidation reaction (HOR) at the anode and the oxygen reduction reaction (ORR) at the cathode, as the core reactions of fuel cells, are the key elementary reactions governing energy conversion. While the HOR proceeds at a relatively fast rate, it is still regulated by catalyst surface adsorption and charge transfer efficiency.^{127,128} In contrast, the ORR is inherently limited by multi-step reaction intermediates and slow electron transfer, making it the rate-limiting step for the overall performance of fuel cells.¹²⁹⁻¹³² MSI as a strategy for regulating the electronic and geometric structures of catalysts, play a crucial role in HOR and ORR catalysis. By precisely controlling the electronic states of metal active sites, the charge transfer efficiency at the metal-support interface, and the coordination environment and exposure of active sites, MSI can optimize the H adsorption/desorption equilibrium during HOR and precisely regulate the binding energies of key intermediates such as OOH, *O, and *OH during ORR, thereby simultaneously enhancing the charge transfer rate of HOR and the reaction kinetic efficiency of ORR.^{133,134}

In alkaline HOR, SACs have garnered significant attention due to their high activity and tunable MSI. Zhang et al.¹³⁵ employed a salt-assisted coordination symmetry regulation strategy to transform ZIF-8 tetrahedral coordination into planar square coordination, yielding 2D Pt SAC (Figure 14a). Multidimensional enhancement of MSI: Increasing pyridine nitrogen content to 90% provides uniform anchoring sites, while high-temperature carbonization-induced hexagonal ring defects increase active site density and optimize Pt d-band centers. This catalyst exhibits enhanced stability and electron transfer efficiency, achieving an alkaline HOR mass activity of 2396 A g_{Pt}⁻¹. Wang et al.¹³⁶ synthesized a Pd single-atom embedded in Ni₃N catalyst (Pd₁/Ni₃N), forming Pd₁-Ni₆ hexagonal coordination and

Pd₁Ni₂ trimer sites. Pd replaces Ni atoms on the Ni₃N surface to create atomically dispersed sites (Figure 14b). The introduction of Pd induces electron transfer from Ni and N to Pd, modulating the d-band center. A unique adsorption pattern (*H adsorbed at Pd₁Ni₂-H_v sites and *OH adsorbed at Pd₁Ni₂-H_n sites) mitigates the overly strong *H/*OH adsorption inherent to pristine Ni₃N, thereby enhancing catalytic performance. It exhibits outstanding intrinsic activity and mass activity, achieving a high power density of 31.7 W mg_{Pd}⁻¹ at an ultra-low Pd loading. Han et al.¹³⁷ prepared Ir cluster/ α -MoC_{1-x} catalysts (Ir/ α -MoC_{1-x}), where Ir clusters and the support form SMSI via Ir-Mo bonds (Figure 14c-d). Electron transfer from the support to Ir reduces the Ir oxidation state, weakens *H adsorption energy at Ir sites, and enhances *OH adsorption capacity at Mo sites, optimizing HOR kinetics. Its mass-normalized exchange current density reaches 320 mA mg⁻¹, outperforming conventional Ir/ β -Mo₂C and commercial Pt/C catalysts. Zhang et al.¹³⁸ anchored Ru single atoms onto oxygen-rich vacancy-doped ZrO_{2-x}/C supports (Ru-SA-ZrO_{2-x}/C). The MSI suppress Ru agglomeration, optimize hydrogen/hydroxyl binding energies to lower the HOR energy barrier, and modulate the d-band center to weaken CO adsorption, conferring exceptional CO tolerance. Ru-SA-ZrO_{2-x}/C exhibits the highest HOR activity across the entire potential range (Figure 14e).

Ren et al.¹³⁹ employed a single-atom alloy (SAA) with carbon encapsulation dual-modulation strategy to prepare a core-shell NiPt_{SA}@NC catalyst. Pt acquires electrons from Ni to form an electron-rich center, driving electron transfer to the carbon shell and shifting the Ni d-band center downward. This catalyst exhibits an alkaline HOR specific activity of 82.0 μ A cm⁻² and maintains 92% stability after 3000 cycles (Figure 14f). Many high-performance catalysts achieve their activity through the synergistic interplay of multiple interactions. For SAA systems, it is important to distinguish between the electronic synergy within the active site itself and that between the active site and the support. In NiPt_{SA}@NC, for example, charge polarization occurs between the isolated Pt atoms and the surrounding Ni host: Pt gains electrons from Ni, resulting in an electron-rich Pt center and an electron-deficient Ni surface. This electronic modulation shifts the Ni d-band center moderately downward, weakening its overly strong hydrogen adsorption and optimizing the hydrogen binding energy, which in turn leads to more favorable hydrogen oxidation reaction kinetics. Between the active site and the support, electrons transfer from the metal core to the carbon shell, further stabilizing the electronic state of the Ni sites. At the same time, the porous carbon shell acts as a protective layer, suppressing Ni oxidation and structural degradation, while also enhancing interfacial water adsorption and facilitating water dissociation.

He et al.¹⁴⁰ constructed a PtIr-Co_{0.05}NC catalyst anchored at Co-N₄ sites on a nitrogen-doped carbon substrate. Co-N₄ acts as an "electronic bridge" to promote electron transfer between PtIr clusters and the support, enhancing electronic coupling, optimizing *H adsorption free energy (-0.16 eV), and reducing the Volmer energy barrier for the basic HOR rate-determining step from 0.26 eV to 0.06 eV. This catalyst achieves a current density of at a potential of 2.59 mA cm⁻² at a potential of 50 mV, much higher than that of Co-free PtIr-NC (Figure 14g).



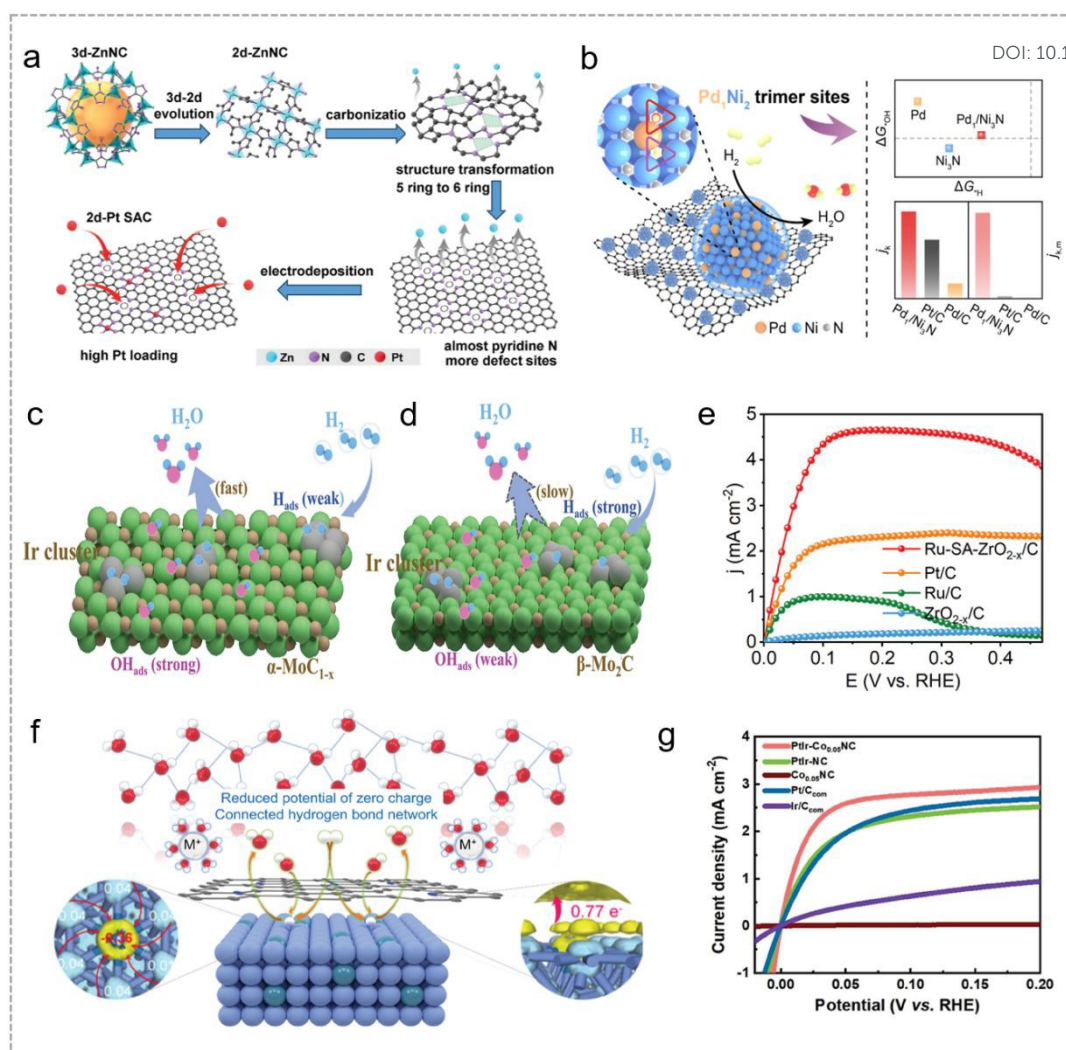
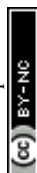


Figure 14. Application of MSI in the HOR. (a) Schematic diagram of the mechanism of 3D–2D evolution and the corresponding carbonization process. Reproduced with permission.¹³⁵ Copyright 2024, Wiley. (b) Schematic illustration for the synthesis of Pd₁/Ni₃N. Reproduced with permission.¹³⁶ Copyright 2025, American Chemical Society. (c) Predicted schematic diagram of the alkaline HOR process on synergistic Ir/α-MoC_{1-x}. (d) Predicted schematic diagram of the alkaline HOR process on synergistic Ir/β-Mo₂C. Reproduced with permission.¹³⁷ Copyright 2024, Wiley. (e) HOR polarization curves of Ru-SA-ZrO_{2-x}/C, Pt/C, Ru/C, and ZrO_{2-x}/C. Reproduced with permission.¹³⁸ Copyright 2025, Wiley-VCH GmbH. (f) Schematic illustration of the alkaline HOR mechanism on NiPt_{SA}@NC. Reproduced with permission.¹³⁹ Copyright 2024, Wiley. (g) Geometric area-normalized polarization curves in H₂-saturated 0.1 M KOH solutions. Reproduced with permission.¹⁴⁰ Copyright 2025, Wiley.

Regarding the role of MSI in the ORR reaction. Zhou et al.¹⁴¹ prepared a dynamically tunable Pt single-atom ORR catalyst (Pt₁-CuO_x/Cu) via an in situ partial oxidation strategy, anchoring Pt atoms onto a CuO_x/Cu hybrid support with adjustable oxidation states to achieve MSI dynamic optimization (Figure 15a). CuO_x/Cu functions as an “oxidation-reduction electron reservoir,” reversibly modulating the Cu⁰/Cu²⁺ oxidation state during ORR. It dynamically donates electrons to the Pt 5d orbital (elevating Pt electrons by 0.53) and induces the formation of a low-coordination structure, precisely regulating *OOH adsorption energy. This catalyst exhibits over 97% four-electron selectivity with a mass activity of 6.1 A mg⁻¹ (three times that of commercial Pt/C) and maintains stable performance over 100 h of stability testing (Figure 15b-c). Yang et al.³⁸ synthesized a high-valent Ir SAC (Ir_{SA}-MnO_x) via room-temperature impregnation-adsorption. Ir atoms are highly dispersed on MnO_x hollow nanospheres bearing Mn cation vacancies. The Mn vacancies provide

anchoring sites for Ir and enhance MSI, enabling Ir to adopt a highly oxidized state and form a stable IrO₆-Mn vacancy coordination structure (Figure 15d). This catalyst efficiently catalyzes ORR via a four-electron pathway, exhibiting outstanding half-wave potential and ultra-high stability, surpassing commercial Pt/C in performance (Figure 15e).

Zhang et al.¹⁴² synthesized first-coordination-shell sulfur-doped Fe₁N-C and second-coordination-shell sulfur-doped Fe₁N-SC catalysts, regulating MSI through coordination environment control. Fe₁N-SC, featuring second-coordination-shell sulfur doping, more effectively modulates the electronic structure of the Fe center and reduces the *OH desorption energy barrier, resulting in outstanding ORR performance. A liquid ZAB was assembled using Fe₁N-SC as the cathode catalyst, achieving an open circuit potential (OCP) of 1.46 V, outperforming Pt/C-based zinc-air batteries. Voltage-current polarization curves and corresponding power density curves



demonstrate that FeN-SC exhibits outstanding performance as a cathode catalyst (Figure 15f-h). Luo et al.¹⁴³ prepared single-atom manganese catalysts MoP@Mn_{SAC}-NC, regulating Mn spin states by embedding MoP nanocrystals within nitrogen-doped carbon frameworks. MSI facilitates electron transfer from Mn to MoP, where strong interactions between MoP and Mn-N₄ sites convert Mn spin

states from low-spin (S=1/2) to high-spin (S=5/2), optimizing O₂ adsorption and *OOH/*OH adsorption/desorption processes. It exhibits outstanding alkaline ORR activity, achieves a nearly complete 4e⁻ pathway, and demonstrates exceptional stability, which are attributed to MoP-induced electronic regulation (Figure 15i-k).

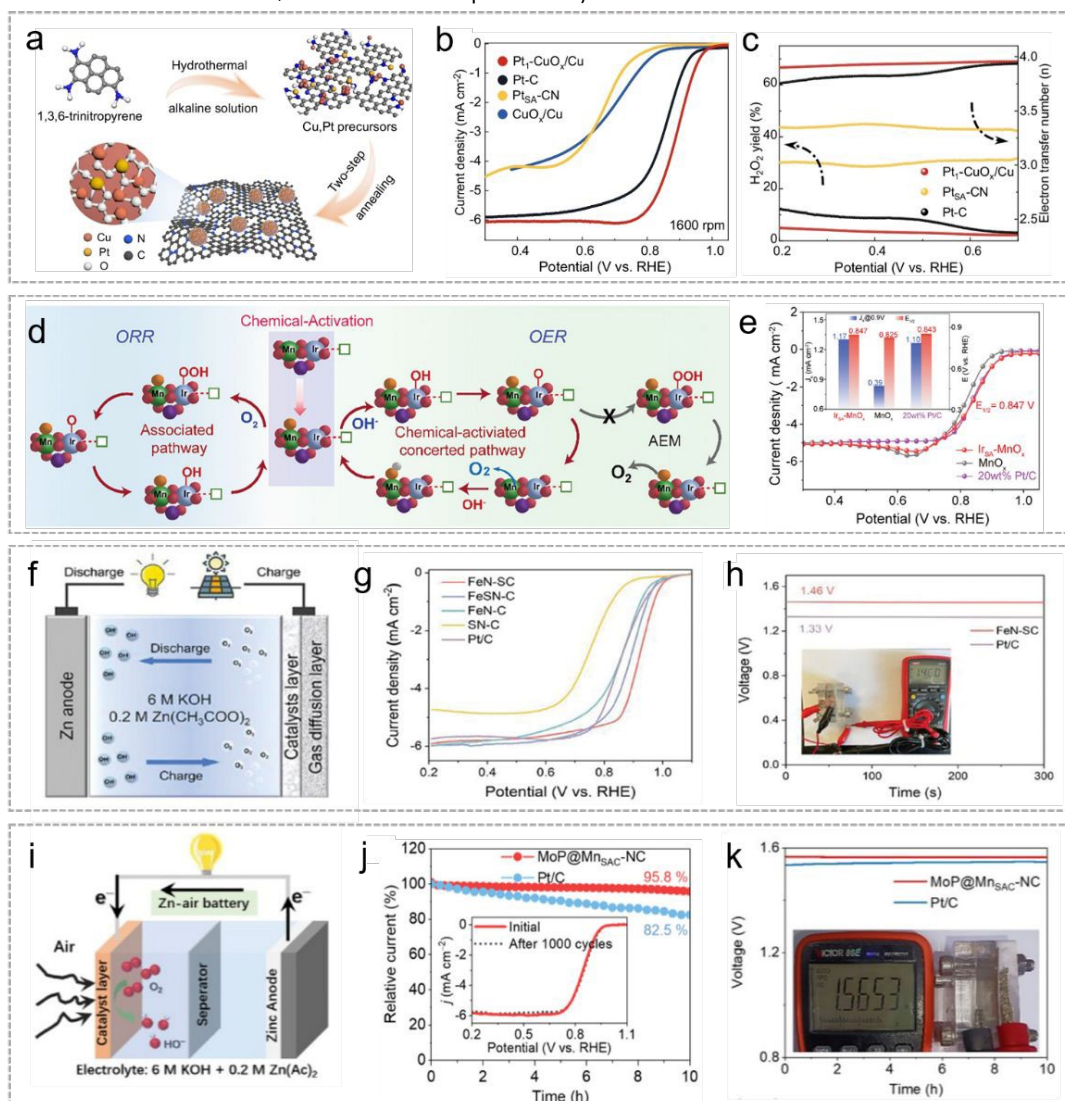


Figure 15. Application of MSI in the ORR. (a) The Pt₁-CuO_x/Cu dispersed on carbon nanosheets was synthesized through sequential hydrothermal and pyrolytic processes. (b) LSV curves of Pt₁-CuO_x/Cu, Pt-C, Pt_{SA}-CN and CuO_x/Cu samples. (c) The selectivity parameters of ORR pathway for the catalysts involved. Reproduced with permission.¹⁴¹ Copyright 2024, Springer Nature. (d) The scheme of the possible independent associated 4e⁻ pathway for ORR and chemical activated concerted pathway for OER on Ir_{SA}-MnO_x. (e) ORR polarization curves of Ir_{SA}-MnO_x. Reproduced with permission.³⁸ Copyright 2024, Wiley. (f) Schematic of ZABs. (g) LSV curves of FeN-SC. (h) OCP of FeN-SC and Pt/C. Reproduced with permission.¹⁴² Copyright 2025, Wiley. (i) Schematic diagram of the liquid-state ZAB. (j) Discharge polarization curves and corresponding power density curves. (k) Open circuit voltage plots of MoP@Mn_{SAC}-NC (inset shows photography of OCV of the liquid-state ZAB). Reproduced with permission.¹⁴³ Copyright 2025, Wiley.

During the ORR, single atom sites often undergo structural reconstruction. Tong et al.¹⁴⁴ designed a Mn-SAS catalyst with a well-defined Mn-N₄ configuration and used operando synchrotron radiation to track the evolution process of the Mn sites on the support under ORR conditions. As the potential is applied, the Mn-N₄ structure first turns into Mn-N₃C and then into Mn-N₂C₂. Meanwhile, the Mn valence state rises from +3.0 to +3.8 and later drops to +3.2. When the potential is removed, the catalyst returns to its original

Mn³⁺-N₄ configuration. This stepwise evolution improves both the electronic and geometric structures of the active centers. The generated Mn^{3.8+}-N₃C configuration favors O₂ adsorption, while the Mn^{3.2+}-N₂C₂ structure reduces the energy barrier of the rate-determining step. As a result, the catalyst delivers an onset potential of 0.99 V and exhibits remarkable stability over 10 000 cycles.

In fuel cells, the HOR and ORR are key processes determining overall performance. The MSI has emerged as a core strategy for



enhancing catalyst performance by precisely regulating the electronic structure, coordination environment, and interfacial properties of active sites. For HOR, MSI optimizes the d-band center and surface electron density of metal sites, thereby balancing the adsorption and desorption energy barriers of reaction intermediates and enhancing resistance to poisoning by impurities such as CO. For ORR, MSI can adjust the valence state and local coordination structure of active sites, promoting the four-electron reaction pathway while suppressing H₂O₂ formation. It also reduces reaction energy barriers by optimizing the adsorption strength of key intermediates such as *OOH and *OH. Concurrently, MSI strengthens electron coupling between the metal-supported and support, effectively enhancing the half-wave potential, kinetic current density, and cycling durability, providing crucial guidance for designing high-performance fuel cell catalysts.

3.3. Application of MSI in CO₂RR

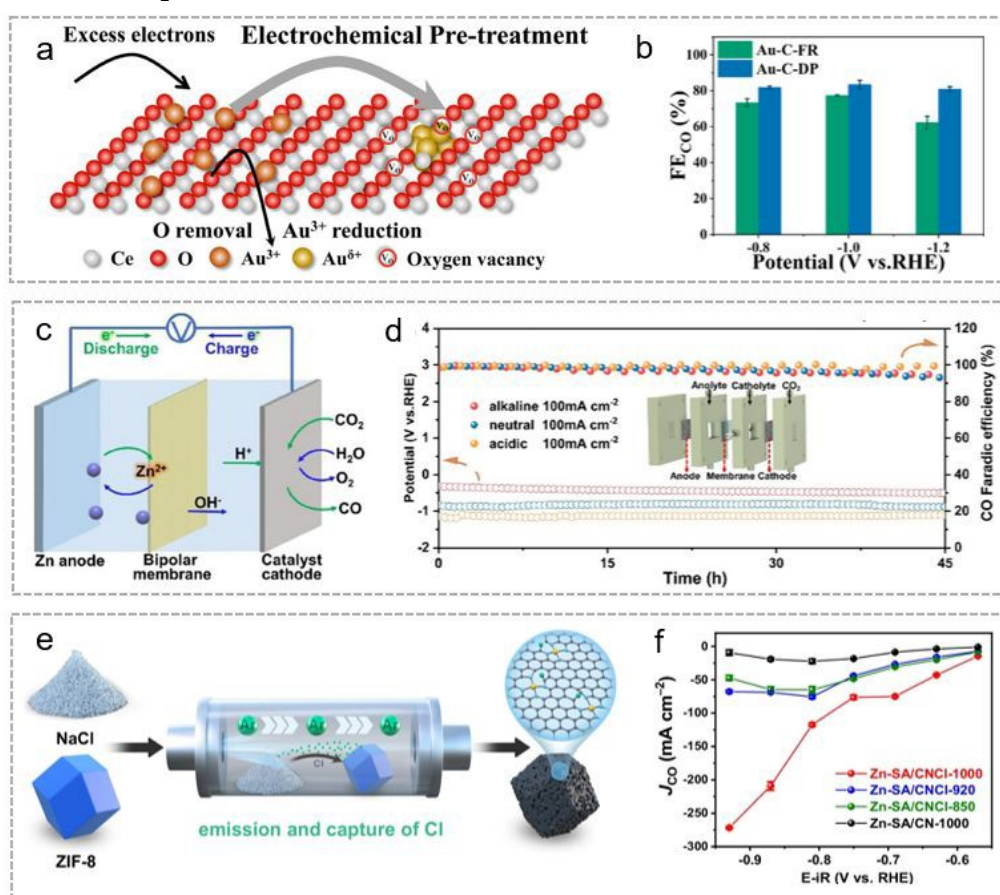


Figure 16. Application of MSI in the CO₂RR. (a) Illustration of the CO₂RR mechanism over Au-CeO₂-DP. (b) CO FE of Au-C-FR and Au-C-DP catalysts. Reproduced with permission.¹⁵³ Copyright 2022, American Chemical Society. (c) Schematic illustration of a primary aqueous Zn–CO₂ battery. (d) Durability test of Ni-N_{pyridinic}-C in flow-cell and schematic illustration of gas-diffusion flow-cell. Reproduced with permission.¹⁰⁶ Copyright 2025, Wiley. (e) The schematic illustration of NaCl-co-pyrolysis strategy, which was similar to the synthetic method reported by the ref. (f) The comparison of J_{CO} during CO₂RR. Reproduced with permission.¹⁵⁴ Copyright 2025, Springer Nature.

To investigate the regulatory mechanism of MSI in the electrocatalytic CO₂ reduction reaction, Sun et al.¹⁵³ prepared an Au-CeO₂-DP catalyst with a unique interfacial structure via deposition-precipitation combined with electrochemical pretreatment. The core innovation is that electron spillover from Au³⁺ electrochemical reduction induces CeO₂ support reduction, constructing an active interface of partially encapsulated Au nanoparticles and oxygen-

Electrochemical CO₂RR have emerged as a research hotspot due to their mild conditions, controllable pathways, and high energy efficiency.¹⁴⁵⁻¹⁴⁸ However, chemical inertness of CO₂, slow proton-electron transfer kinetics, and interference from the competitive hydrogen evolution reaction severely limit its efficiency and selectivity.^{149,150} Therefore, designing highly efficient electrocatalysts to reduce overpotentials, suppress HER, and direct the formation of target products is central to scaling CO₂RR applications. In recent years, SACs have emerged as a new research focus due to their maximized atomic utilization and unique electronic properties.^{151,152} MSI are pivotal in regulating CO₂RR performance of SACs. Concurrently, MSI modulates the electronic state and coordination environment of the metal center, optimizing the adsorption strength of intermediates such as CO₂, *COOH, and *CO while lowering reaction energy barriers.

vacancy-rich CeO₂ (Figure 16a). XPS results reveal a positive shift of 0.28 eV in the Au 4f orbital binding energy, confirming the formation of Au^{δ+} species. Ce 3d XPS quantitative analysis reveals an increase in Ce³⁺ content from 15.18% to 26.36%, coupled with enhanced oxygen vacancy characteristic peaks in the O 1s spectrum, confirming oxygen vacancy enrichment on the support surface. MSI-induced interfacial charge rearrangement constructs an efficient electron transport



pathway, enabling the catalyst to achieve a mass current density of 233 mA mg⁻¹ while maintaining high selectivity with a CO Faraday efficiency (FE) >90% (Figure 16b). Chen et al.¹⁰⁶ synthesized Ni-Npyridinic-C and Ni-Npyrrolic-C via rapid Joule heating. Pyridine nitrogen coordination induces a high-spin state that optimizes MSI, promotes CO₂ activation, and stabilizes *COOH, whereas pyrrole nitrogen coordination exhibits weaker effects in the low-spin state. Ni-Npyridinic-C achieved 98.8% CO₂ reduction efficiency in an H-type cell, with >99% selectivity at industrial current densities and across a wide pH range. In zinc-CO₂ batteries, it demonstrated a maximum power density of 1.89 mW cm⁻², showcasing practical application potential (Figure 16c-d). Pan et al.¹⁵⁵ synthesized Co-N₅/HNPCs via coordination engineering, stabilizing Co sites and modulating electronic structure through MSI, which optimize CO₂ adsorption and *COOH formation and achieve CO FE of 99.2% and 99.4% at -0.73 V and -0.79 V (vs RHE.), respectively, with high selectivity and stability across a broad potential range. Wei et al.¹⁵⁴ converted Zn-N₄ sites to Zn-N₃ sites via planar chlorination engineering, optimizing the coordination environment and electronic structure induced by C-Cl bonds to enhance *COOH adsorption and lower the reaction energy barrier. Zn-SA/CNCl-1000 achieve a CO partial current density of 271.7 mA cm⁻² at -0.93 V with 97% FE, stable operation at 200 mA cm⁻² for 50 h (Figure 16e-f).

Conventional carbon supports make it difficult to create highly accessible active sites and CO₂-rich interfacial environments. On top of that, how single-atom metals evolve structurally and catalytically under real operating conditions is still poorly understood. Li et al.¹⁵⁶ designed an interconnected mesoporous carbon nanofiber/carbon nanosheet hybrid network (IPCF@CS) as a catalyst support. During acidic CO₂ electroreduction, the MSI drives the dynamic synergy between Ni single-atom sites and the bicontinuous porous carbon network. Initially, Ni sits stably in the N-doped carbon matrix as a planar Ni-N₄ configuration, with MSI ensuring strong electronic coupling and well-dispersed sites. When a potential is applied, MSI induces an in-plane to out-of-plane distortion of the Ni sites: the planar Ni-N₄ warps into a non-planar configuration with elongated Ni-N bonds, and Ni gets reduced to a lower valence state. This MSI-mediated structural reconstruction adjusts the electron distribution and d-band center of Ni 3d orbitals. As a result, CO₂ activation and *COOH adsorption are both strengthened, while *CO and *H bind is weaker. That not only boosts the intrinsic kinetics of CO₂ reduction but also suppresses hydrogen evolution.

In CO₂ electroreduction, MSI does more than just improve CO₂ activation and the binding of key intermediates like *COOH and *CO. It also lowers the reaction barriers, suppresses hydrogen evolution, and boosts selectivity toward valuable products. Under operando conditions, applying a potential drives MSI to reshape the active sites in situ, giving rise to configurations that better support intrinsic catalytic activity. MSI also helps keep atomically dispersed metal sites stable and makes the catalyst more robust during long-term cycling. Taken together, these roles of MSI offer a solid theoretical foundation for developing technologies that turn CO₂ into high-value chemicals.

3.4. Application of MSI in NRR

Developing catalytic materials with highly efficient NRR functionality has become a significant research focus. SACs exhibit unique catalytic

advantages due to their atomically dispersed active sites and tunable coordination environments.¹⁵⁷ However, these catalysts generally suffer from low metal loading, which directly limits the number of active sites and makes it difficult to meet industrial-scale ammonia yield and FE requirements.^{158,159} Recently, MSI regulation strategies have offered novel approaches to overcoming NRR technical bottlenecks. This strategy optimizes catalytic performance through three dimensions: First, in regulating the reaction microenvironment, the support not only prevents metal atom agglomeration via spatial confinement but also increases the number of active sites; Second, in HER suppression, MSI-induced electronic defect states effectively modulate ΔG_{H*}. Finally, for nitrogen activation, selecting Lewis acid-containing supports reduces the N₂ dissociation energy barrier via σ-π cooperative mechanisms.¹⁶⁰

Li et al.¹⁶¹ successfully synthesized a nitrogen-doped carbon-supported Fe-Mo bimetallic catalyst (FeMoNC) using ZIF-8 as a template (Figure 17a). Its structural core comprises atomically dispersed, adjacent Fe-N₃ and Mo-N₃ sites. The low-spin Fe site adsorbs and activates N₂ via its abundant empty d orbitals, while the adjacent Mo site efficiently promotes H₂O dissociation, continuously supplying protons to nitrogen-containing intermediates at the Fe site, thereby significantly accelerating protonation. Nitrogen-doped carbon support stabilizes the bimetallic atoms via Fe-N and Mo-N coordination bonds, preventing agglomeration, while electronic coupling induces the low-spin state at the Fe site. Additionally, the porous structure of the support significantly enhances mass transfer efficiency between N₂ and the electrolyte. FeMoNC achieves a maximum FE of 37.42% in an H-type electrolyzer with an ammonia yield of 39.35 μg h⁻¹ mg_{cat}⁻¹ (Figure 17b-c). Kong et al.¹⁶² prepared D-FeN/C catalysts via electrospinning combined with pyrolysis. Synergistic effects between Fe-N₄ sites and carbon defects, accelerate species supply and optimize intermediate interactions. Under alkaline electrolyte conditions at -0.4 V, ammonia yield reach 24.8 μg h⁻¹ mg_{cat}⁻¹ with FE of 15.8% (Figure 17d-f).

Xie et al.¹⁶³ hydrothermally synthesized a Mo/VO₂ catalyst. Leveraging strong N₂ adsorption/weak H₂ adsorption properties of VO₂ suppress the HER. MSI between Mo and VO₂ create electron-deficient regions on Mo, further inhibiting the HER while promoting N₂ activation and protonation. Charge density difference analysis reveal Mo transferring 0.3 electrons to N₂, activating the N≡N bond and preparing the substrate for subsequent reactions. This catalyst exhibits distinct NRR activity, achieving an NH₃ yield of 190.1 μg mg_{cat}⁻¹ h⁻¹ and Faradaic efficiency of 32.4% at -0.5 V (Figure 17g-i). Zhang et al.¹⁶⁴ synthesized Ni-BTA (NiN₄ coordination) and Ni-THB (NiO₄ coordination). NiN₄ coordination brought the Ni 3d band center closer to the Fermi level, enhancing charge transfer and N≡N bond activation while lowering the rate-limiting step energy barrier. At -0.2 V vs. RHE, Ni-BTA achieved a FE of 56.3% and ammonia yield of 37.3 μg mg⁻¹ h⁻¹, significantly outperforming Ni-THB (Figure 17j).

Electrocatalytic reduction of nitrite to ammonia has been held back by two main issues: slow water dissociation and weak adsorption of nitrite intermediates. Zhang et al.¹⁶⁵ came up with an in situ electrochemical reconstruction method that turns Ni-doped bismuth oxide (NiBiO_{2-x}) into a Bi/NiBiO_{2-x} composite. Operando characterizations show that NiBiO_{2-x} undergoes structural changes under an applied potential, forming Bi/NiBiO_{2-x} with Ni²⁺ and Bi⁰ working together as dual active sites. The Ni²⁺ sites lower the energy



barrier for water dissociation, while Bi^0 helps adsorb NO_2^- more strongly and promotes the formation and further conversion of the key $^*\text{NO}_2\text{H}$ intermediate. Thanks to this synergy, the in-situ-formed $\text{Bi}/\text{NiBiO}_{2-x}$ catalyst delivers efficient conversion of nitrite to ammonia.

In the electrochemical NRR, MSI play an indispensable role in enhancing the practical performance of ammonia synthesis. MSI optimizes the electronic state and coordination environment of active sites through electron transfer between the support and

metal, enhancing N_2 adsorption and $\text{N}=\text{N}$ bond activation. It also modulates the adsorption energy barrier of hydrogen intermediates, effectively suppressing the competing HER and significantly improving the FE of ammonia synthesis. In summary, MSI simultaneously elevates the catalytic activity, selectivity, and long-term stability of the NRR. This provides critical support for developing green ammonia synthesis technologies under ambient conditions.

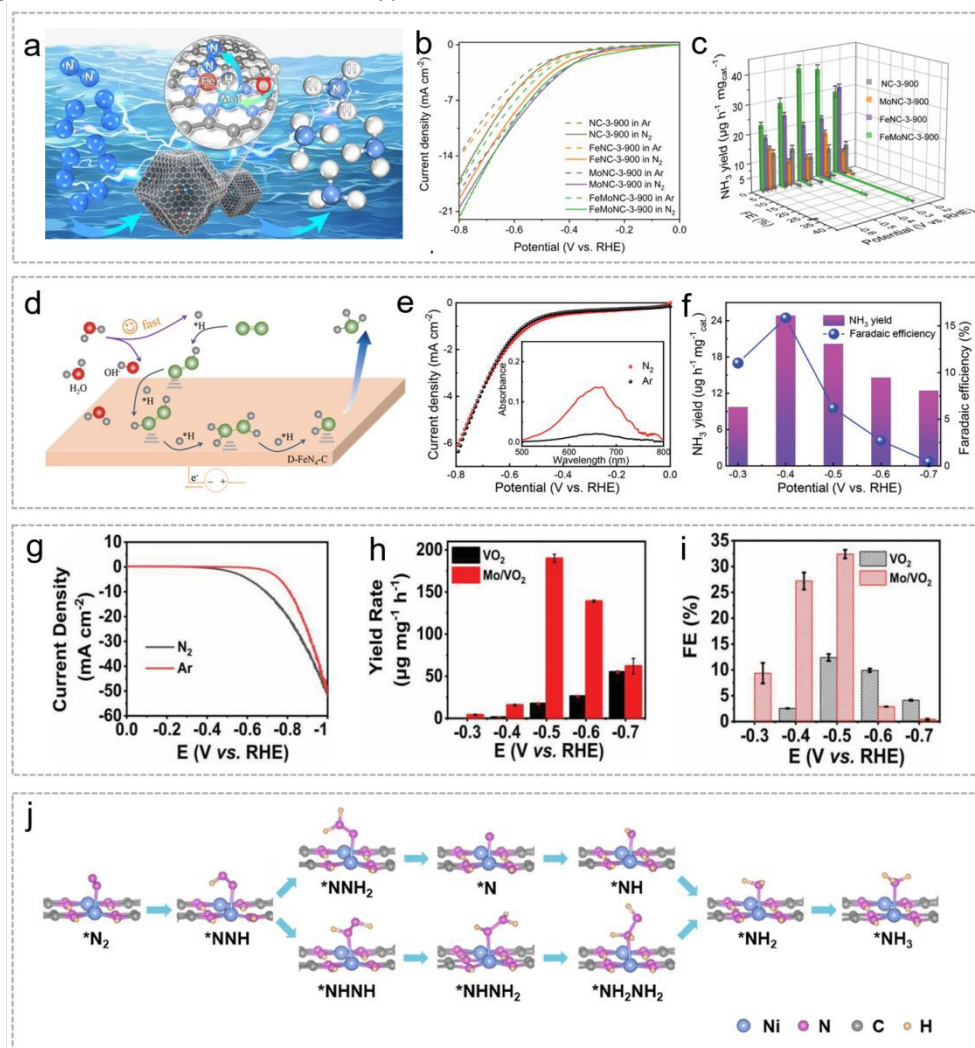


Figure 17. Application of MSI in the NRR. (a) Schematic Diagram of FeMoNC Catalysis. (b) Polarization curves of various samples in Ar/N_2 -saturated 0.1 M KOH solution. (c) NH_3 yield rate and FE values of various samples at given potentials. Reproduced with permission.¹⁶¹ Copyright 2025, American Chemical Society. (d) A proposed reaction mechanism for accelerated proton-feeding NRR kinetics. (e) Polarization curves of D-FeN/C conducted in N_2 -saturated (red line) and Ar -saturated (black line) 0.1 m KOH solution; inset: corresponding UV-vis absorption spectra of the electrolytes stained with indophenol indicator after NRR electrolysis. (f) NH_3 yields (purple) and FE values (blue) of D-FeN/C at different applied potentials. Reproduced with permission.¹⁶² Copyright 2022, Wiley. (g) LSV curves of Mo/VO_2 in 0.05 M H_2SO_4 saturated with Ar and N_2 at a scan rate of 10 mV s^{-1} . (h) NH_3 yield and (i) FE of Mo/VO_2 and VO_2 at different potentials. Reproduced with permission.¹⁶³ Copyright 2023, Wiley. (j) Simplified structures of reaction intermediates on the Ni-BTA model along the distal and alternating pathways of NRR catalysis. Reproduced with permission.¹⁶⁴ Copyright 2025, Wiley.

3.5. Application of MSI in the Oxidation of Organic Small Molecules

“Alternative anode reactions”, replacing OER with the oxidation of organic small molecules offer a solution^{166,167}: Small molecules like 5-Hydroxymethylfurfural (HMF) and glycerol have oxidation potentials

lower than OER, enabling reduced cell voltage and enhanced hydrogen production efficiency.¹⁶⁸ Simultaneously, high-value-added products are produced, achieving synergistic “hydrogen production-value enhancement.” In fuel cells, liquid organic hydrogen carriers (LOHCs) like methanol and formic acid serve as



vital hydrogen supplements due to their convenient storage/transport and high energy density.^{169,170}

For example, HMF is a key biomass platform compound that can be converted into various high-value chemicals. Among these, 2,5-furan dicarboxylic acid (FDCA) serves as a crucial monomer for synthesizing bio-based polyesters such as polyethylene furfural, offering a promising alternative to petroleum-based terephthalic acid. Xu et al.¹⁷¹ synthesized Ru_{0.3}/NiFe LDH SACs. Leveraging MSI to form Ru^{δ+} and induce Ni/Fe electron rearrangement, they enhanced HMF hydroxyl adsorption and NiOOH phase formation while lowering the rate-limiting step energy barrier. The catalyst achieves 99.2% HMF conversion, 98.7% FDCA selectivity, and excellent

stability (Figure 18a-b). Formaldehyde, a low-cost chemical feedstock, exhibits an extremely low theoretical potential for oxidation (FOR), while its product formic acid holds significant economic value. Qiu and Gao¹⁷² achieved highly efficient FOR using Pt_{SA}-Cu NWs SACs. Due to the high electronegativity of Pt regulating the electronic structure of Cu, Pt-Cu interactions reduce the coupling free energy of H* (Figure 18c). The Pt_{SA}-Cu NWs catalyst exhibits outstanding intrinsic activity and a large electrochemical active surface area, effectively promoting the FOR. A current density of 100 mA cm⁻² is achieved at a voltage of 0.09 V. The FOR-HER bipolar system attained an industrial-grade current density of 0.12 V, with H₂ FE stably maintained for 30 h (Figure 18d).

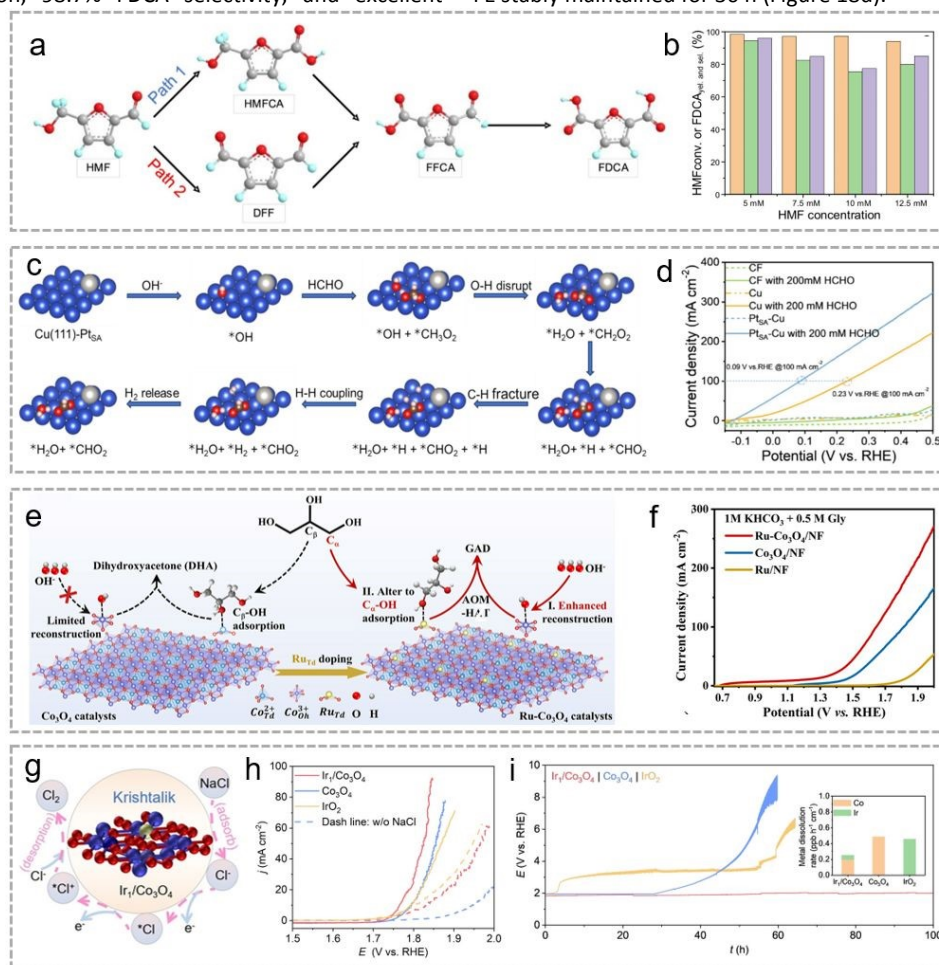


Figure 18. Application of MSI in the oxidation of organic small molecules. (a) Schematic illustration of the two possible HMF oxidation pathways to FDCA. (b) Diagram of HMF conversion, FDCA selectivity and FDCA yield versus substrate concentration during the electrochemical oxidation of HMF on Ru_{0.3}/NiFe. Reproduced with permission.¹⁷¹ Copyright 2023, Elsevier. (c) Optimization of crystal structures of different intermediates on Cu (1 1 1) and Cu (1 1 1)-Pt_{SA}. (d) LSV of CF, Cu, and Pt_{SA}-Cu NWs in 1.0 M KOH and 200 mM HCHO. Reproduced with permission.¹⁷² Copyright 2025, Elsevier. (e) Schematic diagram of Ru atoms regulating the adsorption configuration of C α -OH and enhancing OH⁻ adsorption enrichment. (f) LSV curves of the potential at different current densities. Reproduced with permission.¹⁷³ Copyright 2025, Wiley. (g) Schematic illustration of the COR pathway in Ir₁/Co₃O₄. (h) LSV curves of the comprehensive electrochemical performance of Ir₁/Co₃O₄, Co₃O₄, and IrO₂. (i) Chronopotentiometry curves of Ir₁/Co₃O₄, Co₃O₄, and IrO₂ at 15 mA cm⁻². Reproduced with permission.¹⁷⁴ Copyright 2024, Wiley.

The electrocatalytic oxidation of glycerol (GOR) to produce high-value glycerol aldehyde (GAD) suffers from numerous alkaline side reactions and slow neutral kinetics. Luo et al.¹⁷³ developed a Ru-Co₃O₄/NF catalyst that activates Co₃O₄ lattice restructuring through Ru doping, thereby regulating the adsorption configuration of glycerol primary alcohol (Figure 18e). This approach simultaneously

enhances GOR activity and selectivity in near-neutral media. It achieved 10 mA cm⁻² at 1.16 V (vs. RHE) in 1 M KHCO₃, with wide potential window GAD selectivity \approx 60% and total C₃ product selectivity \approx 90%, demonstrating excellent stability (Figure 18f). Cai et al.¹⁷⁴ successfully constructed an Ir single-atom substituted Co₃O₄ catalyst (Ir₁/Co₃O₄) by precisely replacing octahedral Co sites in Co₃O₄



with Ir atoms, forming an atomically precise asymmetric Ir-O-Co coordination structure. Within this structure, electron transfer occurs between the Ir site and the Co_3O_4 via Ir-O-Co bonds. Mechanistically, the Ir site strongly adsorbs and activates Cl $^-$. By moderately binding the *Cl intermediate, it significantly lowers the energy barrier of the rate-determining step-chlorine evolution reaction (COR)-and promotes electron transfer, thereby enhancing overall reaction kinetics (Figure 18g). In constant-current stability testing, $\text{Ir}_1/\text{Co}_3\text{O}_4$ demonstrates outstanding catalytic performance, maintaining essentially stable activity for up to 100 h (Figure 18h-i).

The electrochemical urea oxidation reaction (UOR) offers a less energy-intensive route than the oxygen evolution reaction for producing hydrogen through water electrolysis. Gong et al.¹⁷⁵ prepared a Ni-based catalyst with an amorphous/crystalline heterojunction, labeled A/C-Ni@G. Due to its unsaturated coordination and efficient interfacial charge transfer, this structure rapidly reconstructs during electrolysis into vacancy-rich NiOOH, which acts as the real active species. This unique active form helps break the C-N bonds in urea and lowers the energy barrier of the rate-determining step. As a result, the catalyst delivers excellent UOR performance.

In the electrooxidation of small organic molecules, MSI affect the catalytic performance in several ways. MSI can tune the electronic structure or induce coordination changes at metal active sites, which helps activate C-H, O-H, and C-N bonds in the organic molecules. It also steers how intermediates are adsorbed and converted. On top of that, MSI holds the metal species firmly on the support through coordination bonding, which keeps metal particles from aggregating or leaching out. That in turn makes the catalyst more resistant to poisoning and more stable over long-term cycling.

4. Conclusion

This review systematically summarizes the regulation of MSI by support types, crystal phases, crystal facets, and atomic doping. The regulatory mechanisms of MSI based on different support materials and their microstructural characteristics are systematically revealed. Among them, oxide supports leverage unique surface structures and electronic properties to regulate metal electron distribution and band structure; Sulfide supports optimize MSI configurations through geometric anchoring and electronic interactions; Nitride supports stabilize single-atom active sites and adjust their electron density and coordination environment via electronic coupling effects of metal-nitrogen bonds; Carbon supports provide favorable electron transport and mass transfer environments for active metals through superior conductivity and specific chemical structures; Phosphide supports enhance MSI by inducing metal spin state transitions via electronic structure modulation; LDH utilizes its layered structure to precisely regulate the electronic structure of active sites through coordination bonding and electron transfer. At the microstructural level: Crystal phases influence strain effects and interfacial electron transfer through lattice matching, regulating MSI intensity and mechanisms at atomic and electronic scales; Crystal facets modulate MSI by altering coordination environments and geometric configurations of active sites via surface exposure differences; Vacancy defects systematically adjust MSI mechanisms to precisely control the structure, electronic states, and catalytic

behavior of metal active components; Atomic doping significantly impacts MSI and enhances catalytic performance through multiple mechanisms. Consequently, the strong MSI endows this catalyst with exceptional performance in key electrochemical reactions, including HER, OER, ORR, HOR, CO_2RR , NRR, and organic molecule oxidation. Although the unique catalytic mechanism of MSI plays a central role in catalytic applications, there are still many difficulties in its current research. Looking ahead, addressing current research gaps, MSI studies should focus on:

(1) Uncovering dynamic mechanisms through in situ characterization techniques: Current understanding is largely based on ex-situ or post-mortem characterization, which fails to capture the transient electronic and structural states of the metal-support interface during catalysis. Advanced in situ/operando techniques-such as ambient-pressure X-ray photoelectron spectroscopy (AP-XPS), electrochemical scanning transmission electron microscopy (EC-STEM), and time-resolved X-ray absorption spectroscopy (XAS)-are critical to probe the real-time dynamics of charge transfer, adsorbate-induced restructuring, and the stability of single-atom sites under applied potential and reactive environments. This knowledge is fundamental for deciphering true active centers and deactivation pathways.

(2) Pioneering the rational design of next-generation support matrices: Moving beyond conventional oxides and carbons, the synthesis of supports with programmable defects, strain fields, and atomic-scale architectures is essential. This includes the development of conductive metal-organic frameworks (MOFs), covalent organic frameworks (COFs), high-entropy compounds, and tailored 2D materials. The goal is to precisely engineer supports that not only anchor metals atomically but also actively participate in the reaction through optimized ligand fields, concerted proton-electron transfer, or spillover effects, thereby breaking traditional scaling relationships.

(3) Establish descriptors for quantifying MSI intensity: The direct quantitative characterization of the strength of MSI remains a key challenge in the field of heterogeneous catalysis. At its core, MSI is essentially the result of the coupling of multiple physicochemical effects, including electron transfer, lattice geometric matching, interfacial chemical bonding, and dynamic structural reorganization. Moreover, its characteristics are highly dependent on the reaction microenvironment, the composition and morphology of the supported metal and the support, as well as the interfacial microstructure, making it difficult to achieve precise and universal quantification using a single physical or chemical parameter. Regarding quantitative research on MSI, a promising direction is the development of a multi-parameter, synergistically coupled quantitative characterization system and quantitative analysis of the evolution of MSI intensity under reaction conditions. Concurrently, leveraging big data and machine learning technologies, quantitative MSI data from different catalytic systems should be integrated to establish standardized, universal MSI intensity evaluation models.

(4) Machine learning and high-throughput computation for predicting and screening novel MSI interfaces: Traditional theoretical calculations often rely on specific model systems and perform point by point analyses. Key parameters like binding energy, charge transfer, and diffusion barriers are calculated to describe MSI strength. This approach is not only computationally inefficient but



also struggles to systematically cover combinations of multiple variables such as metal type, support facet, defect configuration, and coordination environment. In contrast, high-throughput computation can programmatically adjust interface structural parameters to efficiently generate large-scale, standardized MSI-related datasets, providing a solid foundation for data-driven research. On this basis, machine learning algorithms can extract hidden structure-activity relationships from massive datasets, enabling rapid prediction of MSI strength, structural stability, and catalytic activity trends for unknown interfaces. Overall, coupling machine learning with high-throughput computation for MSI research not only speeds up the development of high-performance interfaces and promotes rational catalyst design, but also offers new approaches and theoretical support for linking quantitative MSI descriptors to actual catalytic performance.

(5) Precise structure-function relationship between MSI and catalyst-specific structures: By integrating in-situ characterization techniques with multiscale theoretical calculations, the influence mechanisms of support microstructural features are need to systematically quantify. The goal is to elucidate how MSI directionally modulates the electronic structure and coordination environment of active sites, thereby establishing a quantitative correlation model linking “support microstructure-MSI characteristics-catalytic performance.” Based on this theoretical framework, precise design of support structures and optimization of MSI enable rational control over metal active sites, leading to the development of highly efficient and stable catalytic systems that transcend the limitations of traditional linear energy relationships.

This review establishes MSI as a fundamental design paradigm for atomically dispersed electrocatalysts, systematically elucidating how support types, crystal phases, crystal facets, vacancy defects, and atomic doping modulate the electronic structure and coordination geometry of active sites. Furthermore, with MSI as the core regulatory strategy, this approach systematically enhances catalyst activity, selectivity, and durability. It drives performance breakthroughs in electrocatalytic reactions for critical fields like energy conversion, providing robust theoretical support and design guidance for developing highly efficient, low-cost catalysts for industrial applications.

Author contributions

Chaolong Wang: Writing – review & editing, Writing – original draft, Validation, Supervision, Methodology, Investigation, Data curation. Shasha Gao: Writing – original draft, Software, Methodology, Investigation, Data curation. Xiaojing Bu: Investigation, Data curation. Jiacong Lei: Investigation, Writing – original draft. Zhen Zhou: Resources, Project administration, Funding acquisition. Gonglei Shao: Conceptualization, Writing – review & editing, Writing – original draft, Resources, Funding acquisition.

Conflicts of interest

The authors declare no conflict of interest.

Data availability

All data cited in this work are sourced from the original peer-reviewed literature, with full references provided throughout the manuscript and in the reference list. No new experimental or computational data were generated in this study.

Acknowledgements

This work was supported by Henan Province's Central Plains Talent Program (Cultivation Series) - Young Top Talents of Central Plains, the National Natural Science Foundation of China (22205209), and Joint Fund for Provincial Scientific Research and Development Plan of Henan Province (242301420039).

Notes and references

- G. Qing, R. Ghazfar, S. T. Jackowski, F. Habibzadeh, M. M. Ashtiani, C.-P. Chen, M. R. Smith, III and T. W. Hamann, *Chem. Rev.*, 2020, **120**, 5437-5516.
- W.-J. Ong, L.-L. Tan, Y. H. Ng, S.-T. Yong and S.-P. Chai, *Chem. Rev.*, 2016, **116**, 7159-7329.
- J. G. Chen, R. M. Crooks, L. C. Seefeldt, K. L. Bren, R. M. Bullock, M. Y. Darensbourg, P. L. Holland, B. Hoffman, M. J. Janik, A. K. Jones, M. G. Kanatzidis, P. King, K. M. Lancaster, S. V. Lymar, P. Pfromm, W. F. Schneider and R. R. Schrock, *Science*, 2018, **360**, eaar6611.
- Y. Nie, L. Li and Z. Wei, *Chem. Soc. Rev.*, 2015, **44**, 2168-2201.
- M. K. Debe, *Nature*, 2012, **486**, 43-51.
- X. Liang, N. Fu, S. Yao, Z. Li and Y. Li, *J. Am. Chem. Soc.*, 2022, **144**, 18155-18174.
- Y. Q. Zhang, J. Yang, R. Y. Ge, J. J. Zhang, J. M. Cairney, Y. Li, M. Y. Zhu, S. Li and W. X. Li, *Coord. Chem. Rev.*, 2022, **461**, 214493.
- Z. Li, S. Ji, Y. Liu, X. Cao, S. Tian, Y. Chen, Z. Niu and Y. Li, *Chem. Rev.*, 2020, **120**, 623-682.
- S. Ji, Y. Chen, X. Wang, Z. Zhang, D. Wang and Y. Li, *Chem. Rev.*, 2020, **120**, 11900-11955.
- R. Qin, K. Liu, Q. Wu and N. Zheng, *Chem. Rev.*, 2020, **120**, 11810-11899.
- S. K. Kaiser, Z. Chen, D. F. Akl, S. Mitchell and J. Perez-Ramirez, *Chem. Rev.*, 2020, **120**, 11703-11809.
- S. Tauster, S. Fung and R. L. Garten, *J. Am. Chem. Soc.*, 1978, **100**, 170-175.
- S. Tauster and S. Fung, *J. Catal.*, 1978, **55**, 29-35.
- B. H. Chen and J. White, *J. Phys. Chem.*, 1982, **86**, 3534-3541.
- D. E. Resasco and G. Haller, *J. Catal.*, 1983, **82**, 279-288.
- E. J. Braunschweig, A. D. Logan, A. K. Datye and D. J. Smith, *J. Catal.*, 1989, **118**, 227-237.
- Y. Guo, J. Liang, Y. Huang, J. Yang, Q. Zhang, A. Wang, B. Qiao, J. Li and T. Zhang, *Acc. Chem. Res.*, 2025, **58**, 2440-2453.
- Y. Wan, R. Li, J. Su, W. Yi, Y. Li, H. Chu, Z. Shen, S. Gao, X. Hai, R. Zhong and R. Zou, *Adv. Mater.*, 2025, **37**, 2504518.
- L. Gloag, S. V. Somerville, J. J. Gooding and R. D. Tilley, *Nat. Rev. Mater.*, 2024, **9**, 173-189.
- V. Muravev, A. Parastayev, Y. van den Bosch, B. Ligt, N. Claes, S. Bals, N. Kosinov and E. J. M. Hensen, *Science*, 2023, **380**, 1174-1179.
- C. Jiang, B. Yan, B. R. Goldsmith and S. Linic, *Nat. Catal.*, 2025, **8**, 1038-1050.
- R. Lang, X. Du, Y. Huang, X. Jiang, Q. Zhang, Y. Guo, K. Liu, B. Qiao, A. Wang and T. Zhang, *Chem. Rev.*, 2020, **120**, 11986-12043.
- C. Cai, M. Wang, S. Han, Q. Wang, Q. Zhang, Y. Zhu, X. Yang, D. Wu, X. Zu, G. E. Sterbinsky, Z. Feng and M. Gu, *ACS Catal.*, 2021, **11**, 123-130.
- J. Wang, M. Zhou, R. Fu, J. Ge, W. Yang, X. Hong, C. Sun, X. Liao,

View Article Online

DOI: 10.1039/D6SC02712A



- Y. Zhao and Z. Wang, *Adv. Funct. Mater.*, 2024, **34**, 2315326.
25. S. Chen, X. Liu, J. Xiong, L. Mi, X.-Z. Song and Y. Li, *J. Mater. Chem. A*, 2022, **10**, 6927-6949.
26. X. Li, W. Liu, M. Zhang, Y. Zhong, Z. Weng, Y. Mi, Y. Zhou, M. Li, J. Cha, Z. Tang, H. Jiang, X. Li and H. Wang, *Nano Lett.*, 2017, **17**, 2057-2063.
27. X. Wang, W. Ma, Z. Xu, H. Wang, W. Fan, X. Zong and C. Li, *Nano Energy*, 2018, **48**, 500-509.
28. Y. Zhong, X. Xia, F. Shi, J. Zhan, J. Tu and H. J. Fan, *Adv. Sci.*, 2016, **3**, 1500286.
29. Y. Bu, Z. Chen and W. Li, *Appl. Catal. B: Environ.*, 2014, **144**, 622-630.
30. Y. Liu, Q. Wang, J. Zhang, J. Ding, Y. Cheng, T. Wang, J. Li, F. Hu, H. B. Yang and B. Liu, *Adv. Energy Mater.*, 2022, **12**, 2200928.
31. W. Song, C. Xiao, J. Ding, Z. Huang, X. Yang, T. Zhang, D. Mitlin and W. Hu, *Adv. Mater.*, 2024, **36**, 2301477.
32. K. Fan, Z. Li, Y. Song, W. Xie, M. Shao and M. Wei, *Adv. Funct. Mater.*, 2021, **31**, 2008064.
33. P. Zhai, M. Xia, Y. Wu, G. Zhang, J. Gao, B. Zhang, S. Cao, Y. Zhang, Z. Li and Z. Fan, *Nat. Commun.*, 2021, **12**, 4587.
34. C. Han, S. Zhang, H. Zhang, Y. Dong, P. Yao, Y. Du, P. Song, X. Gong and W. Xu, *eScience*, 2024, **4**, 100269.
35. J. Shan, C. Ye, Y. Jiang, M. Jaroniec, Y. Zheng and S.-Z. Qiao, *Sci. Adv.*, 2022, **8**, eabo0762.
36. R. Lang, X. Du, Y. Huang, X. Jiang, Q. Zhang, Y. Guo, K. Liu, B. Qiao, A. Wang and T. Zhang, *Chem. Rev.*, 2020, **120**, 11986-12043.
37. H. Wang, Z. Gao, B. Sun, S. Mu, F. Dang, X. Guo, D. Ma and C. Shi, *Chem Catal.*, 2023, **3**, 100768.
38. Z. Yang, F. Lai, Q. Mao, C. Liu, S. Peng, X. Liu and T. Zhang, *Adv. Mater.*, 2025, **37**, 2412950.
39. M. Sun, W. Wan, X. Zhao, C. Shao, N. Liu, M. Fan and J. Wang, *Adv. Funct. Mater.*, 2025, **35**, 2500553.
40. J. Wei, H. Tang, Y. Liu, G. Liu, L. Sheng, M. Fan, Y. Ma, Z. Zhang and J. Zeng, *Angew. Chem.-Int. Edit.*, 2024, **136**, e202410520.
41. Z.-H. Xue, J. Mahmood, Y. Shang, G. Li, S.-J. Kim, Y. Han and C. T. Yavuz, *J. Am. Chem. Soc.*, 2025, **147**, 17839-17848.
42. Y. Wan, R. Li, J. Su, W. Yi, Y. Li, H. Chu, Z. Shen, S. Gao, X. Hai and R. Zhong, *Adv. Mater.*, 2025, **37**, 2504518.
43. J. A. Rodriguez and J. Hrbek, *Acc. Chem. Res.*, 1999, **32**, 719-728.
44. J. Barbier, E. Lamy-Pitara, P. Marecot, J. Boitiaux, J. Cosyns and F. Verna, *Adv. Cat.*, 1990, **37**, 279-138.
45. S. Wilke and M. Scheffler, *Phys. Rev. Lett.*, 1996, **76**, 3380.
46. J. Lv, Q. Yang, T. Liang, X. Sun, W. Rong, Q. Dai, Y. Gao, L. Wang, X. Xu and Y. Liu, *J. Am. Chem. Soc.*, 2025, **147**, 27708-27719.
47. H. Liu, Q. Liu, Y. Shao, R. Wang, M. Cheng, J. Hu, T. Wei, B. Liu, H. Jiang, L. Qi, M. Chen, W. Lu, W. Li and X. Li, *Adv. Funct. Mater.*, 2025, **35**, 2425826.
48. P. Trogadas, T. F. Fuller and P. Strasser, *Carbon*, 2014, **75**, 5-42.
49. L. Zhang, J. Xiao, H. Wang and M. Shao, *ACS Catal.*, 2017, **7**, 7855-7865.
50. H. Liu, J. Zhao and X. Li, *Electrochem. Energy Rev.*, 2022, **5**, 13.
51. D. Liu, X. Li, S. Chen, H. Yan, C. Wang, C. Wu, Y. A. Haleem, S. Duan, J. Lu and B. Ge, *Nat. Energy*, 2019, **4**, 512-518.
52. R. T. Sanderson, *J. Am. Chem. Soc.*, 1983, **105**, 2259-2261.
53. K. Dehnicke and J. Strähle, *Angew. Chem.-Int. Edit.*, 1981, **20**, 413-426.
54. G. Vilé, D. Albani, M. Nachttegaal, Z. Chen, D. Dontsova, M. Antonietti, N. López and J. Pérez-Ramírez, *Angew. Chem.-Int. Edit.*, 2015, **54**, 11265-11269.
55. M. Sun, Y. Jiang, H. Song, J. Zhang, G. Yin, Y. Cui, C. Zhang, G. Yin and S. Lu, *Adv. Funct. Mater.*, 2025, **35**, 2504982.
56. X. Hu, X. Chen, X. Li and C. Xu, *Adv. Funct. Mater.*, 2024, **34**, 2316699.
57. R. Wang, J. Guo, J. Li, Q. Wang, Z. Lv, C. Gong, C. Pan and T. Ling, *Angew. Chem.-Int. Edit.*, 2025, **137**, e202510671.
58. G. Shao, C. Jing, Z. Ma, Y. Li, W. Dang, D. Guo, M. Wu, S. Liu, X. Zhang, K. He, Y. Yuan, J. Luo, S. Dai, J. Xu and Z. Zhou, *Nat. Commun.*, 2024, **15**, 385.
59. Z. Han, S. Son, K. Kim, S. Gao and G. Shao, *Chem. Mater.*, 2024, **36**, 1831-1840. DOI: 10.1039/D6SC02712A
60. M. Chen, Y. Guan, Z. Miao, S. Zhang, C. Wu, Y. Zhou, H. Luo, D. Wu, R. Li, J. Luo and X. Tian, *ACS Central Sci.*, 2025, **11**, 1862-1869.
61. M. Haeser, *J. Am. Chem. Soc.*, 1994, **116**, 6925-6926.
62. D. E. C. Corbridge, *Phosphorus: an outline of its chemistry, biochemistry and technology*, Elsevier, 2025.
63. M. Wu, R. Zhang, C. Li, X. Sun, G. Chen, L. Guo, K. Zheng and X. Sun, *Mat. Chem. Front.*, 2023, **7**, 4918-4927.
64. S. Wang, S. Li, Y. Yu, T. Zhang, J. Qu and Q. Sun, *Small Methods*, 2024, **8**, 2400376.
65. Z. Luo, J. Xie, J. Cheng, F. Wei, S. Lyu, J. Zhu, X. Shi, X. Yang, B. Wu and Z. J. Xu, *Adv. Mater.*, 2025, **37**, 2504585.
66. Q. He, D. Tian, H. Jiang, D. Cao, S. Wei, D. Liu, P. Song, Y. Lin and L. Song, *Adv. Mater.*, 2020, **32**, 1906972.
67. L. Zhou, T. Wan, Y. Zhong, W. Liu, L. Yu, T. Li, K. Sun, G. I. Waterhouse, H. Xu and Y. Kuang, *Small*, 2024, **20**, 2406076.
68. J. Fan, J. Xia, H. Wang, H. Li, Y. Tao, G. Wang, W. Hao, Q. Bi, G. Li and X. Shen, *Adv. Energy Mater.*, 2025, **15**, 2501995.
69. Z.-z. Yang, J.-j. Wei, G.-m. Zeng, H.-q. Zhang, X.-f. Tan, C. Ma, X.-c. Li, Z.-h. Li and C. Zhang, *Coordin. Chem. Rev.*, 2019, **386**, 154-182.
70. Q. Wang and D. O'Hare, *Chem. Rev.*, 2012, **112**, 4124-4155.
71. A. Karmakar, K. Karthick, S. S. Sankar, S. Kumaravel, R. Madhu and S. Kundu, *J. Mater. Chem. A*, 2021, **9**, 1314-1352.
72. D. P. Sahoo, K. K. Das, S. Mansingh, S. Sultana and K. Parida, *Coordin. Chem. Rev.*, 2022, **469**, 214666.
73. H. Yi, S. Liu, C. Lai, G. Zeng, M. Li, X. Liu, B. Li, X. Huo, L. Qin and L. Li, *Adv. Energy Mater.*, 2021, **11**, 2002863.
74. J. Zhang, L. Yu, Y. Chen, X. F. Lu, S. Gao and X. W. Lou, *Adv. Mater.*, 2020, **32**, 1906432.
75. Z. Gu, J. J. Atherton and Z. P. Xu, *Chem. Commun.*, 2015, **51**, 3024-3036.
76. F. Wang, P. Zou, Y. Zhang, W. Pan, Y. Li, L. Liang, C. Chen, H. Liu and S. Zheng, *Nat. Commun.*, 2023, **14**, 6019.
77. J. Zhang, J. Liu, L. Xi, Y. Yu, N. Chen, S. Sun, W. Wang, K. M. Lange and B. Zhang, *J. Am. Chem. Soc.*, 2018, **140**, 3876-3879.
78. W. Chen, B. Wu, Y. Wang, W. Zhou, Y. Li, T. Liu, C. Xie, L. Xu, S. Du and M. Song, *Energy Environ. Sci.*, 2021, **14**, 6428-6440.
79. S. Shen, Q. Li, H. Zhang, D. Yang, J. Gong, L. Gu, T. Gao and W. Zhong, *Adv. Mater.*, 2025, **37**, 2500595.
80. M. Israr, S. Ali, J. Zhang, Y. Zeng, M. Humayun, H. Yu, X. Chen, C. Chen and Y. Li, *Small*, 2025, **21**, 2500828.
81. J. Wei, H. Tang, L. Sheng, R. Wang, M. Fan, J. Wan, Y. Wu, Z. Zhang, S. Zhou and J. Zeng, *Nat. Commun.*, 2024, **15**, 559.
82. H. Xu, L. Lu, Z. Yu, X. Lu, Y. Duan, C. Si and X. Li, *Appl. Catal. B-Environ. Energy*, 2025, **375**, 125439.
83. J.-W. Zhao, H.-Y. Wang, L. Feng, J.-Z. Zhu, J.-X. Liu and W.-X. Li, *Chem. Rev.*, 2024, **124**, 164-209.
84. X. Zhang, Y. Dong, Q. Lv, C. Jiang, Y. Wang, J. Dou, Q. Guo, B. Dong and Q. Tang, *Appl. Catal. B: Environ.*, 2024, **342**, 123440.
85. X. Xie, Y. Fan, W. Tian, M. Zhang, J. Cai, X. Zhang, J. Ding, Y. Liu and S. Lu, *J. Energy Chem.*, 2023, **83**, 150-157.
86. J. Xu, F. Yang, X. Guo, S. Wang and L. Feng, *J. Energy Chem.*, 2025, **105**, 170-177.
87. S. She, C. Chen, K. Fan, G. Chen, Y. Zhu, D. Guan, Y.-C. Huang, H.-C. Chen, Z. Lin and H. F. Wong, *J. Am. Chem. Soc.*, 2025, **147**, 24392-24402.
88. Z. Shi, X. Zhang, X. Lin, G. Liu, C. Ling, S. Xi, B. Chen, Y. Ge, C. Tan, Z. Lai, Z. Huang, X. Ruan, L. Zhai, L. Li, Z. Li, X. Wang, G.-H. Nam, J. Liu, Q. He, Z. Guan, J. Wang, C.-S. Lee, A. R. J. Kucernak and H. Zhang, *Nature*, 2023, **621**, 300-305.
89. S. Qian, T. Jiang, J. Wang, W. Yuan, D. Jia, N. Cheng, H. Xue, Z. Xu, R. Gautier and J. Tian, *ACS Catal.*, 2024, **14**, 18690-18700.
90. K. Endo, M. Saruyama and T. Teranishi, *Nat. Commun.*, 2023, **14**, 4241.
91. X. Yu, Y. Xie, X. Dong, D. Wang, T. Sun, Q. Sun, S. Cao, F. Meng, R. Zou, C. Zhang, Q. Xu and C.-C. Hou, *Adv. Funct. Mater.*, 2025, **35**,



- 2424401.
92. Y. Zheng, Z. Xing, S. Xiao, D. Ye, Y. Kong, S. Zhang, T. Ma, C. Cheng, S. Li and C. Zhao, *Adv. Mater.*, 2025, **37**, 2508994.
93. J. Liu, Y. Wen, W. Yan, Z. Huang, X. Liu, X. Huang, C. Zhan, Y. Zhang, W.-H. Huang, C.-W. Pao, Z. Hu, D. Su, S. Xie, Y. Wang, J. Han, H. Xiong, X. Huang and N. Chen, *Energy Environ. Sci.*, 2025, **18**, 4396-4404.
94. C. Liu, S. Kwon, P. Godbold, G. Johnson, S. Hwang, C. Sun, H. Zhou, W. A. Goddard, III and S. Zhang, *J. Am. Chem. Soc.*, 2025, **147**, 19391-19399.
95. G. Shao, H. Xiang, M. Huang, Y. Zong, J. Luo, Y. Feng, X.-X. Xue, J. Xu, S. Liu and Z. Zhou, *Sci. China Mater.*, 2022, **65**, 1833-1841.
96. J. Zhang, D. Yang, Z. Yang and L. Wang, *Appl. Catal. B-Environ. Energy*, 2025, **364**, 124845.
97. M. Xi, H. Zhang, L. Yang, Y. Long, Y. Zhao, A. Chen, Q. Xiao, T. Liu, X. Xiao and G. Hu, *Adv. Sci.*, 2025, **12**, 2409855.
98. C. Jia, S. Li, Y. Zhao, R. K. Hocking, W. Ren, X. Chen, Z. Su, W. Yang, Y. Wang and S. Zheng, *Adv. Funct. Mater.*, 2021, **31**, 2107072.
99. Z.-J. Duan, H. Xia, H.-Z. Li, G.-L. Shao, Y.-Z. Ren, X. Tang, Q.-N. Liu, J.-H. Hong, S. Dai and Y.-C. Lin, *Rare Metals*, 2025, **44**, 3130-3140.
100. G. Shao, J. Xu, S. Gao, Z. Zhang, S. Liu, X. Zhang and Z. Zhou, *Carbon Energy*, 2024, **6**, e417.
101. Y. Peng, A. A. Nyaaba, J.-Y. Liu, L. Yang, Y.-J. Liu, H.-B. Zhou, Z.-Y. Ji, B. Zhou, Y. Zhong and G.-X. Zhu, *Rare Metals*, 2025, **44**, 6246-6257.
102. C.-X. Xu, J.-J. Zhang, H.-R. Dou, Y.-Z. Li, D.-M. Li, Y.-J. Zhang, B. Liu, P. Inbaraj and P.-P. Huo, *Rare Metals*, 2025, **44**, 3156-3169.
103. G. Shao, X. X. Xue, B. Wu, Y. C. Lin, M. Ouzounian, T. S. Hu, Y. Xu, X. Liu, S. Li and K. Suenaga, *Adv. Funct. Mater.*, 2020, **30**, 1906069.
104. H.-H. Huang, W. Li, C.-C. Hu, X.-Q. Sun, L.-G. Lu and X.-F. Fan, *Rare Metals*, 2024, **43**, 5126-5140.
105. Y.-H. Cui, W.-C. Ouyang, A.-J. Gao, C.-Y. Yu and L.-P. Zhang, *Rare Metals*, 2024, **43**, 5117-5125.
106. Z. Chen, J. Liu, J. Li, Y. Zhang, J. Yang, J. Li, Z. Wang, Z. Liu and S.-Q. Zang, *Angew. Chem.-Int. Edit.*, 2025, **64**, e202506845.
107. D. Guo, X.-X. Xue, M. Jiao, J. Liu, T. Wu, X. Ma, D. Lu, R. Zhang, S. Zhang and G. Shao, *Chem. Sci.*, 2024, **15**, 16281-16290.
108. L. Zhang, Y. Lei, X. Wang, E. Lv, J. Li, N. Zhang, D. Wang, Y. Zhao, H. Shang and B. Zhang, *Adv. Funct. Mater.*, 2026, **36**, e11730.
109. B. You and Y. Sun, *Acc. Chem. Res.*, 2018, **51**, 1571-1580.
110. S. Chen, T. Takata and K. Domen, *Nat. Rev. Mater.*, 2017, **2**, 1-17.
111. T. Hisatomi, J. Kubota and K. Domen, *Chem. Soc. Rev.*, 2014, **43**, 7520-7535.
112. Z. Li, L. Sun, Y. Zhang, Y. Han, W. Zhuang, L. Tian and W. Tan, *Coordin. Chem. Rev.*, 2024, **510**, 215837.
113. J. Mohammed-Ibrahim and X. Sun, *J. Energy Chem.*, 2019, **34**, 111-160.
114. H. Yao, X. Yu, Y.-X. Jia, J.-C. Zhang, J.-X. Yao, J.-Q. Liu, B.-L. Su and X.-H. Guo, *Rare Metals*, 2025, **44**, 2513-2521.
115. F. Meng, L. Zhu, R. Li, J. Jiang, Y. Li, Y. Wu, Y. Fan, P. Ren, H. Xu and D. Wang, *Adv. Funct. Mater.*, 2025, **35**, 2416678.
116. Q. Wang, W. Ling, Y. Lu, H. Zhao, Q. Cheng, Y. Huang, L. Zu, B. Yang and H. Yang, *Angew. Chem.-Int. Edit.*, 2025, **64**, e202506619.
117. L. Wang, M. Ma, C. Zhang, H. H. Chang, Y. Zhang, L. Li, H. Y. Chen and S. Peng, *Angew. Chem.-Int. Edit.*, 2024, **136**, e202317220.
118. F. Zhang, S. Hong, R. Qiao, W.-H. Huang, Z. Tang, J. Tang, C.-W. Pao, M.-H. Yeh, J. Dai and Y. Chen, *ACS Nano*, 2025, **19**, 11176-11186.
119. D. Kim, K.-E. Ryou, G. Park, S. Jung, J. Park, M. Kim, J. Jang, M. Song, S. Kim and J. Kim, *J. Am. Chem. Soc.*, 2025, **147**, 16522-16535.
120. Z. Zhao, Y. Chen, Y. Liu, S. Qin, Z. Li, Z. Zhang and X. Meng, *Adv. Funct. Mater.*, 2026, **36**, e28280.
121. A. Kumar, M. Gil-Sepulcre, J. P. Fandré, O. Rüdiger, M. G. Kim, S. DeBeer and H. Tüysüz, *J. Am. Chem. Soc.*, 2024, **146**, 32953-32964. [DOI: 10.1039/D6SC02712A](https://doi.org/10.1039/D6SC02712A)
122. S. Wang, M. Fan, H. Pan, J. Lyu, J. Wu, H. Tang and H. Zhang, *J. Energy Chem.*, 2024, **96**, 526-535.
123. M. Hou, L. Zheng, D. Zhao, X. Tan, W. Feng, J. Fu, T. Wei, M. Cao, J. Zhang and C. Chen, *Nat. Commun.*, 2024, **15**, 1342.
124. S. Dong, P. Wang, Z. Li, L. Wei, S. Liu, Y. Yang and F. Zheng, *Adv. Funct. Mater.*, 2025, **35**, 2422166.
125. K. Xiao, R.-T. Lin, J.-X. Wei, N. Li, H. Li, T. Ma and Z.-Q. Liu, *Nano Res.*, 2022, **15**, 4980-4985.
126. X. Li, J. Wang, H. Xue, L. Zhao, J. Lu, H. Zhang, M. Yan, F. Deng and C. Hu, *Adv. Funct. Mater.*, 2025, **35**, 2503360.
127. W. Daud, R. Rosli, E. Majlan, S. Hamid, R. Mohamed and T. Husaini, *Renew. Energ.*, 2017, **113**, 620-638.
128. N. Chen and Y. M. Lee, *Prog. Polym. Sci.*, 2021, **113**, 101345.
129. C. Hu and L. Dai, *Angew. Chem.-Int. Edit.*, 2016, **55**, 11736-11758.
130. A. Kulkarni, S. Siahrostami, A. Patel and J. K. Nørskov, *Chem. Rev.*, 2018, **118**, 2302-2312.
131. J. Han, J. Bian and C. Sun, *Research*, 2020, **2020**, 51.
132. M. Pang, M. Yang, H. Zhang, Y. Shen, Z. Kong, J. Ye, C. Shan, Y. Wang, J. An and W. Li, *Nano Res.*, 2024, **17**, 9371-9396.
133. M. Li, X. Zheng, L. Li and Z. Wei, *Acta Phys.-Chim. Sin.*, 2021, **37**, 2007054.
134. B. Cai, X. Chen, L. Wang and H. Fu, *ACS Catal.*, 2024, **14**, 13602-13629.
135. H. Zhang, F. Wu, R. Huang, X. Liu, Z. Zhang, T. Yao, Y. Zhang and Y. Wu, *Adv. Mater.*, 2024, **36**, 2404672.
136. S.-Q. Wang, Z.-C. Yao, Z.-Q. Shi, X. Liu, T. Tang, H.-R. Pan, L. Zheng, Q. Zhang, D. Su and Z. Zhuang, *J. Am. Chem. Soc.*, 2025, **147**, 5398-5407.
137. Y. Han, L. Zhao, W. Cheng, M. Wang, L. Yang, Y. Lin and K. Xu, *Adv. Funct. Mater.*, 2024, **34**, 2407060.
138. X. Zhang, C. Wang, W. Cao, Q. Zhu, C. Cheng, J. Zheng, H. Zhang, Y. Guo, S. Huang and Y. Yu, *Adv. Sci.*, 2025, **12**, 2413569.
139. H. Ren, W. Yu, M. Lv, J. Gao, H. Hu, M. Wang, X. Cui, J. Liu and L. Jiang, *Adv. Funct. Mater.*, 2025, **35**, 2413754.
140. K. He, S. Wei, Q. Zhou, Y. Zhang, D. Li, Y. Liu, W. Cai, F. Yu and H. Zhou, *Adv. Funct. Mater.*, 2025, **35**, 2419609.
141. W. Zhou, B. Li, X. Liu, J. Jiang, S. Bo, C. Yang, Q. An, Y. Zhang, M. A. Soldatov and H. Wang, *Nat. Commun.*, 2024, **15**, 6650.
142. S. Zhang, B. Sun, K. Liao, X. Wang, Z. Chen, J. Wang, W. Hu and X. Han, *Adv. Funct. Mater.*, 2025, **35**, 2425640.
143. Z. Luo, J. Xie, J. Cheng, F. Wei, S. Lyu, J. Zhu, X. Shi, X. Yang, B. Wu and Z. J. Xu, *Adv. Mater.*, 2025, **37**, 2504585.
144. M. Tong, F. Sun, G. Xing, C. Tian, L. Wang and H. Fu, *Angew. Chem.-Int. Edit.*, 2023, **62**, e202314933.
145. Z. Wang, L. Xu, Y. Zhou, Y. Liang, J. Yang, D. Wu, S. Zhang, X. Han, X. Shi, J. Li, Y. Yuan, P. Deng and X. Tian, *Chem. Soc. Rev.*, 2024, **53**, 6295-6321.
146. H. H. Wong, M. Sun, T. Wu, C. H. Chan, L. Lu, Q. Lu, B. Chen and B. Huang, *eScience*, 2024, **4**.
147. C. Xia, X. Wang, C. He, R. Qi, D. Zhu, R. Lu, F.-M. Li, Y. Chen, S. Chen, B. You, T. Yao, W. Guo, F. Song, Z. Wang and B. Y. Xia, *J. Am. Chem. Soc.*, 2024, **146**, 20530-20538.
148. M. Zeng, W. Fang, Y. Cen, X. Zhang, Y. Hu and B. Y. Xia, *Angew. Chem.-Int. Edit.*, 2024, **63**, e202404574.
149. N. Corbin, J. Zeng, K. Williams and K. Manthiram, *Nano Res.*, 2019, **12**, 2093-2125.
150. X. Wang, J. Qian, Z. Lu, J. Huang, L. Zheng, Y. Jiang, M. Cai, Y. Wei, L. Guo and S. Sun, *Green Carbon*, 2025, **3**, 36-43.
151. L. Zhang, F. Mao, L. R. Zheng, H. F. Wang, X. H. Yang and H. G. Yang, *ACS Catal.*, 2018, **8**, 11035-11041.
152. Z. Cheng, B. J. Sherman and C. S. Lo, *J. Chem. Phys.*, 2013, **138**, 014702.
153. X.-C. Sun, K. Yuan, J.-H. Zhou, C.-Y. Yuan, H.-C. Liu and Y.-W. Zhang, *ACS Catal.*, 2021, **12**, 923-934.
154. S. Wei, J. Zhu, X. Chen, R. Yang, K. Gu, L. Li, C.-Y. Chiang, L.



- Mai and S. Chen, *Nat. Commun.*, 2025, **16**, 1652.
155. Y. Pan, R. Lin, Y. Chen, S. Liu, W. Zhu, X. Cao, W. Chen, K. Wu, W.-C. Cheong and Y. Wang, *J. Am. Chem. Soc.*, 2018, **140**, 4218-4221.
156. H. Li, L. Fang, T. Wang, R. Bai, J. Zhang, T. Li, Z. Duan, K.-J. Chen and F. Pan, *Adv. Mater.*, 2025, **37**, 2416337.
157. Y. Gao, E. Wang, Y. Zheng, J. Zhou and Z. Sun, *Energy Material Advances*, **4**, 0039.
158. Y. Wu, C. He and W. Zhang, *J. Am. Chem. Soc.*, 2022, **144**, 9344-9353.
159. J. Kundu, T. Bhoyar, S. Park, H. Jin, K. Lee and S.-I. Choi, *Adv. Powder Mater.*, 2025, **4**, 100279.
160. M. M. Alsabban, K. Peramaiah, A. Genovese, R. Ahmad, L. M. Azofra, V. Ramalingam, M. N. Hedhili, N. Wehbe, L. Cavallo and K. W. Huang, *Adv. Mater.*, 2024, **36**, 2405578.
161. R. Li, R. Ma, L.-L. Zhang, W. Ma, G. Shao, X. Zhang, Y. Tian, M. Jiao and Z. Zhou, *ACS Nano*, 2025, **19**, 17686-17697.
162. Y. Kong, L. Wu, X. Yang, Y. Li, S. Zheng, B. Yang, Z. Li, Q. Zhang, S. Zhou and L. Lei, *Adv. Funct. Mater.*, 2022, **32**, 2205409.
163. M. Xie, F. Dai, H. Guo, P. Du, X. Xu, J. Liu, Z. Zhang and X. Lu, *Adv. Energy Mater.*, 2023, **13**, 2203032.
164. S. Zhang, Y. Song, Y. Liu, J. Zhu, Z. Ma, L. Qing, Z. Wang, L. Zhang, T. Liu and Y. Xie, *Adv. Funct. Mater.*, 2025, **36**, e02874.
165. Y. Zhang, Z. Xie, S. Ge, P. Li, X. Wang, Z. Zhao, Z. Liu, B. Liu and J. Li, *Nano Res.*, 2026, **19**, 94908176.
166. W.-J. Liu, Z. Xu, D. Zhao, X.-Q. Pan, H.-C. Li, X. Hu, Z.-Y. Fan, W.-K. Wang, G.-H. Zhao and S. Jin, *Nat. Commun.*, 2020, **11**, 265.
167. C. Lei, Z. Chen, T. Jiang, S. Wang, W. Du, S. Cha, Y. Hao, R. Wang, X. Cao and M. Gong, *Angew. Chem.-Int. Edit.*, 2024, **136**, e202319642.
168. Y. Xiong, M. Qiu, Y. Wang, Q. Liu, D. Ouyang, Y. Liu, C. Chen, J. Jiang, M. Fan and K. Wang, *Research*, 2025, **8**, 0925.
169. J. Wang, B. Zhang, W. Guo, L. Wang, J. Chen, H. Pan and W. Sun, *Adv. Mater.*, 2023, **35**, 2211099.
170. H. Li, S. Zhou, J. Liu, W. Wang, A. Chen, L. Sheng, J. Zhao, Y. Li, Y. Sui and B. Zou, *Adv. Sci.*, 2024, **11**, 2403813.
171. H. Xu, G. Xin, W. Hu, Z. Zhang, C. Si, J. Chen, L. Lu, Y. Peng and X. Li, *Appl. Catal. B: Environ.*, 2023, **339**, 123157.
172. J. Qiu, X. Gao and J. Peng, *Chem. Eng. J.*, 2025, **513**, 162961.
173. W. Luo, H. Tian, Q. Li, J. Ma, W. Sun, L. Zhu, H. Wu, F. Kong, X. Zhuang and X. Cui, *Angew. Chem.-Int. Edit.*, 2025, **64**, e202505059.
174. L. Cai, Y. Liu, Y. Gao, B. H. Zhao, J. Guan, X. Liu, B. Zhang and Y. Huang, *Angew. Chem.-Int. Edit.*, 2025, **64**, e202417092.
175. Z. Gong, M. Xu, P. Li, G. Ye, W. Li and H. Fei, *ACS Catal.*, 2025, **15**, 20958-20967.

View Article Online
DOI: 10.1039/D6SC02712A



View Article Online
DOI: 10.1039/D6SC02712A

Data availability

No primary research results, software or code have been included and no new data were generated or analysed as part of this review.

